Delft University of Technology

Master of Science Thesis

Turbulence radiation interactions in fully developed channel flow

Author:

Simone Silvestri

Supervisors:

Ir. A. Patel

Dr.Ir. R. Pecnik

Prof.Dr D.J.E.M. Roekaerts

A thesis submitted in fulfillment of the requirements for the degree of Master of Science in Mechanical Engineering

Faculty of Mechanical, Maritime and Materials Engineering, Process & Energy department

February 2016

Delft University of Technology

Abstract

Faculty of Mechanical, Maritime and Materials Engineering, Process & Energy department

Master of Science in Mechanical Engineering

Turbulence radiation interactions in fully developed channel flow

by Simone Silvestri

Radiative heat transfer plays an important role in many industrial applications, particularly when high temperature heat transfer is involved. Many theoretical analysis and experimental investigations have shown the occurrence of interactions between radiation quantities and turbulence, mainly due to the non-linearity between radiative heat transfer and the temperature field. Turbulence Radiation interactions (TRI) are characterized by the effect of turbulence on radiation and vice versa the influence of radiation in the modification of the turbulence field. While the first effect of TRI has been extensively studied, a comprehensive understanding of the effect of radiation on temperature variance is still lacking. In addition radiative heat transfer, and thus TRI, present largely different effects based on the optical thickness of the participating media. Therefore, a thorough study regarding the impact of the optical thickness of the flow in characterizing TRI is required.

The present work consists of an investigations of TRI in a non reactive turbulent channel flow based on three optical depths ($\tau = 0.1,1,10$). A Finite Volume Method for radiative heat transfer has been implemented and coupled with a DNS code for turbulent channel flow. A fictitious fluid has been simulated with both grey properties and variable absorption coefficient based on the Planck mean absorption coefficient of water vapour. The effects of radiation on the thermal fluctuation field are described and discussed. The results show a strong impact of the optical thickness of the media on the temperature fluctuation field, depicting a transition in TRI behaviours. While for a low value of optical depth (τ), a dissipative effect of TRI on temperature variance is reported, for high optical thicknesses the appearance of large thermal structures in the core of the channel is observed. In particular the distinct and contrasting role of absorption and emission in modifying temperature variance is highlighted and analyzed.

In addition the study of TRI is parametrized on the Planck number. While a strong impact in the temperature field is noticed, the characteristics of TRI are not modified with a change in the Planck number.

Acknowledgements

This project required a large amount of research, work and dedication. However, it would have not been possible without the huge help of many individuals.

First of all I would like to express my sincere gratitude to Dr. Ir. Rene Pecnik. I have been amazingly fortunate to have as my supervisor someone who demonstrated complete trust in me. He provided me with motivation and inspiration, which I both consider essential for the development of my work. It is thanks to his availability and his willingness to dedicate me his time that I was able to develop and complete my master thesis project.

I also want to warmly thank Ir. Ashish Patel for the effort showed throughout the project. He had the patience to follow me on a daily basis and to supply my lack of knowledge in the turbulence field. It was also thanks to many debates done together that I had the chance to enrich my ideas and develop my research. I owe to his expertise the final form of this project. I am thankful to both for reading and reviewing extensively my report.

I would also like to acknowledge Prof. Dr. Dirk Roekaerts for the time devoted in supervising me as well as for his valuable advises, and Ir. Hassan Nemati for his initial guidance.

This whole experience at TU Delft would have not been possible without the immense support of my family that has been a constant source of love, strength and encouragement.

I would like to thank my friends who were always there for me during these two past years of MSc, adding a lot of fun to an amazing experience. The last words of acknowledgement I have saved for Giulia, who contributed in making these past years the best of my life.

Contents

Abstract ii

Acknowledgements v

Contents v

List of Figures ix

Symbols xiii

1 Introduction 1

2 Radiative heat transfer 7
2.1 Introduction to radiative transfer . . . 7
2.1.1 Radiative transfer equation in participating media . . . 7
2.1.2 Boundary conditions . . . 10
2.1.3 Radiation Source term . . . 10
2.2 Radiation modelling . . . 11
2.3 Finite Volume Method . . . 12
2.3.1 Spatial discretization schemes . . . 14
2.3.2 Cartesian coordinates . . . 17
2.4 Mathematical description of TRI in a fluctuating thermal field . . . 24

3 Fully developed turbulent channel flow 29
3.1 Direct numerical simulation . . . 29
3.2 Numerical details . . . 30

4 Results and Discussion 35
4.1 Grey Gas . . . 35
4.1.1 Mean flow properties . . . 35
4.1.2 Heat flux . . . 37
4.1.3 Temperature variance and fluctuations of radiative quantities . . . 41
4.1.4 Budgets of temperature variance . . . 45
4.1.5 Temperature, velocity and incident radiation correlations . . . 51
4.1.6 Spectral analysis . . . 54
4.2 Variable absorption coefficient . . . 62
4.2.1 Mean flow properties . . . 62
4.2.2 Temperature variance analysis . . . 63

4.3 Effect of Planck number 68
4.3.1 Mean flow properties 68
4.3.2 Thermal turbulence, temperature variance budgets and spectral analysis 69
4.4 Turbulent heat flux modeling in radiative flows 72

5 Conclusions and Recommendations **77**
5.1 Conclusions 77
5.2 Recommendations 78

A Reynolds Averaged Navier Stokes Equations **81**

B Derivation of temperature variance transport equation **83**

C Properties of Fourier transform **85**

Bibliography **87**

List of Figures

2.1 Phenomena occurring in radiative heat transport for participating media . 8
2.2 solid angle Ω and angular variables θ and ϕ 13
2.3 Indexes of neighbouring cells starting from computational cell p and face k 15
2.4 Cubic enclosure for 3D Cartesian validation 18
2.5 Validation as for Sakurai et al [1], optically very thin case: $\kappa = 0.01$ . . . 19
2.6 Validation as for Sakurai et al [1], optically thin case: $\kappa = 0.1$ 20
2.7 Validation as for Sakurai et al [1], optically intermediate case: $\kappa = 1$. . . . 20
2.8 Validation as for Sakurai et al [1], optically thick case: $\kappa = 5$. 21
2.9 Validation as for Sakurai et al [1], optically very thick case: $\kappa = 10$. . . . 22
2.10 absorption coefficient 0.5, scattering coefficient 0.5 22
2.11 varying κ; dotted line: STEP base case, *: CLAM base case, dashed line: STEP angle refined, dashed dotted line: CLAM angle refined, solid line: STEP spatially refined, ○: CLAM spatially refined, ♦: benchmark from Burns and Christen [2] 23
2.12 behaviour of scaling function $\Re(\mathbf{w}, \kappa)$ for different wavenumbers and absorption coefficients κ 26
2.13 behaviour of scaling function $4 - \Re(\mathbf{w}, \kappa)$ for different wavenumbers and absorption coefficients κ 27

3.1 geometry for channel flow, wall bounded in x direction and periodic in the homogeneous directions 31

4.1 Averaged profiles. (a): mean temperature; (b): mean emissive power; (c): mean incident radiation; (d): mean radiative heat source (the inlay shows a zoom on the y-axis around $\overline{P}_r = 0$). 36
4.2 heat transfer mechanisms. (a): total heat flux; (b): mean conductive heat flux; (c): mean wall normal turbulent heat flux; (d): mean radiative heat flux normalized on wall radiative flux on hot side 38
4.3 radiative heat flux $\overline{q}_R$ 39
4.4 Turbulent intensity of temperature fluctuation 41
4.5 incident radiation root mean square profiles 43
4.6 (a): E_m root mean square profiles; (b): P_r root mean square profiles . . . 43
4.7 Budgets of temperature variance for Reference case (Ref) 46
4.8 Budgets of temperature variance for case G01 $\tau = 0.1$, inclusion highlights the core zone ($x/\delta = 0.6 - 1.2$) 47
4.9 Budgets of temperature variance for case G1 $\tau = 1$. 47
4.10 Budgets of temperature variance for case G10 $\tau = 10$ 48
4.11 Radiation term $\mathcal{R}$ decomposed in absorption $\mathcal{R}_a$ and emission term $\mathcal{R}_e$ normalized by absorption coefficient κ for different optical thickness . . . 50

4.12 (a): streamwise velocity - temperature co-variance (streamwise turbulent heat flux); (b): incident radiation - temperature co-variance 51
4.13 temperature longitudinal (a,c and e) and transverse (b,d and f) 2-point autocorrelation $\rho_{\theta,\theta}$ for different channel heights 53
4.14 Temperature energy spectra $E_{\theta,\theta}$ at $x/\delta = 1.5$, (a): longitudinal energy spectra; (b): transverse energy spectra 54
4.15 Temperature energy spectra $E_{\theta,\theta}$ at $x/\delta = 1.93$, (a): longitudinal energy spectra; (b): transverse energy spectra 55
4.16 Pre-multiplied, normalized thermal energy spectra contours $w_2 E_{\theta,\theta}/\overline{\theta'\theta'}$; (a): no radiation case; (b) $\tau = 0.1$ 55
4.17 Pre-multiplied, normalized thermal energy spectra contours $w_2 E_{\theta,\theta}/\overline{\theta'\theta'}$; (a): $\tau = 1$; (b) $\tau = 10$ 56
4.18 Incident radiation energy spectra $E_{G,G}$ normalized by optical thickness τ at $x/\delta = 1.$, (a): longitudinal energy spectra; (b): transverse energy spectra 57
4.19 Incident radiation energy spectra $E_{G,G}$ normalized by optical thickness τ at $x/\delta = 1.93$, (a): longitudinal energy spectra; (b): transverse energy spectra 57
4.20 inverse of characteristic time scales for molecular dissipation and radiative terms at $x/\delta = 1.5$, (a): using transverse spectral information; (b): using longitudinal spectral information 58
4.21 Snapshots of θ' at $x/\delta = 1.5$; (a): No radiation; (b): $\tau = 0.1$; (c): $\tau = 1.$; (d): $\tau = 10$. 60
4.22 Snapshots of θ' at $x/\delta = 1.93$; (a): No radiation; (b): $\tau = 0.1$; (c): $\tau = 1.$; (d): $\tau = 10$. 61
4.23 Averaged profiles. (a): mean temperature; (b): mean absorption coefficient; (c): mean incident radiation; (d): mean radiative heat source 62
4.24 Temperature root mean square profiles; markers denote varying κ cases, while lines denote grey gas cases 63
4.25 Emission term normalized by the optical thickness, for variable κ (markers) and grey cases (lines) 64
4.26 Absorption term normalized by optical thickness 65
4.27 Absorption coefficient correlations, (a) absorption coefficient - incident radiation correlation normalized on optical thickness; (b): absorption coefficient - temperature correlation normalized on optical thickness 65
4.28 Averaged profiles. (a): mean temperature; (b): mean absorption coefficient; (c): mean incident radiation; (d): mean radiative heat source 68
4.29 $\sqrt{\overline{\theta'^2}}$ profiles for $Pl = 0.3$ and various optical thickness. 69
4.30 Temperature variance budgets, (a): non radiative case; (b): case L01, $\tau = 0.1$; (c): case L1, $\tau = 1$; (d): case L10, $\tau = 10$ 70
4.31 Temperature energy spectra $E_{\theta,\theta}$ at $x/\delta = 1.1$, (a): longitudinal energy spectra; (b): transverse energy spectra 71
4.32 Pre-multiplied, normalized thermal energy spectra contours $w_2 E_{\theta,\theta}/\overline{\theta'\theta'}$; (a): no radiation case; (b) $\tau = 0.1$ 72
4.33 Pre-multiplied, normalized thermal energy spectra contours $w_2 E_{\theta,\theta}/\overline{\theta'\theta'}$; (a): $\tau = 1$; (b) $\tau = 10$ 72
4.34 turbulent Prandtl number calculated for case Ref, and comparison between calculated and modeled Pr_{t_R} for cases G01,G1 and G10 74

4.35 $\mathcal{U}$ normalized with radiation-based scaling as proposed by Zhang et al [3] for cases Ref, G01, G1 and G10 75

B.1 Radiative budgets for temperature variance equation, $\tau = 10$, CLAM scheme 84

Symbols

Latin letters

A	Facial area
c_p	specific heat capacity at constant pressure
$\mathcal{D}$	Conductive heat flux
E_m	Emissive power
I	Intensity of radiation beam
I_b	Blackbody intensity
$\Im$	Absorption parameter, imaginary part
G	Incident radiation
k	Conductive heat transfer coefficient
$\mathbf{n}$	Area normal unit vector
$\mathcal{P}_\theta$	Production of temperature variance
P_r	Net volumetric heat source (radiative power)
P_a	Absorptive volumetric power (heat source)
P_e	Emissive volumetric power (heat sink)
Pl	Plank number
Pr	Prandtl number
Pr_t	Turbulent Prandtl number
$\mathbf{q}_r$	Radiative heat flux vector (q_x, q_y, q_z)
q_{turb}	Turbulent heat flux
q_{cd}	Conductive heat flux
q_R	Radiative heat flux
$\mathcal{R}$	Radiative term in temperature variance budgets
$\mathcal{R}_e$	Emissive term in temperature variance budgets
$\mathcal{R}_a$	Absorptive term in temperature variance budgets
$\Re$	Absorption parameter, real part
Re	Reynolds number
$\widehat{\mathbf{s}}$	Intensity beam unit direction vector
S	Source function
T_b	Bulk temperature
$\mathcal{T}_\theta$	Turbulent transport of temperature variance

$\mathbf{u}$	Velocity vector (u, v, w)
$\mathcal{U}$	Turbulent heat flux
U_b	Bulk velocity
V	Control volume
$\mathbf{w}$	wavenumber vector (w_1, w_2, w_3)

Greek letters

α_t	Eddy diffusivity
β	Extinction coefficient
γ	Radiation scaling factor
δ	Half channel height
ϵ_w	Wall emissivity
ϵ_m	Molecular dissipation of temperature variance
ϵ_r	Radiative dissipation of temperature variance
η	Waveumber of radiation spectrum
η_B	Batchelor scale
η_K	Kolmogorov scale
κ	Absorption coefficient
κ_P	Plank mean absorption coefficient
κ_G	Incident mean absorption coefficient
μ	Dynamic viscosity
ν	Kinematic viscosity
ν_t	Eddy viscosity
ρ^d	Diffuse reflectivity
ρ^s	Specular reflectivity
ρ	Density
ρ_{f_1,f_2}	Correlation between f_1 and f_2
σ	Stefan Boltzmann constant
σ_s	Scattering coefficient
θ	Non dimensional temperature and polar angle
ϕ_m	Molecular diffusion
ϕ_r	Radiative diffusion
ϕ	Azimuthal angle
Φ	Phase function
Ω	Solid angle

Abbreviations

DNS	Direct Numerical Simulation
DO	Discrete Ordinates

FVM	Finite Volume Method
LES	Large Eddy Simulation
LHS	Left Hand Side
PBL	Planetary Boundary Layer
RHS	Right Hand Side
RTE	Radiative Transfer Equation
SGS	Sub Grid Scales
TRI	Turbulence Radiation Interactions

"*Lo duca e io per quel cammino ascoso*
intrammo a ritornar nel chiaro mondo;
e sanza cura aver d'alcun riposo,

salimmo sù, el primo e io secondo,
tanto ch'i' vidi de le cose belle
che porta 'l ciel, per un pertugio tondo.

E quindi uscimmo a riveder le stelle. "

Dante Alighieri

Chapter 1

Introduction

Radiative heat transfer refers to heat transport via electromagnetic waves. When dealing with radiative heat transfer great attention must be paid to "participating" media. A fluid is referred to as participating if it is able to absorb, emit and scatter radiation waves. The interference of a fluid with electromagnetic waves is strongly dependent on the optical depth of the system that defines the attenuation of the intensity beam traveling trough the media. Different optical thicknesses can result in completely different qualitative behaviours of the media. As an example, intensity beams originating from the sun are relatively unobstructed by the presence of air, resulting in a direct heating of the earth's surface. It is thus possible to state that earth's atmosphere acts as an optically thin media towards sun's radiation. On the other hand, in the core of a nuclear power plant, a pool of heavy water is used to provide shielding from radiation. Radiation intensity leaving the nucleus is fully depleted once it reaches the outer boundaries of the pool. Thus heavy water is regarded as a optically thick media.

When dealing with heat transfer applications, high velocities of the working media are employed in order to enhance the heat transfer due to mixing, therefore resulting in turbulent flows. In particular for high temperature applications, where radiative heat transfer can be regarded as the main heat transfer mode, a special attention must be given to the coupling of the two heat transfer mechanism, since a high level of interaction occurs. Therefore the influence of the optical depth of the fluid plays an important role and since different qualitative behaviours occur, variable results can be obtained based on the objective of the heat transfer process (heating of the medium or heating of the surface). Despite a relatively high level of understanding, the characterization of the coupling between radiative heat transfer and convective heat transfer still represents a challenging task due to the highly non linear coupling between temperature and radiation field. This non linear coupling results in a case dependent effect, preventing the development of solid and universal models. Turbulence Radiation Interactions (TRI)

are characterized by the effect of turbulence on radiation and vice versa the modification of turbulence due to radiation. The importance of TRI in modeling participating flows has long been recognized resulting in a large amount of open literature available on the topic. Due to the considerable relevance of radiative heat transfer in combustion applications, the research has been mainly focused on reactive flows, in order to assess and quantify the heat loss caused by TRI.

Wu et al. [5] developed a high fidelity Photon Monte Carlo (PMC) method for radiative transfer in Direct Numerical Simulations (DNS). They tested the method on one-dimensional laminar premixed flames and on a statistical one-dimensional turbulent premixed flames showing the compatibility of a Monte Carlo simulation with the high accuracy of DNS. Their method was used by Deshmukh et al. [6] to investigate turbulence-radiation interactions in a statistically one-dimensional non-premixed flames. In order to study the effect of TRI, several correlation coefficients were calculated: temperature auto-correlation, absorption coefficient - blackbody intensity correlation and absorption coefficient - intensity correlation. TRI from all three contributions were found to be significant and increasing with optical thickness.

TRI in an horizontal plane channel flow have been studied by Sakurai et al. [1]. Optically Thin Approximation (OTA) was used for the radiative heat transfer. The Boussinesq approximation was used in order to study the effect of an absorbing emitting gas on developing buoyant turbulent structures in a channel with isothermal hot and cold walls. The range of studied optical depths was limited to moderately optically thin media due to the use of the OTA with a maximum τ of 0.1. Results show a dissipation of thermal turbulence field due to the action of radiation. They noticed a decrease of the temperature gradient near the hot wall as the optical thickness increased. Moreover, the downward flow towards the cold wall was observed to reduce due to the effect of a high overall temperature of the fluid. The conclusions showed that radiation effects cause a breakage of the organized large scale vortices resulting in a reduction of the turbulent heat flux with the increase of the optical thickness. Moreover, they observed that the suppression of buoyancy driven large scales affects the wall normal velocity fluctuation by producing a profile similar to a forced convection case. The role of radiation was investigated in wall normal and stream wise turbulent heat flux as well as in temperature variance transport equations. The radiative term was noticed to be always negative, therefore reducing the aforementioned quantities. Since the radiative term remained small for all investigated cases, Sakurai et al. [1] concluded that radiation contributes through the modification of mean gradient terms rather than through the direct dissipative action caused by the radiative term.

Roger et al. [8] quantified the influence of intensity Sub Grid Scales (SGS) fluctuations in the resolution of the filtered Radiative Transfer Equation (RTE), in LES of

turbulent planar jets. The results confirmed that neglecting the SGS-TRI may be a correct approximation, since sub grid scales are relevant (and important) only near the jet edges where radiative transfer is low. On the other hand Gupta, Haworth and Modest [9] analyzed the SGS-TRI term for reactive flow, in particular luminous and non luminous non-premixed flames. Results show that SGS fluctuations of emission TRI exceeds the resolved scale fluctuations, indicating the need for modeling in LES, while absorption TRI is mostly contributed by the resolved scales fluctuations, thus enabling the omission of an absorption SGS term.
Gupta et al. [4] performed Large Eddy Simulations (LES) of a planar turbulent channel flow with non reactive and reactive mixtures. They focused on the closure of the average net radiative volumetric heat source by analyzing statistical correlations of temperature, blackbody intensity and the absorption coefficient. From their findings, in a non reactive flow radiation fluctuations originating from temperature variance are negligible, which justifies the use of the average temperature to calculate of the mean net radiative volumetric source. Turbulence radiation interactions are noticed to be much higher in a reacting case and increasing as optical thickness increases.

The most extensive study of turbulence radiation interactions was performed by Yufang Zhang [3] using low Mach approximation for DNS and an optimized reciprocity emission based Monte Carlo method for radiation calculations. A comprehensive study on the effects of radiation on enthalpy as well as on turbulent budgets equations was performed. Based on their results they proposed a "radiation scaling" in order to scale all radiation affected quantities and obtain universal collapsed profiles. Furthermore, a model for the turbulent Prandtl number was proposed in order to model turbulent heat flux with the gradient diffusion approximation in wall modelled large eddy simulation. All simulations were performed on a burnt gas composition mixture. In chapter 4, the proposed models for scaling and turbulent Prandtl number will be tested for various optical depths in a turbulent channel flow.

The above presented literature review deals with the study of radiative heat transfer and TRI in reactive and non-reactive flows by considering mostly the effect of turbulence on radiation. On the other hand, the influence of radiation in modifying the thermal turbulent structures and interacting between temperature modes was first investigated by Schertzer and Simonin [10]. Their work deals with the identification of the effect of radiative transfer on thermal turbulent spectra. All relations were obtained with scaling arguments and analytic calculations. Relations of radiative dissipation, ξ_R, with turbulent transport and molecular dissipation of temperature variance were studied in the framework of homogeneous isotropic turbulence. A scaling for the temperature spectra due to radiation ($N(w)$) is obtained and compared to spectral molecular dissipation in the framework of atmospheric boundary layer. Results show the appearance of

a "inertio-radiative" range in the thermal turbulence spectrum where radiative dissipation dominates over molecular dissipation for strong radiative effects (large absorption coefficient). The resulting temperature spectra shows a slope of $\mathbf{w}^{-3}$ both in the grey and non-grey case.
The work of Schertzer and Simonin was further developed by Soufiani [11], who investigated the thermal turbulent spectra for high temperature radiating gasses, specifically H_2O and CO_2, in homogeneous isotropic turbulence. Soufiani concluded that radiation acts as a dissipation term on temperature fluctuation; its influence is mostly observed in the large wavenumber range where radiation drastically modifies the temperature spectra by damping the energy contained in the small scales.
Moreover, Coantic and Simonin [12], continued the work developed by Schertzer and Simonin [10], focused on the Planetary Boundary Layer (PBL). They analyzed the spectral budgets of temperature variance while employing the homogeneous isotropic turbulence assumption. They observed that thermal turbulence spectra in the PBL is a function of η_K/κ_P, and effect of radiation is noticeable only at extremely low value of this ratio. Overall effects of radiative dissipation are shown to be of limited importance in modeling temperature variance in the terrestrial boundary layer, since radiative terms do not show a relevant effect on the temperature variance transport equation.

Despite all the theoretical work and simulations performed on the topic, a comprehensive understanding of TRI regarding the influence of radiation in temperature variance, depending on various optical thicknesses is lacking.This mostly due to the difficulty associated with modeling high optical depths and due to the high computational expenses required by even relatively simple radiation models. The aim of this work is to provide a further understanding on how radiative heat transfer affects the temperature field, and how TRI modify temperature structure and the thermal energy spectra. DNS will be used, coupled with a Finite Volume Method (FVM) to investigate different optical depths, to observe the qualitative behaviour of heat transfer mechanism and to enrich the theory unravelling the physics behind a complicated phenomena such as turbulence radiation interactions. In addition, the simulation of a turbulent channel flow will provide information on the spectral effects of inhomogeneous turbulence on radiation and vice versa, expanding the knowledge on this topic that is currently limited to homogeneous isotropic turbulence.

Thesis outline

Chapter 2 introduces the theory on radiative heat transfer and radiative transport modeling. A Finite Volume Method (FVM) for the solution of the radiative heat transfer has been used in the present work, which will be outlined in detail and verified by comparison with analytical solutions. Finally, the influence of radiative heat transfer in a fluctuating thermal field will be discussed with the aid of Fourier transforms. This final section will provide a theoretical framework for the investigations developed later on in the thesis.

Chapter 3 will provide an introduction on turbulent flows and on direct numerical simulations. The governing equations will be presented and the numerical details of the implementation will be briefly discussed.

Chapter 4 will presents a discussion of the results obtained for a grey participating turbulent channel flow with different optical thicknesses. Following, an analysis of the influence of two parameters, namely absorption coefficient and Planck number, in heat flux as well as thermal fluctuation levels in channel flow is performed.

Finally, the results will be concluded in chapter 5 and an outlook for further developments is provided.

Chapter 2

Radiative heat transfer

2.1 Introduction to radiative transfer

All bodies with a non-zero temperature emit thermal radiation. Radiative transfer is a heat transfer mode like convection and conduction, but, unlike the latters, radiation scales with the fourth power of temperature, dominating heat transfer when high temperatures are involved, as in most industrial applications and processes.
Conduction and convection are relatively short range phenomena, whereas radiation length scales are much larger allowing heat transfer across infinitely far locations if unobstructed. Therefore, radiation needs to be modelled accounting for the variation in space following specific propagation directions, while traveling in a participating media that is able to emit, absorb and scatter electromagnetic waves.

2.1.1 Radiative transfer equation in participating media

In order to describe radiative heat transfer, an intensity needs to be defined. The intensity represents the flux of energy carried by single a monochromatic beam. The units of intensity are $W/(m^2 sr \mu m)$, where steradians (sr) represent the angular dependency, while μm accounts for the dependency on wavelength. While a beam of thermal radiation travels in a participating media, its energy content can be depleted by absorption and out-scattering or it can be augmented by emission and in-scattering. If all these effects are taken into account, the Radiative Transfer Equation (RTE) results in a complicated integro-differential equation with 7 independent variables (3 spatial locations, 2 angular directions, 1 spectral variable and time)

$$\frac{1}{c}\frac{\partial I_\eta}{\partial t} + \frac{\partial I_\eta}{\partial s} = \kappa_\eta I_{b\eta} - \kappa_\eta I_\eta - \sigma_{s,\eta} I_\eta + \frac{\sigma_{s,\eta}}{4\pi}\int_{4\pi} I_\eta(\hat{\mathbf{s}}_i)\Phi_\eta(\hat{\mathbf{s}}_i, \hat{\mathbf{s}}) d\Omega_i \ . \tag{2.1}$$

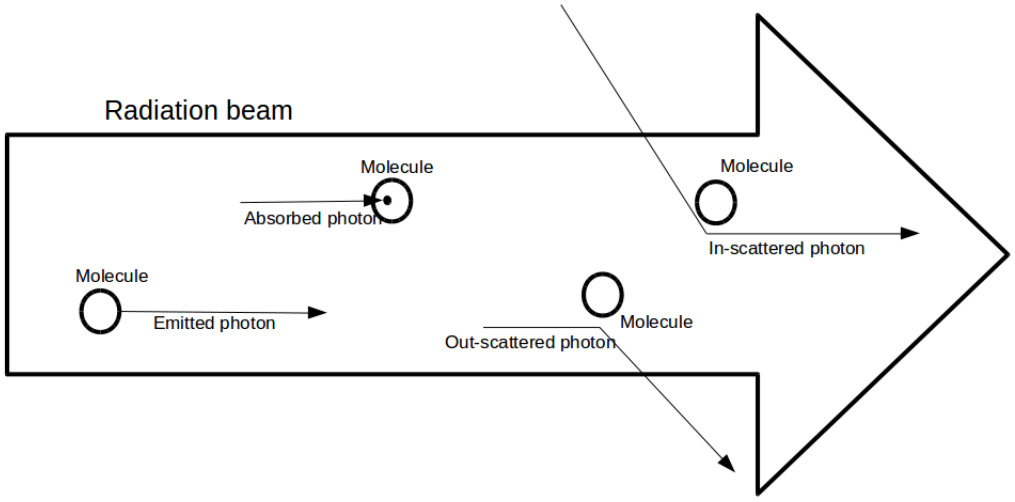

FIGURE 2.1: Phenomena occurring in radiative heat transport for participating media

Equation (2.1) is the full RTE obtained by radiative energy balance. The spectral absorption coefficient, denoted as κ_η, is a proportionality constant that represents the amount of absorption in a unit length traveled. $\sigma_{s,\eta}$ is the spectral scattering coefficient, which quantifies the amount of scattering from the media, namely the relative amount of photons in the beam that change direction due to interaction with molecules. The Left Hand Side (LHS) of equation (2.1) represents the change of intensity in time and in space, where s is the spatial coordinate in the beam propagation direction. The velocity of radiation transfer is in the order of speed of light ($\sim$ 300,000 m/s), hence the time dependent term of equation (2.1) is usually neglected since radiative heat transfer time scales are much lower than typical conduction and convection time scales. On the Right Hand Side (RHS) of equation (2.1), the first term represents augmentation by emission from the media, the second term is depletion by absorption, while the third and fourth term are out and in scattering, respectively. Figure 2.1 shows a schematic interpretation of the phenomena as described in equation (2.1). By neglecting the time dependent term and introducing a source function and an extinction coefficient, the radiative transfer equation can be simplified as follows:

$$\nabla I_\eta \cdot \hat{\mathbf{s}} = S_\eta - \beta_\eta I_\eta \ , \tag{2.2}$$

where the partial derivative on the propagation direction has been converted to a total derivative, because the process is assumed to be quasi-steady. β_η and S_η are calculated as:

$$\beta_\eta = \kappa_\eta + \sigma_\eta \ , \tag{2.3}$$

$$S_\eta = \kappa_\eta I_{b\eta} + \frac{\sigma_\eta}{4\pi} \int_{4\pi} I_\eta(\hat{\mathbf{s}}_i) \Phi_\eta(\hat{\mathbf{s}}_i, \hat{\mathbf{s}}) d\Omega_i \ . \tag{2.4}$$

Two common approximations for the radiative transfer equation are:

- grey gas
- emitting-absorbing media

In the first case, the absorption coefficient, the scattering coefficient and the phase function are considered constant with respect to wavelength. Therefore, the total intensity can be calculated directly by integrating equation (2.1) in wavenumber, with:

$$I_b = \int_0^\infty I_{b\eta} d\eta \ , \tag{2.5}$$

$$I = \int_0^\infty I_\eta d\eta \ . \tag{2.6}$$

In the second case, scattering is neglected thus $\sigma_\eta = 0$ and equation (2.1) can be simplified as:

$$\nabla I_\eta \cdot \hat{\mathbf{s}} = \kappa_\eta \cdot (I_{b\eta} - I_\eta) \ . \tag{2.7}$$

By integrating equation (2.7) over the wavenumber, it is possible to calculate the total intensity transported:

$$\int_0^\infty \nabla I_\eta \cdot \hat{\mathbf{s}} d\eta = \int_0^\infty \kappa_\eta I_{b\eta} d\eta - \int_0^\infty \kappa_\eta I_\eta d\eta \ . \tag{2.8}$$

In order to obtain a relation for the integrated intensity, the first term on the RHS is multiplied and divided by I_b as defined in (2.5). The second term on the RHS is multiplied and divided by I as defined in (2.6), yielding:

$$\nabla I \cdot \hat{\mathbf{s}} = \kappa_P I_b - \kappa_G I \ , \tag{2.9}$$

where κ_P is the Planck mean absorption coefficient and κ_G is the incident mean absorption coefficient calculated as:

$$\kappa_P = \frac{\int_0^\infty \kappa_\eta I_{b\eta} d\eta}{\int_0^\infty I_{b\eta} d\eta} \ , \tag{2.10}$$

$$\kappa_G = \frac{\int_0^\infty \kappa_\eta I_\eta d\eta}{\int_0^\infty I_\eta d\eta} \ . \tag{2.11}$$

While the Planck mean absorption coefficient depends only on the medium properties, the incident mean absorption coefficient depends also on the spectral properties of the boundary, hence for general cases $\kappa_P \neq \kappa_G$. However, if the system is isolated and the boundary temperature is similar to the temperature of the medium, it is possible to assume $\kappa_P \sim \kappa_G$, as done by Gupta [4, 9] and Sakurai [1] because the emission wavelength is similar to the absorption wavelength. Therefore from now on the subscript P can be omitted by defining $\kappa = \kappa_P$ for non-grey simulations. Scattering has been assumed isotropic and grey for validation purposes, but due to extremely high computational

expenses, it has been neglected for the coupled simulations as described in chapter 3). Because of these simplifications the dependency on wavelength is removed and from here on only total quantities (i.e. integrated in wavenumber) will be discussed. The simplified total radiative transfer equation is then given as:

$$\nabla I \cdot \hat{\mathbf{s}} = \kappa I_b - \kappa I - \sigma_s I + \frac{\sigma_s}{4\pi} \int_{4\pi} I d\Omega \ . \tag{2.12}$$

2.1.2 Boundary conditions

The boundary conditions for the intensity depend on the properties of the enclosing surfaces. For diffusely emitting and reflecting grey surfaces, the boundary condition can be written as:

$$I(\mathbf{r}_w, \hat{\mathbf{s}}) = \epsilon(\mathbf{r}_w) I_b(\mathbf{r}_w) + \frac{\rho^d(\mathbf{r}_w)}{\pi} \int_{\hat{\mathbf{n}} \cdot \hat{\mathbf{s}} < 0} I(\mathbf{r}_w, \hat{\mathbf{s}}') |\hat{\mathbf{n}} \cdot \hat{\mathbf{s}}'| d\Omega' + \rho^s I(\mathbf{r}_w, \hat{\mathbf{s}}_s) \ . \tag{2.13}$$

The first term on the RHS represents the emission from the surface, while the second and third terms represent the fraction of diffusely reflected and specularly reflected radiation, respectively. The sum of the emissivity of the surface and its total reflectivity must be unity ($\epsilon + \rho^s + \rho^d = 1$) and specular reflection direction can be calculated as:

$$\hat{\mathbf{s}}_s = \hat{\mathbf{s}} - 2(\hat{\mathbf{s}} \cdot \hat{\mathbf{n}}_w) \hat{\mathbf{n}}_w \ . \tag{2.14}$$

2.1.3 Radiation Source term

The radiative flux vector can be calculated by integrating intensities over all directions:

$$\mathbf{q}_r = \int_{4\pi} I(\hat{\mathbf{s}}) \hat{\mathbf{s}} d\Omega \ . \tag{2.15}$$

Performing an energy balance over an infinitesimal volume shows that the divergence of the radiative heat flux acts as a source term in the overall energy equation. Therefore, $\nabla \cdot \mathbf{q}_r$ represents the amount of energy deposited or withdrawn from each volume element due to radiation. The divergence of the radiative heat flux can be calculated from the intensity as:

$$\nabla \cdot \mathbf{q}_r = \int_{4\pi} \nabla I(\hat{\mathbf{s}}) \cdot \hat{\mathbf{s}} d\Omega \ , \tag{2.16}$$

where the RHS is the exact integration over all directions of the RTE. By substituting equation (2.12) into equation (2.16), it is possible to obtain an equation for the divergence of the radiation field as:

$$\nabla \cdot \mathbf{q}_r = 4\kappa\sigma T^4 - \kappa \int_{4\pi} I d\Omega \ . \tag{2.17}$$

The scattering term is not present in equation (2.17) because of isotropic scattering: in and out scattering integrated over the direction range compensate each other. The

emission term is obtained by integrating the blackbody intensity over all directions, while usually the absorption term is replaced by the incident radiation (G) which is defined as:

$$G = \int_{4\pi} I d\Omega \ . \tag{2.18}$$

2.2 Radiation modelling

Modelling radiative heat transfer can be a challenging and computationally expensive task due to the long radiation scales and the propagation in virtually all directions. Several models have been developed throughout the years. The main classes which will be reviewed are divided into integral and differential methods.

Integral methods

Integral methods resolve the integral formulation of equation (2.12). A commonly adopted method falling in this category is the Photon Monte Carlo method. A Monte Carlo photon transport simulation consists of launching a number of photon beams starting from location in which a high energy density is encountered and tracing them until fully depleted. Monte Carlo methods can achieve a high degree of accuracy, being able to resolve exactly the RTE to an extent that is controllable by simulation parameters. A drawback of these methods is the high computational cost, having to trace several rays (up to millions) in order to obtain a statistically significant result. Another example of an integral method is the zonal method, proposed by Hottel and Cohen [13]. In the zonal method, the volume and the surface of the enclosure are divided into several zones assuming constant temperature and radiation properties within the zone. Total Exchange factors are evaluated (surface-volume, volume-volume and surface-surface). Therefore, the RTE is reduced into a set of nonlinear algebraic equations solvable using various numerical matrix inversion techniques. The zonal method was popular in the past due to its simple implementation, but the need to invert full matrices causes high computational expenses when dealing with complex problems or optically thick cases.

Differential methods

Differential methods solve the differential formulation of the RTE by discretizing equation (2.12) in a control volume formulation. Examples of these methods are the Spherical harmonics method, discrete ordinates method and the finite volume method. Because of the formulation of these methods, they are more easily coupled with CFD simulations where a discrete spatial grid is required to obtain a solution.
In the spherical harmonics approximation (P_N) method, the intensity is expressed by a

series of spherical harmonics that divide the RTE into a set of first order Partial Differential Equations (PDE) [14] that can be solved with standard PDE solvers. The P_N approximation has been extensively used in its lowest-order approximation P_1 for one and two dimensional problems, but the complexity of P_N increases rapidly with higher order spherical harmonics required for three dimensional geometries. Furthermore, the P_N method performs poorly when compared to other methods for highly non isotropic radiation field and in optically thin limit [14].
One of the most popular method for modelling the RTE equation is the Discrete Ordinates method (DO or S_N approximation). Akin to the P_N approximation, DO method is a tool to transform the RTE into a set of partial differential equations [15]. The discrete ordinates method is based on an angular discretization of the intensity propagation directions, discretizing the directional dependence of the RTE with a finite difference formulation. This method results in a fairly simple implementation and it is particularly popular because of the easy coupling potential with CFD codes, but suffers of some severe drawbacks such as ray effect, false scattering and non-conservation of radiative energy [15]. Moreover the set of discrete ordinates must satisfy the so called zero, first and second moments, a set of conditions on the ordinates and their weights that guarantee the correct implementation of the method.

2.3 Finite Volume Method

The Finite Volume Method (FVM) was first developed from Briggs [16], as an alternative to the discrete ordinates method in the field of neutron transport and further developed by Raithby and Chui [17] for thermal radiative transfer. As discussed in the previous section, discrete ordinates method requires the set of ordinates to satisfy several conditions, making it difficult to develop a flexible scheme for unstructured meshes. Moreover, the DO method does not ensure energy conservation since it is based on a finite differencing scheme. Therefore, a complete finite volume formulation was proposed in order to ensure conservation of radiant energy and simplify the implementation for complex geometries. In addition, FVM is shown to be unaffected by ray effect and to experience a reduced false scattering when compared to DO method [15].
For these reasons finite volume method for radiation transport calculation is slowly acquiring popularity in the field of thermal radiative transport prediction. The method provides a good compromise between computational requirements and solution accuracy. The starting point of the finite volume method is the integration of the RTE (equation (2.12)) over the control volume:

$$\int_V \nabla I \cdot \hat{\mathbf{s}} dV = \int_V \kappa I_b dV - \int_V \kappa I dV - \int_V \sigma_s I dV + \int_V \frac{\sigma_s}{4\pi} \int_{4\pi} I d\Omega dV \ . \tag{2.19}$$

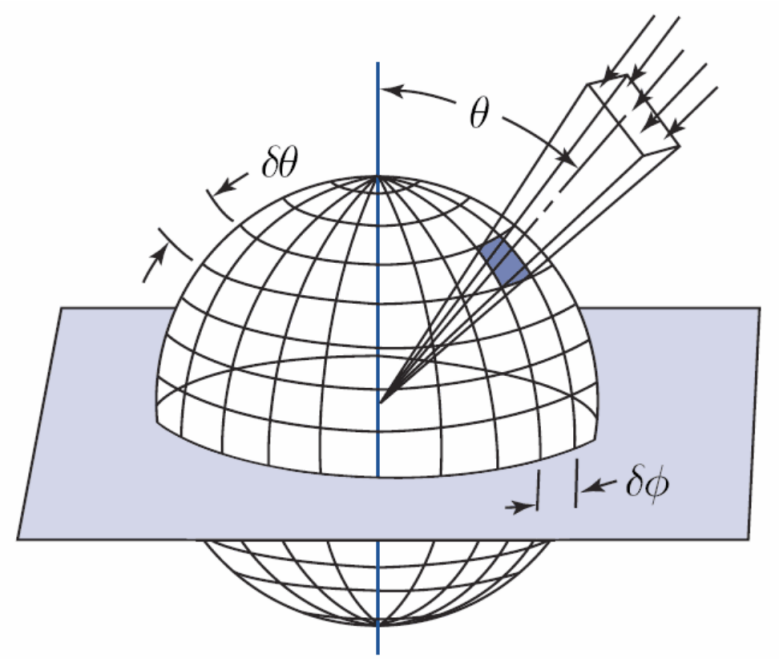

FIGURE 2.2: solid angle Ω and angular variables θ and ϕ

By moving the unit direction vector in the ∇ operator and making use of the divergence theorem :

$$\int_V \nabla I \cdot \hat{\mathbf{s}} dV = \int_V \nabla \cdot (I\hat{\mathbf{s}}) dV = \int_A I\hat{\mathbf{n}} \cdot \hat{\mathbf{s}} dA \ , \tag{2.20}$$

where A represents the faces of the control volume. In order to represent the directional behaviour in a finite volume fashion, the whole range of directions (a full sphere) is discretized in a set of control angles. A figurative representation of the "control angle discretization" of the direction range is shown in figure 2.2. Hence, substituting equation (2.20) into equation (2.19), integrating over the control angle and changing order to the integrals yields:

$$\begin{aligned} \int_A \int_{\Omega_i} I\hat{\mathbf{n}} \cdot \hat{\mathbf{s}} d\Omega dA = \int_V \int_{\Omega_i} \kappa I_b d\Omega dV - \int_V \int_{\Omega_i} \kappa I d\Omega dV - \\ \int_V \int_{\Omega_i} \sigma_s I d\Omega dV + \int_V \int_{\Omega_i} \frac{\sigma_s}{4\pi} \int_{4\pi} I d\Omega' d\Omega dV \ . \end{aligned} \tag{2.21}$$

The implementation of FVM assumes constant intensity throughout the control angle Ω_i. The resulting discretized equation is then:

$$\sum_k I_{ki}(\mathbf{n}_k \cdot \mathbf{s}_i) A_k = (S_{pi} - (\kappa_p + \sigma_{sp}) I_{pi}) V \Omega_i \ , \tag{2.22}$$

where:

$$S_{pi} = \kappa_p I_{bp} + \frac{\sigma_{sp}}{4\pi} \sum_{j=1}^{n} I_{pj} \Omega_j \ , \tag{2.23a}$$

$$\mathbf{s}_i = \int_{\Omega_i} \hat{\mathbf{s}} d\Omega \ , \tag{2.23b}$$

$$\mathbf{n}_k = \int_A \hat{\mathbf{n}} dA \ . \tag{2.23c}$$

The subscripts k and p identify variables on the faces and in the nodal point of the control volume ($k = n, s, w, e, t, b$) respectively, while the subscript i denotes the propagation direction.
Ω_i, Ω_j and integrated unit direction vector $\mathbf{s}_i$ are expressed as a function of two angular variables: polar angle θ and azimuthal angle ϕ, defined as in figure 2.2. From this definition, the infinitesimal solid angle is calculated as

$$d\Omega \ = \sin\theta d\theta d\phi \ ,$$

while the unit direction vector is defined as:

$$\hat{\mathbf{s}} = \cos\phi \sin\theta \hat{\mathbf{i}} + \sin\phi \sin\theta \hat{\mathbf{j}} + \cos\theta \hat{\mathbf{k}} \ .$$

Boundary conditions are developed by integrating equation (2.13) over the surface area and over the control angle, hence for diffuse boundaries ($\rho^s = 0$):

$$I_{w,out} = \epsilon_w I_{bw} + (1 - \epsilon_w) \frac{\sum_{\mathbf{n}_w \cdot \mathbf{s}_i < 0} I_{w,in} |\mathbf{n}_w \cdot \mathbf{s}_i|}{\sum_{\mathbf{n}_w \cdot \mathbf{s}_i > 0} (\mathbf{n}_w \cdot \mathbf{s}_i)} \ . \tag{2.24}$$

The only remaining unknown is the facial intensity I_{ki} that must be derived from the nodal intensity I_{pi} by means of a spatial discretization schemes

2.3.1 Spatial discretization schemes

Several schemes were developed to discretize the facial intensity from the nodal intensity, characterized by different accuracy and computational requirements. Only the most important are reviewed in this report.

The simplest discretization scheme is the STEP scheme. The STEP scheme assumes the facial intensity to be equal to the upstream nodal intensity. Therefore $I_{ki} = I_{pi}$ if $\mathbf{n}_k \cdot \mathbf{s}_i > 0$ and $I_{ki} = I_{Ki}$ if $\mathbf{n}_k \cdot \mathbf{s}_i < 0$, where K represents the neighbouring cells corresponding to the surface area k. The result of the implementation of this scheme is a fully explicit formulation of equation (2.22):

$$I_{pi} = \frac{S_{pi} V \Omega_i - \sum_{\mathbf{n}_k \cdot \mathbf{s}_i < 0} I_{Ki} (\mathbf{n}_k \cdot \mathbf{s}_i) A_k}{(\kappa_p + \sigma_{sp}) V \Omega_i + \sum_{\mathbf{n}_k \cdot \mathbf{s}_i > 0} (\mathbf{n}_k \cdot \mathbf{s}_i) A_k} \ . \tag{2.25}$$

Because I_{Ki} is required for those faces for which $\mathbf{n}_k \cdot \mathbf{s}_i < 0$, it is sufficient to implement a marching scheme to obtain I_{pi}. If $\sigma_s \neq 0$ or $\rho_w \neq 0$ the propagation directions are coupled, which requires the iteration of equation (2.25) until the desired tolerance is met.
The STEP scheme results in a simple formulation and, like a fully implicit finite difference, non-physical results [15]. The drawback of using this method is the occurrence of a large truncation error and therefore a low degree of accuracy. Despite the drawbacks, due to the stability and the simple implementation, the STEP scheme is currently the most used spatial discretization scheme for FVM.

In order to reduce the truncation error associated with the use of the simple STEP scheme, numerous alternatives have been proposed. The most popular scheme is the diamond scheme, where the facial intensity is calculated as arithmetical average of the two neighbouring nodal intensities. The diamond scheme is still a first order discretization scheme but is proven to produce more accurate results when compared to the simple STEP scheme [15]. A severe limitation of the diamond scheme is dictated by stability issues. As Modest reports [15] different studies using the diamond scheme encounter non-physical intensities, either negative or higher than the sum of incoming plus emitted intensity. The occurrence of these nonphysical intensities has not been fully clarified yet.

The CLAM scheme is a second order bounded scheme that discretizes the facial intensity with a three-point approximation, requiring the knowledge of the upstream and downstream nodal intensities, as well as the nodal intensity from the second upstream cell. The facial intensity is then calculated as:

$$I_k = \begin{cases} I_u + \psi(I_d - I_u) & \text{if } 0 \leq \psi \leq 1 \\ I_u & \text{otherwise} \end{cases} , \tag{2.26}$$

$$\psi = \frac{I_u - I_{uu}}{I_d - I_{uu}} , \tag{2.27}$$

where subscript u and uu denote respectively first and second node in the upstream direction, while subscript d denotes the first node in the downstream direction.

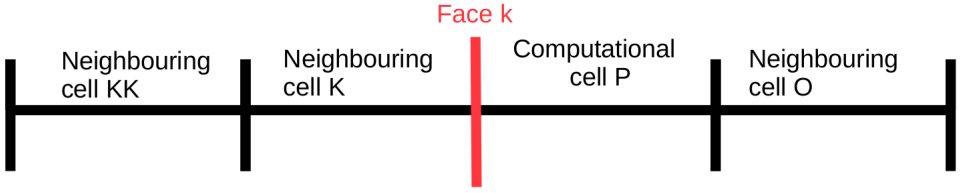

FIGURE 2.3: Indexes of neighbouring cells starting from computational cell p and face k

The CLAM scheme results in a complicated and coupled formulation, since the set of

equations become implicit and the intensity can no longer be calculated in a single sweep. In order to avoid an implicit formulation of equation (2.22), the solution is first guessed from the STEP scheme, subsequently correcting with a source term, S_{clam} derived in the passages (2.28). In this derivation subscript KK denotes the neighbouring cell of K in k direction, while O represents the neighbouring cell of p in direction $-k$. The subscript i is dropped for simplicity. A graphical representation of the neighbouring cells indices is shown for a 1D configuration in figure 2.3.
Implementing the CLAM scheme at the LHS of equation (2.22) yields:

$$\sum_{\mathbf{n}_k\cdot\mathbf{s}_i>0}(I_p+\psi_p(I_K-I_p))(\mathbf{n}_k\cdot\mathbf{s})A_k+\sum_{\mathbf{n}_k\cdot\mathbf{s}_i<0}(I_K+\psi_K(I_p-I_K))(\mathbf{n}_k\cdot\mathbf{s})A_k\ , \tag{2.28a}$$

where parameters ψ_p and ψ_K are given from equation (2.27) as:

$$\psi_p=\begin{cases}\frac{I_p-I_O}{I_K-I_O} & \text{if } 0\leq\psi_p\leq 1\\ 0 & \text{otherwise}\end{cases}\ , \tag{2.28b}$$

$$\psi_K=\begin{cases}\frac{I_K-I_{KK}}{I_p-I_{KK}} & \text{if } 0\leq\psi_K\leq 1\\ 0 & \text{otherwise}\end{cases}\ . \tag{2.28c}$$

It is possible to extract the additional unknown terms rising from the CLAM scheme as:

$$\sum_{\mathbf{n}_k\cdot\mathbf{s}_i>0}I_p(\mathbf{n}_k\cdot\mathbf{s})A_k+\sum_{\mathbf{n}_k\cdot\mathbf{s}_i<0}I_K(\mathbf{n}_k\cdot\mathbf{s})A_k+S_{clam,p}\ , \tag{2.28d}$$

where:

$$S_{clam,p}=\sum_{\mathbf{n}_k\cdot\mathbf{s}_i>0}\psi_p(I_K-I_p)(\mathbf{n}_k\cdot\mathbf{s})A_k+\sum_{\mathbf{n}_k\cdot\mathbf{s}_i<0}\psi_K(I_p-I_K)(\mathbf{n}_k\cdot\mathbf{s})A_k\ . \tag{2.28e}$$

Equation (2.22) then reduces to:

$$I_{pi}=\frac{S_{pi}V\Omega_i-\sum_{\mathbf{n}_k\cdot\mathbf{s}_i<0}I_{Ki}(\mathbf{n}_k\cdot\mathbf{s}_i)A_k-S_{clam,p}}{(\kappa_p+\sigma_{sp})V\Omega_i+\sum_{\mathbf{n}_k\cdot\mathbf{s}_i>0}(\mathbf{n}_k\cdot\mathbf{s}_i)A_k}\ , \tag{2.28f}$$

where $S_{clam,p}=0$ equals the implementation of the STEP scheme. Equation (2.28f) is iterated using the calculated value of $S_{clam,p}$ at the previous iteration until the desired tolerance is met. Despite the additional computational time required in order to calculate $S_{clam,p}$ and to iterate the solution, CLAM scheme provides much more accurate solution to the RTE, specially in those limits in which first order solutions fail, as for high optical thickness (see section 2.3.2).

For the present work, in order to investigate the difference between first and second order spatial discretization, only two schemes were implemented: the STEP scheme and the CLAM scheme. The performance of these two schemes will be discussed and

compared in a Cartesian coordinate configuration in the next section.

2.3.2 Cartesian coordinates

When dealing with Cartesian coordinates the implementation of equations (2.25) and (2.28f) is relatively simple since the area normal unit vector $\mathbf{n}_k$ is independent of the spatial location ($\mathbf{n}_x = \hat{\mathbf{i}}$, $\mathbf{n}_y = \hat{\mathbf{j}}$ and $\mathbf{n}_z = \hat{\mathbf{k}}$). The calculation of the term $(\mathbf{n}_k \cdot \mathbf{s}_i)A_k$ is then straightforward. Intensity in a Cartesian domain can be calculated with the STEP scheme identifying eight regions of the angular domain, each corresponding to different incoming and outgoing directions:

- $0 \leq \phi < \pi/2$, $0 \leq \theta < \pi/2$, incoming directions: bottom, south west
- $\pi/2 \leq \phi < \pi$, $0 \leq \theta < \pi/2$, incoming directions: bottom, south east
- $\pi \leq \phi < 3\pi/2$, $0 \leq \theta < \pi/2$, incoming directions: bottom, north east
- $3\pi/2 \leq \phi < 2\pi$, $0 \leq \theta < \pi/2$, incoming directions: bottom, north west
- $0 \leq \phi < \pi/2$, $\pi/2 \leq \theta < \pi$, incoming directions: top, south west
- $\pi/2 \leq \phi < \pi$, $\pi/2 \leq \theta < \pi$, incoming directions: top, south east
- $\pi \leq \phi < 3\pi/2$, $\pi/2 \leq \theta < \pi$, incoming directions: top, north east
- $3\pi/2 \leq \phi < 2\pi$, $\pi/2 \leq \theta < \pi$, incoming directions: top, north west

Each zone is then treated separately sweeping from the boundaries corresponding to the incoming directions until the outgoing boundaries are reached. If the CLAM scheme is employed, from the first guess the clam source term is calculated and the domain sweep is iterated until a converged solution is reached.

For verification purposes the 3D benchmark case from Sakurai et al. [18] has been simulated.

In his paper, Sakurai develops an analytical expression to exactly resolve radiative transport in a cubic enclosure with $L_x = 1$, $L_y = 1$, $L_z = 1$ which contains an emitting-absorbing grey gas. In order to achieve an analytical solution and to verify the effects of a non-uniform temperature profile, the chosen temperature distribution (fixed) is defined as follows:

$$T(x, y, z) = \left(\sin \frac{x\pi}{L_x} \sin \frac{y\pi}{L_y} \sin \frac{z\pi}{L_z} \cdot \frac{\pi}{\sigma} \right)^{\frac{1}{4}} . \tag{2.29}$$

Figure 2.4 shows the domain as well as the location at which the radiation source is calculated. The walls are cold ($T = 0$ K) and black ($\epsilon = 1$). The solution is obtained

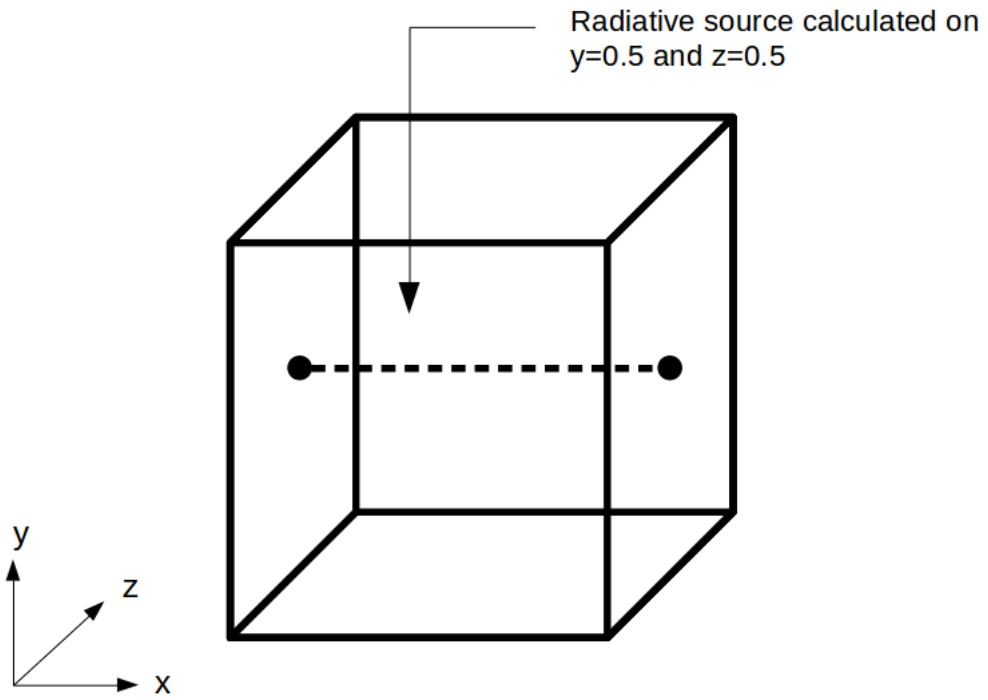

FIGURE 2.4: Cubic enclosure for 3D Cartesian validation

analytically for a single direction $\hat{\mathbf{s}}$ as:

$$I(x,y,z,\hat{\mathbf{s}}) = I_{b,w}e^{-\kappa s} + \\ +\kappa e^{-\kappa s}\int_0^s e^{-\kappa s'}\left(\sin\frac{(x_0+\xi s')\pi}{L_x}\sin\frac{(y_0+\eta s')\pi}{L_y}\sin\frac{(z_0+\mu s')\pi}{L_z}\right)ds' \ , \tag{2.30}$$

where ξ, η and μ are the direction cosines, and s is the distance from the boundary originating the ray, calculated as

$$s = \frac{x-x_0}{\xi} = \frac{y-y_0}{\eta} = \frac{z-z_0}{\mu} \ , \tag{2.31}$$

and x_0, y_0, z_0 represents the positions at the wall. The integration of equation (2.32) yields the following expression:

$$I(x,y,z) = \frac{\kappa e^{-\kappa s}}{4}(I_1 + I_2 - I_3 - I_4) \ , \tag{2.32}$$

with I_1, I_2, I_3 and I_4 given as:

$$I_n = \frac{\kappa e^{-\kappa s}\sin(a_n+b_n s) - b_n e^{-\kappa s}\cos(a_n+b_n s) - \kappa\sin a_n + b_n\cos a_n}{\kappa^2+b_n^2} \ . \tag{2.33}$$

Finally coefficients $a_1 - a_4$ and $b_1 - b_4$ are calculated as:

$$a_1 = +\frac{x_0\pi}{L_x} - \frac{y_0\pi}{L_y} + \frac{z_0\pi}{L_z}, \qquad b_1 = +\frac{\xi\pi}{L_x} - \frac{\eta\pi}{L_y} + \frac{\mu\pi}{L_z}, \tag{2.34a}$$

$$a_2 = -\frac{x_0\pi}{L_x} + \frac{y_0\pi}{L_y} + \frac{z_0\pi}{L_z}, \qquad b_2 = -\frac{\xi\pi}{L_x} + \frac{\eta\pi}{L_y} + \frac{\mu\pi}{L_z}, \tag{2.34b}$$

$$a_3 = +\frac{x_0\pi}{L_x} + \frac{y_0\pi}{L_y} + \frac{z_0\pi}{L_z}, \qquad b_3 = +\frac{\xi\pi}{L_x} + \frac{\eta\pi}{L_y} + \frac{\mu\pi}{L_z}, \tag{2.34c}$$

$$a_4 = -\frac{x_0\pi}{L_x} - \frac{y_0\pi}{L_y} + \frac{z_0\pi}{L_z}, \qquad b_4 = -\frac{\xi\pi}{L_x} - \frac{\eta\pi}{L_y} + \frac{\mu\pi}{L_z}. \tag{2.34d}$$

In order to achieve a correct solution, intensities from 10000 independent directions were calculated. The incident radiation was then calculated using equation (2.18) where the integral was replaced by a summation over the solid angles, and Ω_i was calculated as explained for the finite volume method.
Results for different optical thicknesses have been compared to the simulation results using both STEP and CLAM scheme.
Absorption coefficient has been varied over a broad range (0.01 - 10 m^{-1}) in order to verify the performance of the FVM for different optical thickness. Simulations have been performed for different mesh sizes (both for spatial and angular discretization), in order to assess the sensitivity of the two methods to mesh variations.

In Figures 2.5 to 2.9 the diamonds represent the analytical solution, while dashed-dotted line, +, ∘ and solid line represent respectively the STEP scheme and the CLAM scheme on a coarse mesh ($N_x = N_y = N_z = 10$, $N_\theta = 2$, $N_\phi = 4$), and on a fine mesh ($N_x = N_y = N_z = 50$, $N_\theta = 8$, $N_\phi = 12$)

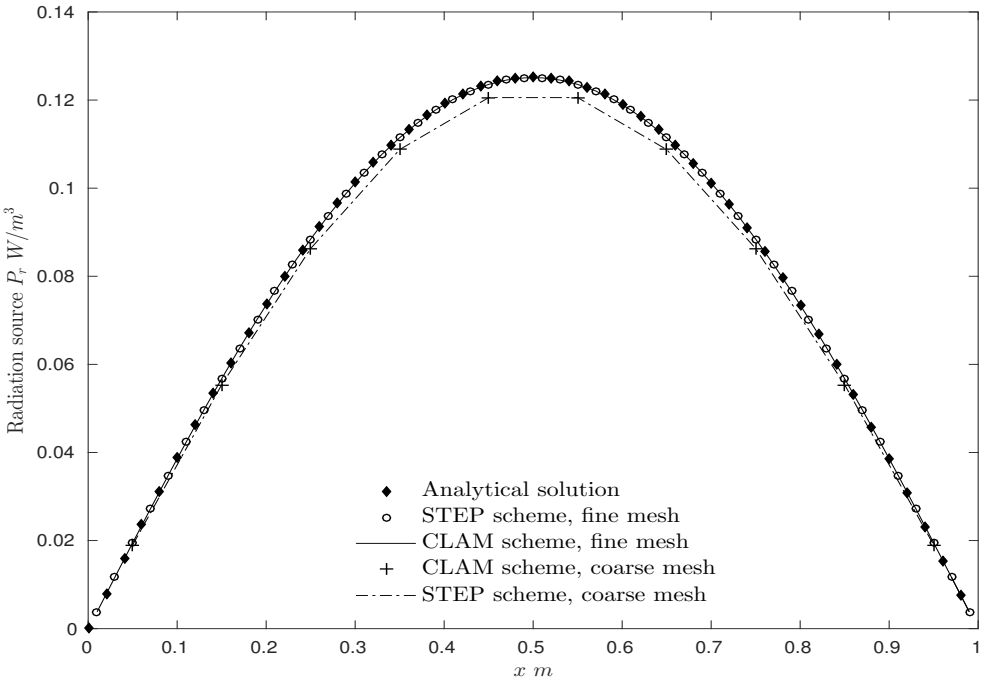

FIGURE 2.5: Validation as for Sakurai et al [1], optically very thin case: $\kappa = 0.01$

From figure 2.5 and 2.6 it is possible to conclude that $S_{clam,p} \to 0$ in the optically thin

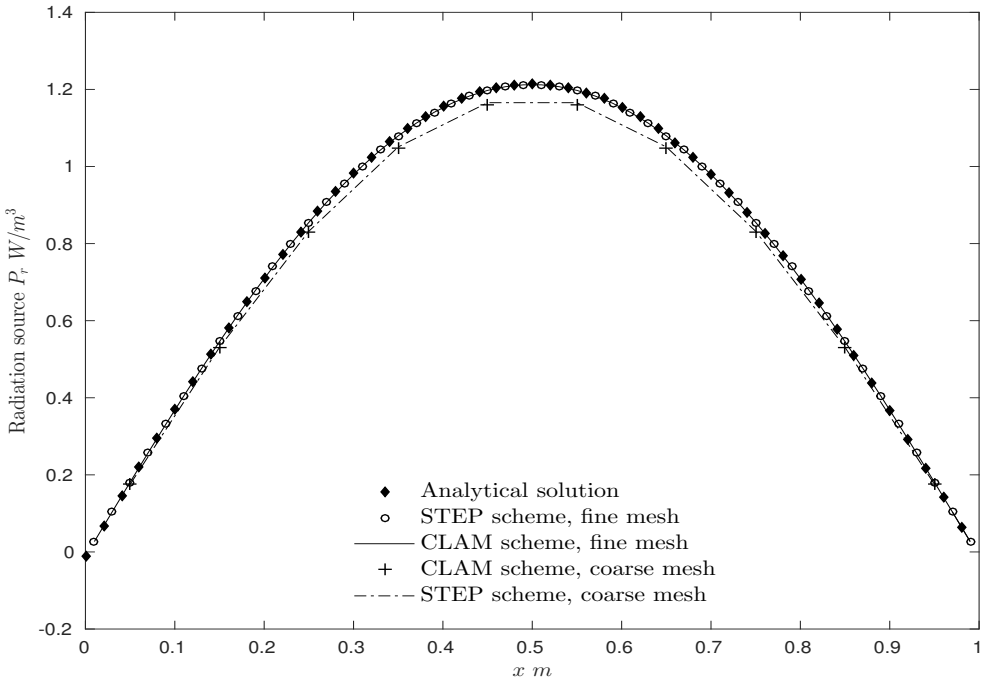

FIGURE 2.6: Validation as for Sakurai et al [1], optically thin case: $\kappa = 0.1$

limit. Therefore the solution for the STEP and the CLAM scheme are indistinguishable. It is also possible to observe that the FVM performs good in the thin limit being able to reproduce almost identically the analytical solution with a relatively fine grid. The solutions obtained by the coarse grid are slightly under-predicted, but still rather close to the analytical solution.

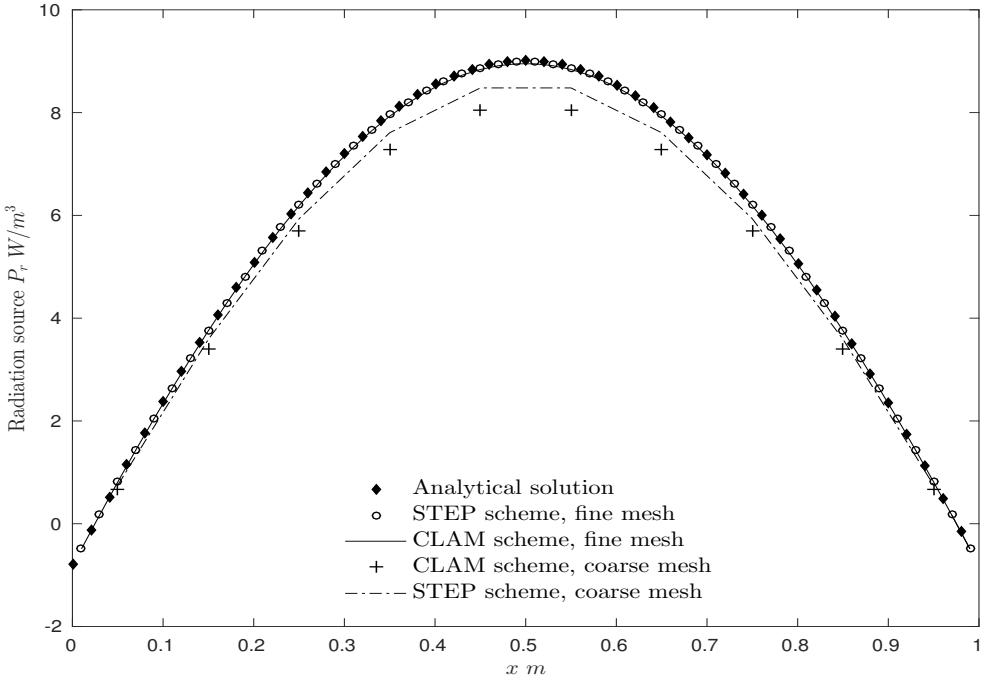

FIGURE 2.7: Validation as for Sakurai et al [1], optically intermediate case: $\kappa = 1$.

For an optically intermediate medium (absorption coefficient $\kappa = 1\ m^{-1}$, in figure 2.7) both methods are still coinciding with the analytical solution on the fine grid. Results on the coarse grid, on the other hand, are not satisfactory. Surprisingly, the STEP scheme on the coarse grid performs better than the CLAM scheme that shows a higher mesh sensitivity.

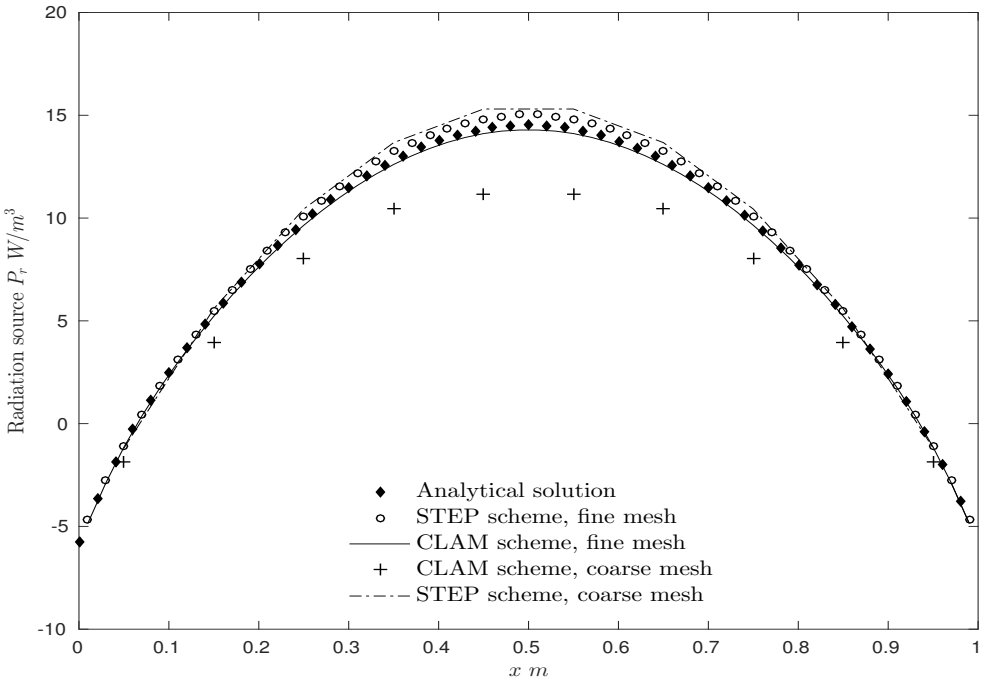

FIGURE 2.8: Validation as for Sakurai et al [1], optically thick case: $\kappa = 5$.

On the other hand, when the medium becomes optically thick ($\kappa = 5$ and $10\ m^{-1}$ in figures 2.8 and 2.9, respectively) the two methods show a remarkable difference. the STEP scheme heavily over predicts the radiation source with the error increasing with the absorption coefficient. The results are affected by grid refinement, since the solution moves closer to the analytical data for finer grids, but a noticeable error is still observed on the fine grid. The CLAM scheme shows the same behaviour as for the optically intermediate case. The deviation of the results obtained with the coarse grid from the analytical solution is significantly large, while results obtained by the fine accurately describe the exact solution. Once again, the CLAM scheme proves to be very mesh sensitive.

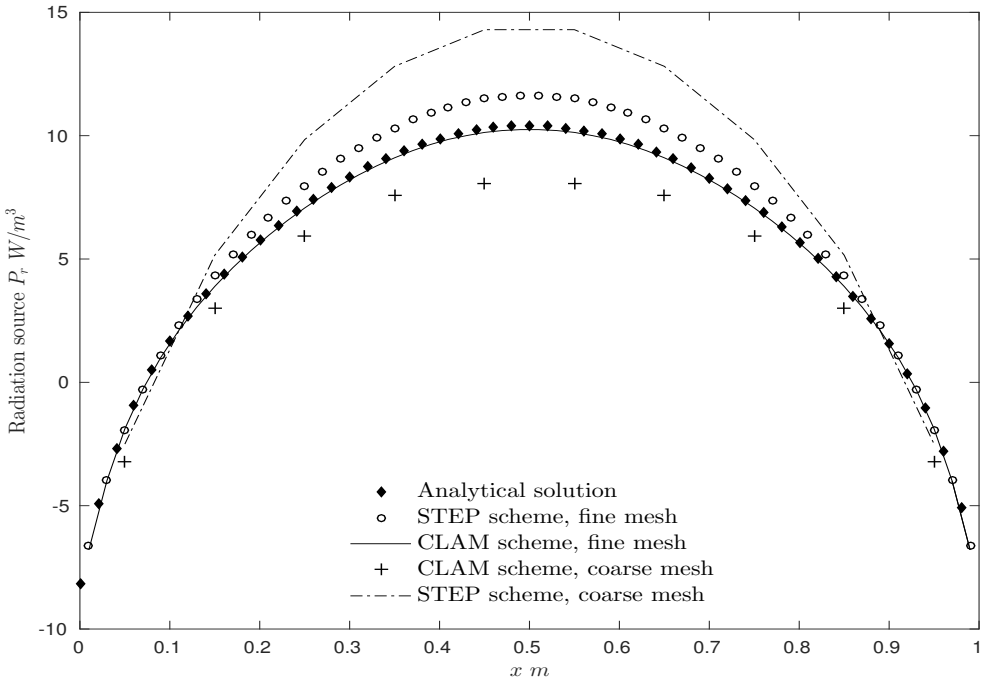

FIGURE 2.9: Validation as for Sakurai et al [1], optically very thick case: $\kappa = 10$.

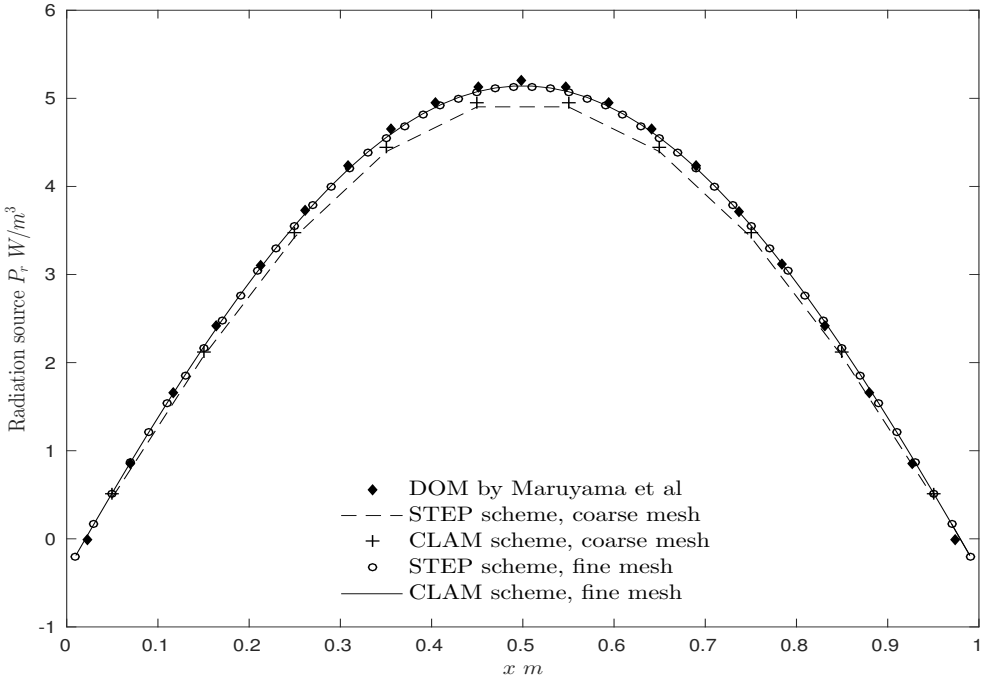

FIGURE 2.10: absorption coefficient 0.5, scattering coefficient 0.5

An absorbing-emitting and isotropically scattering case, taken from simulations of Maruyama et al [19], has also been compared with the FVM simulation in order to validate the code with isotropic scattering. The domain and temperature distribution are the same as the cases above, but $\kappa = 0.5$ and $\sigma_s = 0.5$. Results in figure 2.10 show good agreement with the discrete ordinate code used by Maruyama et al. [19].

A further benchmark case from Burns and Christen [2] is used as validation for a media with a spatially varying absorption coefficient. The cubic enclosure is the same as in the previous case, as well as the boundary conditions (black cold walls). The medium is isothermal and the absorption coefficient is spatially varying as:

$$\kappa(x,y,z) = 0.9 \cdot \left(1 - 2\left|\frac{x}{L}\right|\right)\left(1 - 2\left|\frac{y}{L}\right|\right)\left(1 - 2\left|\frac{z}{L}\right|\right) + 0.1 \ . \tag{2.35}$$

κ is then symmetric with respect to the center of the enclosure, with a maximum value of 1 m^{-1} in the center, decreasing till a minimum of 0.1 m^{-1} on the walls. The fine grid of the previous case has been chosen as a base case. Different simulations have been performed by refining separately the spatial and the angular grid to perform a grid sensitivity analysis. The angularly refined grid has $N_\theta = 16$ and $N_\phi = 24$ while the spatially refined grid has $N_x = N_y = N_z = 100$.

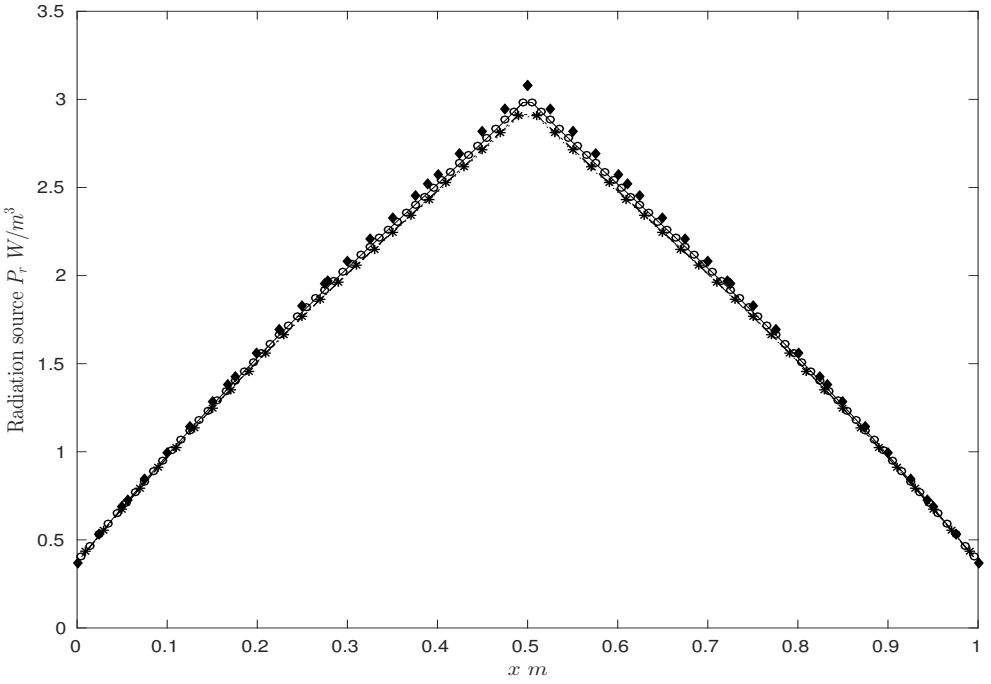

FIGURE 2.11: varying κ; dotted line: STEP base case, *: CLAM base case, dashed line: STEP angle refined, dashed dotted line: CLAM angle refined, solid line: STEP spatially refined, ○: CLAM spatially refined, ♦: benchmark from Burns and Christen [2]

The CLAM scheme is noticed to perform slightly better although the difference between the two methods appears to be minimal due to the overall low κ. An analysis of the three used grids shows that a spatial refinement is generally preferred over an angular refinement, being 96 directions (8x12) enough to have a correct converged solution. Despite having a larger deviation than the previous case, the results show satisfactory agreement with the benchmark case. On the other hand, the need for a refined grid shows the lower performance of FVM when a variable absorption coefficient is considered.

2.4 Mathematical description of TRI in a fluctuating thermal field

In this section a mathematical derivation of the length scales of radiative emission and absorption will be performed for the simple case of an absorbing - emitting grey gas. This derivation will provide a description of the transition of radiative heat transfer from a long-range phenomena to a short-range phenomena. Furthermore, the influence of this transition in a fluctuating thermal field will be analyzed.

The theoretical framework for this derivation is a cubic domain, periodic in three directions that experiences a homogeneous and isotropic fluctuating thermal field. Temperature and velocity can be described by a mean and a fluctuating value: $X = \overline{X} + X'$ (where $\overline{X}$ denotes the mean and X' denotes the fluctuation). Mean temperature as well as mean velocities in the cubic enclosures are forced to zero, (i.e. $T = T'$ and $u_j = u_j'$) and conductive effects are neglected ($k = 0$) in order to highlight the effects of radiative transfer. The energy equation thus becomes:

$$\frac{\partial T}{\partial t} + \frac{\partial u_j T}{\partial x_j} = -\frac{\nabla \cdot \mathbf{q}_r}{\rho c_p} \ , \tag{2.36}$$

where for simplicity $P_r = \nabla \cdot \mathbf{q}_r$. Where P_r can be further decomposed into an emission and an absorption term:

$$P_r = \kappa E_m - \kappa G \ . \tag{2.37}$$

Emission represents the stabilizing effect of the net radiative source term in the energy equation, while incident radiation acts as a source of fluctuations. In order to visualize the influence of radiation over the wavenumbers and to derive the characteristic length scales of radiative heat transfer, Fourier transform can be performed. The three dimensional Fourier transform of a function $f(\mathbf{x})$ is defined as:

$$\widehat{f}(\mathbf{w}) = \int_{-\infty}^{\infty}\int_{-\infty}^{\infty}\int_{-\infty}^{\infty} f(\mathbf{x}) \cdot e^{-i(\mathbf{w}\cdot\mathbf{x})} d\mathbf{x} \ , \tag{2.38}$$

where $\mathbf{w} = (w_1, w_2, w_3)$ is the wavenumber vector and $\mathbf{x} = (x, y, z)$ is the position vector. A Fourier representation $\widehat{f}(\mathbf{w})$ of a function $f(\mathbf{x})$ highlights the dependency of function f on the wavenumber $\mathbf{w}$, displaying the characteristic frequencies of the function and thus providing information on the associated length scales. The transformation of equation (2.36) in Fourier space, accounting for properties of derivation as well as multiplication in Fourier space presented in appendix C), yields:

$$\frac{\partial \widehat{T}}{\partial t} + i(\mathbf{w} \cdot \widehat{\mathbf{u}}) * \widehat{T} = -\frac{\widehat{P_r}}{\rho c_p} \ . \tag{2.39}$$

Equation (2.39) shows the influence of P_r on the instantaneous energy equation in frequency space. $\widehat{P_r}$ can then be used to characterize both the characteristic radiation length scales, as well as the effect produced on $\widehat{T}$. The Fourier transformation of radiative transfer equation (2.12) for a simple emitting - absorbing grey gas in wavenumber space, yields:

$$i(\mathbf{w}\cdot\mathbf{s})\widehat{I} = \kappa(\widehat{I}_b - \widehat{I}) \ , \tag{2.40}$$

where $\mathbf{s}$ is the unit direction vector above defined as $\widehat{\mathbf{s}}$. The caret is omitted for clarity. By rearranging equation (2.40) it is possible to express Fourier modes of intensity I as a function of the Fourier modes of local blackbody intensity I_b. Since $I_b = \sigma T^4/\pi$:

$$\widehat{I} = \left(\frac{\kappa^2}{\kappa^2 + (\mathbf{w}\cdot\mathbf{s})^2} - \frac{i(\mathbf{w}\cdot\mathbf{s})\kappa}{\kappa^2 + (\mathbf{w}\cdot\mathbf{s})^2} \right) \cdot \frac{\sigma\widehat{T^4}}{\pi} \ . \tag{2.41}$$

Because the Fourier transform is a linear operator and the wavenumber vector is independent of intensity propagation direction, it holds that (see Kim et al. [20]):

$$\widehat{G} = \widehat{\int_{4\pi} I d\Omega} = \int_{4\pi} \widehat{I} d\Omega \ . \tag{2.42}$$

Substituting this expression into the Fourier equation of $\widehat{P}_r$, results in:

$$\widehat{P}_r = \kappa \left(4\sigma\widehat{T^4} - \int_{4\pi} \widehat{I} d\Omega \right) \ , \tag{2.43}$$

and finally:

$$\widehat{P}_r = \kappa\sigma\widehat{T^4} \left(4 - \frac{\kappa^2}{\pi} \int_{4\pi} \frac{1}{\kappa^2 + (\mathbf{w}\cdot\mathbf{s})^2} d\Omega + \frac{i\kappa}{\pi} \int_{4\pi} \frac{(\mathbf{w}\cdot\mathbf{s})}{\kappa^2 + (\mathbf{w}\cdot\mathbf{s})^2} d\Omega \right) \ . \tag{2.44}$$

To simplify equation (2.44) two functions are defined, yielding:

$$\widehat{P}_r = \kappa\sigma\widehat{T^4}[4 - \Re(\mathbf{w},\kappa) + i\Im(\mathbf{w},\kappa)] \ , \tag{2.45}$$

with

$$\Re(\mathbf{w},\kappa) = \frac{\kappa^2}{\pi} \int_{4\pi} \frac{1}{\kappa^2 + (\mathbf{w}\cdot\mathbf{s})^2} d\Omega \ , \tag{2.46a}$$

$$\Im(\mathbf{w},\kappa) = \frac{\kappa}{\pi} \int_{4\pi} \frac{(\mathbf{w}\cdot\mathbf{s})}{\kappa^2 + (\mathbf{w}\cdot\mathbf{s})^2} d\Omega \ . \tag{2.46b}$$

Equation (2.45) shows the frequency dependency of the emission and the absorption terms in relation to the frequency of T^4 modes. Since equation (2.45) does not involve any convolution, no new frequency is created and the frequency range in which $\widehat{P}_r$ is defined, remains the same as for $\widehat{T^4}$. The emission term within the parenthesis on the RHS is represented by a constant, namely 4. This suggests that emission acts non preferentially on all scales of $\widehat{T}$. By recalling equation (2.39), it can be concluded that emission stabilizes temperature fluctuations independently of the associated frequency.

The two integrals on the RHS, on the other hand, depict the effect of absorption. It can be shown that $\Im(\mathbf{w}, \kappa)$ is three orders of magnitude lower than $\Re(\mathbf{w}, \kappa)$ for the whole absorption coefficient and wavenumber range, and therefore can be neglected. Absorption, contrary to emission, exhibits a preferential behaviour, highlighted by the dependency of $\Re$ over the wavelengths. The analysis of this term results in an indirect observation of the modification of radiative heat transfer characteristic length scales. Plots of $\Re(\mathbf{w}, \kappa)$ and $4 - \Re(\mathbf{w}, \kappa)$ are shown in figure 2.12 and 2.13 for various absorption coefficients.

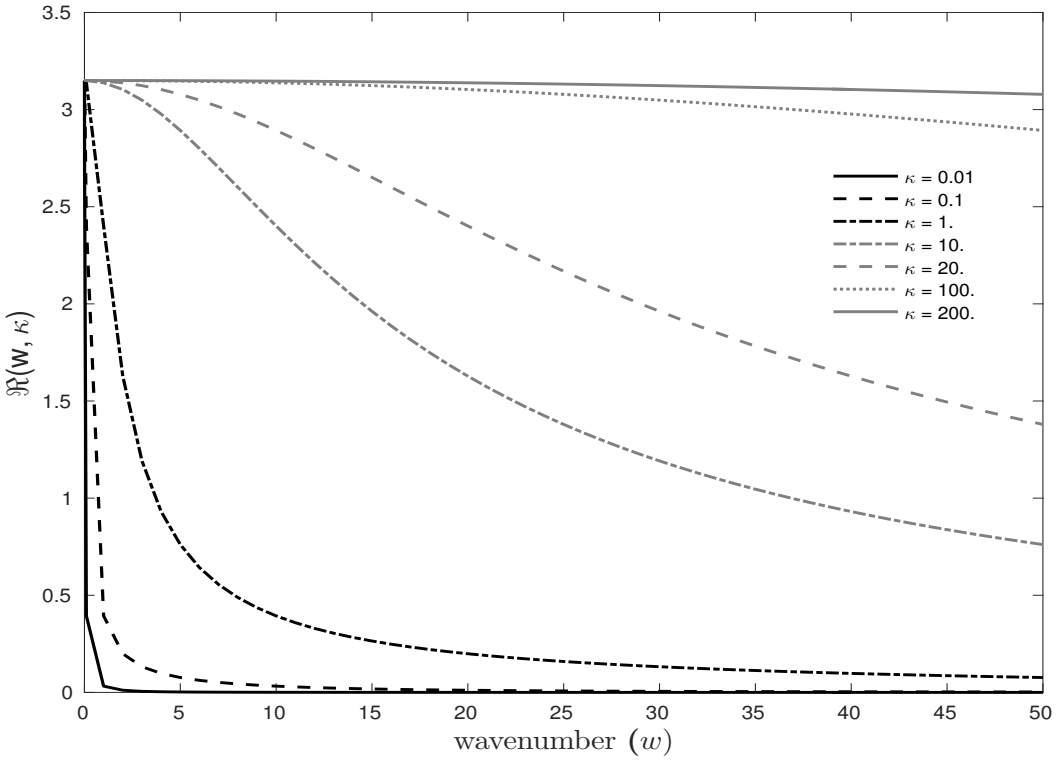

FIGURE 2.12: behaviour of scaling function $\Re(\mathbf{w}, \kappa)$ for different wavenumbers and absorption coefficients κ

Figure 2.12 represents the influence of absorption over different wavelengths. The largest wavenumber of figure 2.12 corresponds to the highest T^4 fluctuating frequency. For smaller absorption coefficients, absorption shows a very negligible influence over T^4 scales. Therefore, fluctuations in temperature do not induce corresponding incident radiation fluctuations, resulting in a fairly non-fluctuating incident radiation field. Since incident radiation is an integral measure of intensity, it can be inferred that the local intensity is not affected by the local temperature fluctuations. Thus intensity fluctuations at all scales are minimized. Since intensity is insensitive to local quantities, it can be concluded that length scales of radiative heat transfer are significantly large, enabling heat transfer between far apart locations. When the absorption coefficient is increased, a more profound influence of incident radiation over the scales can be noticed, with a preferential effect on large scales (high wavelength). In other words, when the absorption coefficient increases, large thermal eddies absorb incoming radiation, causing local

fluctuation of G. Therefore, the absorption becomes more local since it is influenced by smaller scales of temperature. Considering that G represents an indirect measure of intensity, it can be concluded that an increase in the optical thickness results in larger intensity fluctuations, depicting the reduction of radiative heat transfer length scales. If the absorption coefficient is increased extensively, $\Re(\mathbf{w}, \kappa)$ approaches a constant value. When the media is sufficiently optically thick that a beam is absorbed in the close proximity of where it has been emitted, absorption modes are tightly coupled to temperature modes. Therefore, the energy is distributed over wavenumbers in a similar fashion for absorption as for T^4. This effect defines the "optically thick approximation" and confirms the theory stating that in an optically thick media, radiation length scales are so short that radiation can be analyzed in analogy with molecular heat transfer (see Modest [15]).

Moreover, it is possible to notice that an increase in optical thickness corresponds to a stretching of the curve to higher wavenumbers, meaning that the behaviour of temperature scales towards radiation is shifted to smaller wavelengths. By increasing the fluctuation range, the cut-off wavenumber increases and $\Re(\mathbf{w}, \kappa)$ will eventually show an optical thin behaviour ($\Re(\mathbf{w}, \kappa) \approx 0$) also for high absorption coefficients if $\mathbf{w}$ is sufficiently high (i.e. in a turbulent flows, high turbulence levels generate smaller scales which appear to be transparent to radiation).

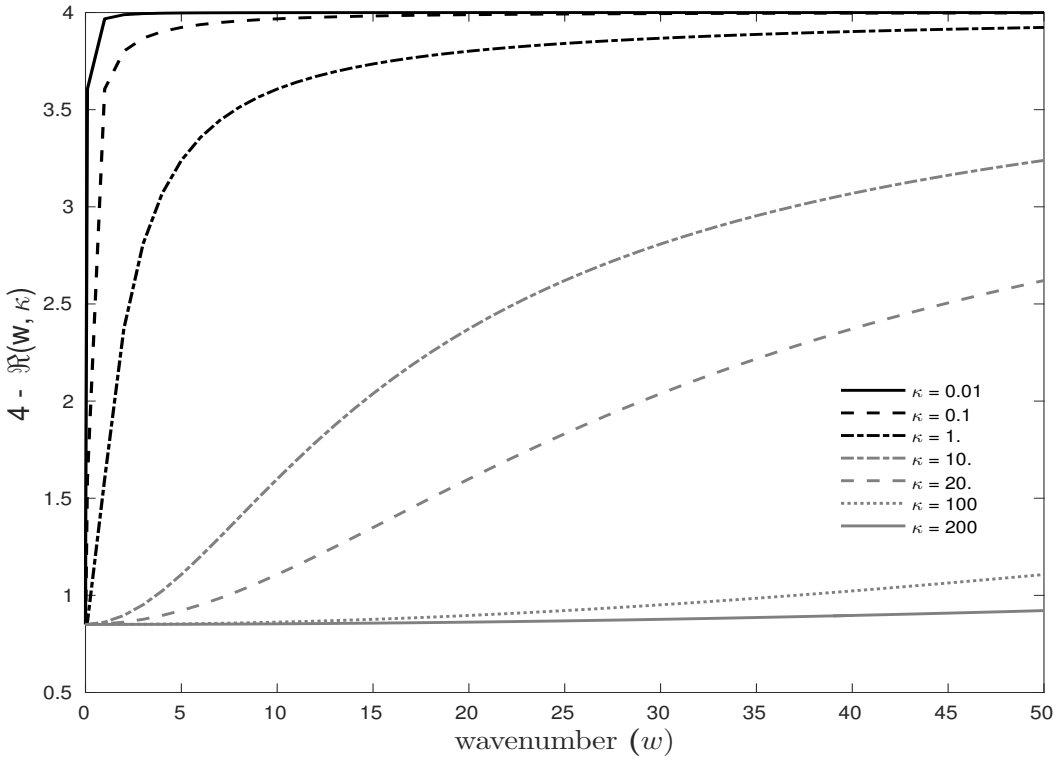

FIGURE 2.13: behaviour of scaling function $4 - \Re(\mathbf{w}, \kappa)$ for different wavenumbers and absorption coefficients κ

Figure 2.13 shows the effect of combined emission and absorption on the scaling of

P_r modes. The absorption tends to reduce $\widehat{P_r}$, decreasing the energy contained in P_r modes. At a low optical thickness, a non-negligible effect of G is observed only on the larger scales, while the higher frequency fluctuations are still dominated by the effect of emission. Upon increasing the optical thickness, the damping effect of incident radiation is visible over all wavenumbers, until reaching the optically thick limit where $\widehat{P}_r = C \cdot \widehat{T^4}$.

The conclusions drawn by the analysis of figures 2.12 and 2.13 are summarized below:

- Radiative heat transfer modes exist in relation with T^4 modes, thus no new frequencies are created by moving from $\widehat{T^4}$ to $\widehat{P_r}$ ($\widehat{T^4}$ frequency range is a direct effect of Reynolds Re and Prandtl Pr number)
- Incident radiation scales, representing intensity beam length, decrease with increased optical thickness. For a low absorption coefficient G fluctuation energy is stored in the low wavenumber range. Therefore, thermal fluctuations do not induce corresponding fluctuations in incident radiation and radiative heat transfer scales are fairly large. On the other hand, by increasing the optical thickness radiative heat transfer can be regarded as a short range phenomena, sensitive to thermal fluctuations at all scales.
- By increasing the frequency range, (i.e. creating smaller temperature scales), the coupling of incident radiation modes with $\widehat{T^4}$ at high wavenumbers tends to fall off confirming the optical thin behaviour of small eddies.
- The combined effect of emission and absorption results in a constant rate withdrawal of energy throughout the scales due to emission and a preferential accumulation of energy on the larger scales due to the effect of absorption.

The conclusion that can be postulated with simple observation of figures 2.12 and 2.13, is that the radiation length scales decrease with increasing optical thickness, reducing the stabilizing effect that radiative emission provides to the temperature field, allowing higher frequency temperature fluctuations. These fluctuations will be localized at larger scales where the effect of incident radiation is amplified. Therefore, radiation provides a direct correlation between small and large thermal structures, resulting in the depletion of small eddies in favour of larger structures. These assumptions will be further investigated with the aid of power density spectra and 2-point autocorrelations in chapter 4.

Chapter 3

Fully developed turbulent channel flow

Turbulence can be defined as a deterministic chaotic behaviour of the flow that undergoes rapid and casual changes both in velocity magnitude and direction. Turbulent flows are opposed to laminar flows where the flow moves along smooth streamlines. Most engineering applications are characterized by a large Reynolds number and deal with turbulent flows. A turbulent flow is characterized by eddies, swirling vortices that enhance the mixing in the flow. The scales of these vortices vary from large structures that carry a high amount of energy to smaller structures characterized by a higher fluctuating frequency. The transfer of energy through the scales of motion can be viewed as a "cascade" of energy. Turbulence kinetic energy is produced at large scales. Large eddies are characterized by a length scale l_0 and a velocity scale $u(l_0)$ comparable to domain size and bulk velocity. Reynolds number of large eddies is therefore comparable to the bulk Reynolds number of the flow. Large vortices break up into smaller eddies due to perturbations and mainly vortex stretching. These eddies undergo similar process producing somewhat smaller vortices. This phenomena continues until the scales are small enough that their associated Reynolds number is in the order of the unity. At these low Reynolds number, viscosity dissipation occurs and turbulence cannot be sustained, thus turbulent kinetic energy is dissipated into heat.

3.1 Direct numerical simulation

Direct numerical simulations entirely resolves the fluid flow, avoiding the use of models to describe turbulence. This method is inherently unsteady, requiring an average in time in order to obtain a solution for statistically steady problems. Because the fluid flow

is completely resolved in DNS, cell volumes must be as small as the smallest scales encountered in the flow. The smallest scales of the flow are in the order of the Kolmogorov scales, that, as derived by Kolmogorov (see [22]) are defined as $\eta_K \approx (\nu^3/\epsilon)^{1/4}$, where ν is the kinematic viscosity of the fluid and ϵ is the viscous dissipation.
Therefore, the maximum element size is $\Delta L = \eta_K$, the number of required mesh points is $N = L/\Delta L = L/\eta_K$ and since ϵ scales with U^3/L, the required number of control volumes scales with Reynolds number as $N^3 \sim Re^{9/4}$. If $Pr > 1$ the required number of control volumes must be increased of a factor $\sqrt{Pr}$ in order to include the smaller scales of thermal turbulence (batchelor scale, see Batchelor [23]).
Moreover the time step should be able to include the development of small scales, therefore $dt \sim t_\eta$, where t_η is the Kolmogorov time scale (time scale of the smallest eddies) defined as $t_\eta = (\nu/\epsilon)^{1/2}$.
Finally the size of the domain must be large enough to reproduce the behaviour of the large eddies.
The high computational requirements allow the use of a such accurate method only for the most simple configurations and low Reynolds number.

3.2 Numerical details

Turbulence radiation interactions are studied by means of coupled DNS and radiation FVM in a fully developed turbulent channel flow. The considered case is periodic in the homogeneous directions (z and y) and bounded by isothermal parallel planes in the x direction. The continuity, momentum and energy equations for a radiating incompressible flow read:

$$\frac{\partial u_i}{\partial x_i} = 0 \ , \tag{3.1}$$

$$\rho \frac{\partial u_i}{\partial t} + \rho u_j \frac{\partial u_i}{\partial x_j} = -\frac{\partial p}{\partial x_j} + \mu \frac{\partial^2 u_i}{\partial x_j^2} \ , \tag{3.2}$$

$$\frac{\partial T}{\partial t} + u_j \frac{\partial T}{\partial x_j} = \frac{k}{\rho c_p} \frac{\partial^2 T}{\partial x_j^2} - \frac{P_r}{\rho c_p} \ , \tag{3.3}$$

where the temperature is assumed to be a passive scalar (i.e. temperature variations do not affect momentum equation). For a more practical implementation it is useful to scale the governing equations on constant values in order to highlight the dependency of the equations on non-dimensional parameters. The scaled equations read:

$$\frac{\partial u_i^*}{\partial x_i^*} = 0 \ , \tag{3.4}$$

$$\frac{\partial u_i^*}{\partial t^*} + u_j^* \frac{\partial u_i^*}{\partial x_j^*} = -\frac{\partial p^*}{\partial x_j^*} + \frac{1}{Re} \frac{\partial^2 u_i^*}{\partial x_j^{*2}} \ , \tag{3.5}$$

$$\frac{\partial \theta^*}{\partial t^*} + u_j^* \frac{\partial \theta^*}{\partial x_j^*} = \frac{1}{RePr} \frac{\partial^2 \theta^*}{\partial x_j^{*2}} - \frac{P_r^*}{RePrPl} \ , \tag{3.6}$$

$$P_r^* = 4\kappa^* {I_b}^* - \frac{\kappa^*}{\pi} \int_{4\pi} I^* d\Omega \ . \tag{3.7}$$

The * represents non-dimensional variables, in the rest of the report will be omitted for simplicity. Non-dimensional variables are defined as follows:

$$u^* = \frac{u}{U_b}, \quad x^* = \frac{x}{\delta}, \quad t^* = t\frac{U}{\delta}, \quad \theta^* = \frac{T - T_c}{T_h - T_c}, \quad \kappa^* = \kappa\delta, \quad I_b^* = \left(\frac{\theta^*}{T_0^+} + 1 \right)^4, \tag{3.8}$$

where U_b is the bulk velocity, δ is the half channel height, while T_h and T_c are respectively the hot and cold wall temperatures. Non dimensional parameters are defined as:

- Reynolds number $Re = U_b\delta/\nu$ ratio of inertial and viscous forces;
- Prandtl number $Pr = k/\rho c_p$ ratio of molecular and turbulent heat transfer
- Planck number $Pl = k\Delta T\delta/\sigma T_c^4$ ratio of molecular and radiative heat transfer
- $T_0^+ = T_c/\Delta T$
- Optical thickness $\tau = \overline{\kappa}|_{x=\delta}\delta$

Coordinate x,y,z represent wall normal, span wise and stream wise direction respectively, with corresponding velocity component u,v,w. A representation of the geometry is shown in figure 3.1:

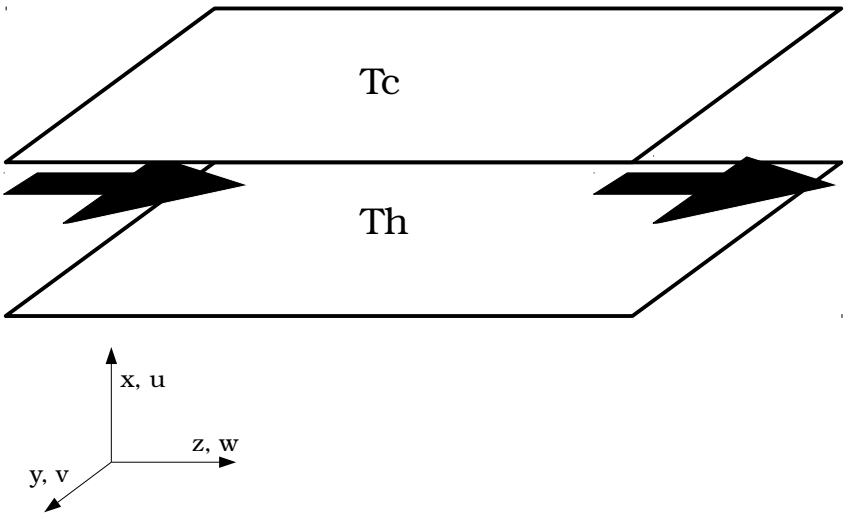

FIGURE 3.1: geometry for channel flow, wall bounded in x direction and periodic in the homogeneous directions

A pressure gradient in the stream wise direction is applied in order to maintain a constant Reynolds number based on bulk velocity. Spectral differentiation with Fourier expansion and periodic boundary condition is used in the homogeneous directions (y and z) with a skew symmetric formulation, while a sixth order staggered compact finite difference is used to discretize spatial derivatives in the wall normal direction. A Pressure correction scheme is applied based on the projection method. For more details and validation of the DNS code the reader is referred to Patel et al [25]. The size of the computational domain in the streamwise and spanwise directions is respectively $4\pi\delta$ and $3\pi/2\delta$. The computational grid is composed of 168x160x192 cells in wall normal, span wise and stream wise direction for a total of 5.16 Million control volumes.

The flow coupling with radiation is done via the net radiative volumetric source in the energy equation. In order to calculate κ when a non-grey gas is simulated, a simple model for the Planck mean absorption coefficient of water vapour is used, where parameters c_0-c_5 and A are provided by Sandia National Laboratories [26]:

$$\kappa = C_k \cdot \left[c_0 + c_1 \left(\frac{A}{T}\right) + c_2 \left(\frac{A}{T}\right)^2 + c_3 \left(\frac{A}{T}\right)^3 + c_4 \left(\frac{A}{T}\right)^4 + c_5 \left(\frac{A}{T}\right)^5 \right] . \tag{3.9}$$

C_k is a parameter that enables to artificially tune the optical thickness of the system without having to increase the size of the domain. With this technique effects of different optical depths on turbulent radiation interactions can be investigated. Directional dependency is discretized with the use of an angular grid of 8x12 elements, resulting in a set of 96 independent directions.
In order to reduce the high computational requirements for radiative transfer solver, an attempt has been made by solving the RTE and thus calculating the net radiative heat source every five flow iterations and on a coarser grid, as done by Zhang et al. [3]. Specifically, the grid was two time coarser in every direction, resulting in a 84x80x96 grid. A Linear interpolation was employed from the fine to the coarse grid, while four order bi-cubic spline was used to transfer the radiative volumetric source from the coarse to the fine grid. Unfortunately, the results did not show a satisfactory accuracy, probably due to the fact that FVM is used for radiation instead of the more accurate Monte Carlo method as for Zhang et al. [3]. Particularly, energy spectra showed bizarre behaviour at the higher wavenumbers, where an oscillating pattern due to the interpolation scheme was observed. Due to the above mentioned reasons the final results presented consist of the calculation of the RTE every time step and in the full grid. The excessive computational expenses associated with the CLAM scheme did not allow the possibility to perform all simulations with the CLAM scheme. Therefore, to keep the report consistent, the STEP scheme has been used for all simulations, leaving the investigation of TRI with a more accurate solver for future developments. The value of τ shown in table 3.1 when $\kappa = f(T)$ is only representative of the magnitude of the optical thickness of the system; the real τ will oscillate around the presented value due to the influence

of a varying temperature field on the absorption coefficient. Reynolds number, Prandtl number and T_0^+ are constant throughout the simulations with values of 2900, 1 and 1.5, respectively. The DNS results presented in the following sections consist of averaging of 120 statistically independent fields for each simulation.

TABLE 3.1: Investigated cases

CASE	Ref	G01	G1	G10	L01	L1	L10	H01	H1	H10
Pl	-	0.03	0.03	0.03	0.3	0.3	0.3	0.03	0.03	0.03
τ	0	0.1	1.0	10	0.1	1.0	10	0.1	1.0	10
κ	0	0.1	1.0	10	$f(T)$	$f(T)$	$f(T)$	$f(T)$	$f(T)$	$f(T)$

Chapter 4

Results and Discussion

4.1 Grey Gas

The effect of various optical thicknesses on TRI in a grey participating fluid flow is studied first. These cases are G01, G1 and G10, which are characterized with a low Planck number to ensure high impact of radiation on heat transfer (see table 3.1).

4.1.1 Mean flow properties

Figures 4.1(a), 4.1(d), 4.1(c) and 4.1(b) show the average profiles of non dimensional temperature $\overline{\theta}$, emissive power normalized by the absorption coefficient $\overline{E}_m = 4\overline{\left(\theta/T_0^+ + 1\right)^4}$, incident radiation $\overline{G}$ and net radiative volumetric heat source $\overline{P}_r$, respectively (the inlay in figure 4.1(d) shows a zoom on the y-axis). Note that $\kappa\overline{G}$ denotes a heat source in the energy equation, while $\kappa\overline{E}_m$ is the heat sink due to emission.

Radiative heat transfer shows a strong influence on temperature profiles in all three cases. It is important to point out that boundary emission remains constant since the temperature at the boundary is fixed and $\epsilon_w = 1$ (see figure 4.1(b)). For a low optical thickness (case G01, with $\tau = 0.1$), the addition of radiative heat transfer causes the bulk temperature to increase and temperature profile to flatten in the core of the channel. This result can be explained by considering the long range of radiative heat transfer that causes a fairly homogeneous distribution of the heat source ($\kappa\overline{G}$) throughout the channel. By analyzing the incident radiation profile (figure 4.1(c)), it is possible to notice that $\overline{G}$ exhibits only a slight decrease when moving from the hot to the cold side of the channel. As a consequence, the temperature gradient increases at the cold side where more energy ($G - E_m$) is available, while it reduces at the hot side, as well as in the core of the channel, due to the increased bulk temperature. Upon increasing the optical thickness (case G1), the length scales of radiative heat transfer reduce due to the larger

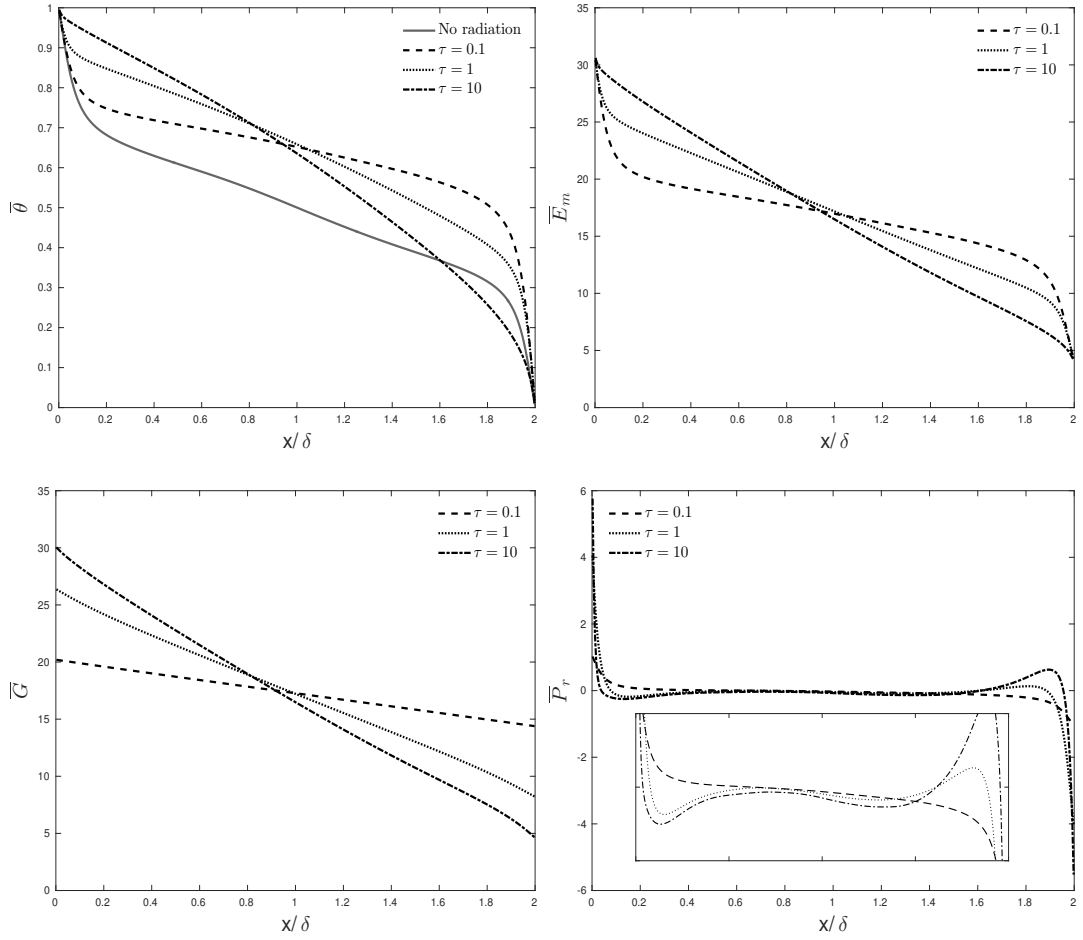

FIGURE 4.1: Averaged profiles. (a): mean temperature; (b): mean emissive power; (c): mean incident radiation; (d): mean radiative heat source (the inlay shows a zoom on the y-axis around $\overline{P}_r = 0$).

absorption (i.e. thermal radiative beams attenuate at a faster rate), shifting $\kappa\overline{G}$ towards the hot side of the channel. This shift can be seen in figure 4.1(c) as the profile of incident radiation profile steepens. Therefore, an intermediate optical thickness results in an overall increase of temperature gradient in the channel core, while the gradients near the walls are smoothened out. A further increase of the optical thickness (case G10) causes an almost complete suppression of the convective and the conductive effects. The temperature gradient decrease drastically near the walls following the further steepening of incident radiation slope, causing an almost linear temperature profile for G10. $\overline{P}_r$ represents the combined effect of emission sink ($\kappa\overline{E_m}$) and absorption source ($\kappa\overline{G}$) of energy. For G01 $\overline{P}_r$ undergoes a monotonic transition from positive to negative values, resulting in a sink of energy on the hot side and a source on the cold side. Upon increasing optical thickness, local minima and maxima appear respectively close to the hot and cold wall due to the contraction of radiative heat transfer length scales. In other words, a local region near the hot wall appears where, due to incoming radiation from the boundary, absorption levels are higher than emission. Vice versa occurs near the

cold wall where the sink of energy due to emission is not replenished by incident radiation. This effect results in local source/sink of energy near the walls and a subsequent reduction in temperature gradient.

4.1.2 Heat flux

Heat fluxes are derived from the averaged energy equation, rewritten here for clarity:

$$\frac{\partial}{\partial x}\left(\frac{1}{RePr}\frac{\partial\overline{\theta}}{\partial x}-\overline{u'\theta'}\right)-\frac{\overline{P}_r}{RePrPl}=0\ . \tag{4.1}$$

Integrating equation (4.1) in wall normal direction (x) yields:

$$\frac{1}{RePr}\frac{\partial\overline{\theta}}{\partial x}-\overline{u'\theta'}-\int_0^x\frac{\overline{P}_r}{RePrPl}dx=C_1\ , \tag{4.2}$$

where C_1 is an integration constant, which is equal to the difference of the total wall heat flux and radiative heat flux on the hot wall $C_1=\overline{q}_w-\overline{q}_{R,hw}$. The flow is statistically homogeneous in the spanwise and streamwise direction, it follows that:

$$\frac{\partial\overline{q}_y}{\partial y}=\frac{\partial\overline{q}_z}{\partial z}=0\ . \tag{4.3}$$

This allows to state that:

$$\int_0^x\overline{P}_r dx=\overline{q}_x+C_2\ , \tag{4.4}$$

where $C_2=\overline{q}_{R,hw}$. The three terms on the LHS of equation (4.2) represent the three heat transfer modes defined as:

$$\overline{q}_{cd}=-\frac{1}{RePr}\frac{\partial\overline{\theta}}{\partial x},\quad \overline{q}_{turb}=\overline{u'\theta'},\quad \overline{q}_R=-\frac{\overline{q}_x}{RePrPl}. \tag{4.5}$$

The long range of the radiative heat transfer requires the consideration of three main contributions in the analysis of the radiative heat flux:

- Wall to wall contributions; $\overline{q}_{R,ww}$ defines the heat flux that is transferred directly from the hot to the cold wall, unobstructed by the presence of a participating media. The temperature of the flow is unaffected by these heat flux contributions.
- Fluid to wall contributions; $\overline{q}_{R,fw}$ include both the heat flux that, emanating from the hot wall, is absorbed by the flow, and the heat flux generated by emission from the flow that reaches the cold wall. These contributions are the main cause of the change in temperature profile observed in figure 4.1(a)
- Fluid to fluid contributions; $\overline{q}_{R,ff}$ refer to the heat flux originating within the fluid due to emission, and reabsorbed before reaching the cold wall. These contributions

do not result in an increase of bulk temperature, but are responsible in shaping the temperature profile.

Figure 4.2(a) shows the overall heat transfer in the channel $\overline{q}_{turb} + \overline{q}_c + \overline{q}_R$, while figures 4.2(b) to 4.2(d) display the heat fluxes for case G01,G1,G10. Radiative heat flux is non dimensionalized by the wall radiative flux on the hot side $\overline{q}_{R,hw}$

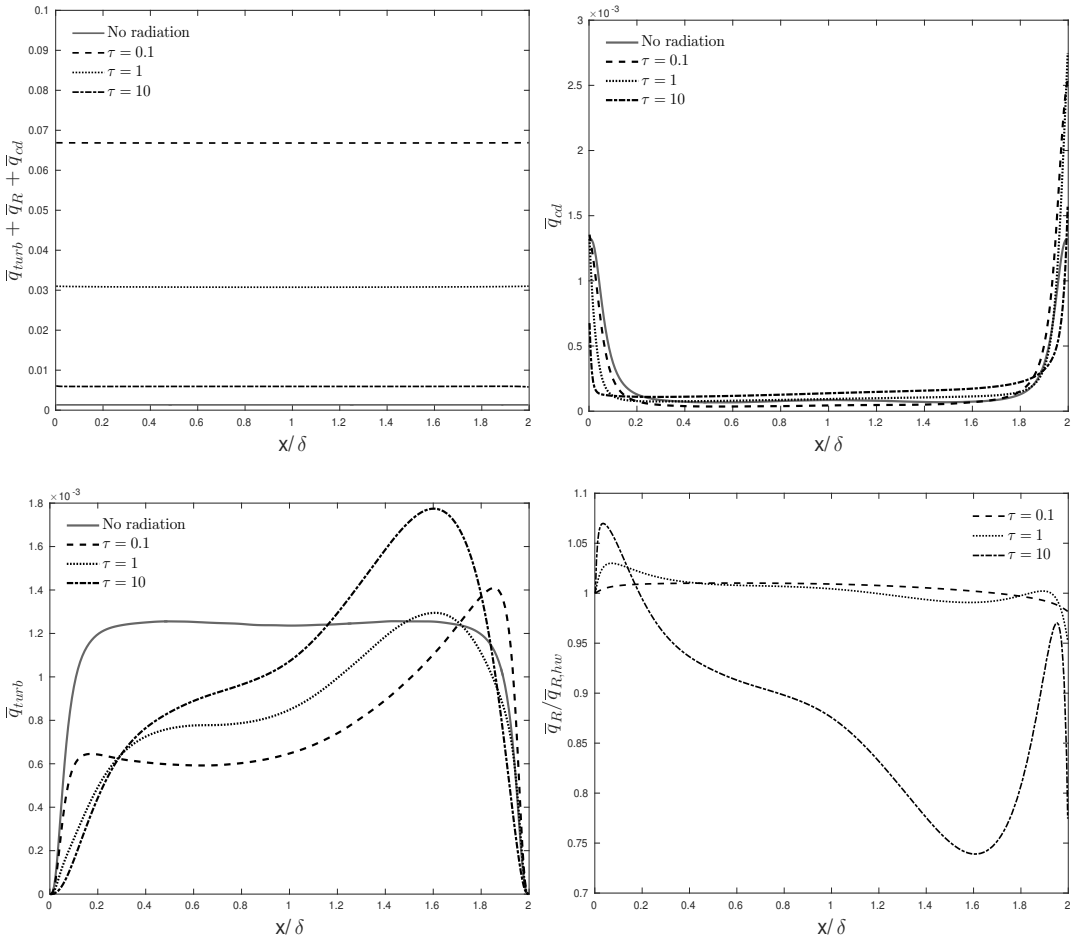

FIGURE 4.2: heat transfer mechanisms. (a): total heat flux; (b): mean conductive heat flux; (c): mean wall normal turbulent heat flux; (d): mean radiative heat flux normalized on wall radiative flux on hot side

By inspecting figure 4.2(a) a drastic increase of overall heat flux between the non radiating and the radiating cases is noticeable. Moreover heat flux tends to reduce when the optical thickness is increased.

Comparing the magnitudes between the different contribution it is also clear that radiative heat transfer dominates over other heat transfer mechanisms. Although the radiative heat flux diminishes for higher optical thicknesses, the radiative flux contribution to the overall heat transfer to the fluid is increased. A distinction must be made

between wall to wall, fluid to wall and fluid to fluid radiative heat flux. Unfortunately, the correct magnitude of these three contributions cannot be explained by inspecting of the total $\overline{q}_R$, but a qualitative explanation can be inferred by considering radiative heat transfer length scales. For a low optical thickness, the thermal radiative waves can travel relatively undisturbed from the hot to the cold wall. Therefore wall to wall contributions comprise of the largest share of $\overline{q}_R$. The consequence is a high heat transfer between hot and cold wall, but a small share of energy that is effectively absorbed by the fluid. The $\overline{\theta}$ profile is thus mainly the result of turbulent and conductive heat transfer. When the optical thickness increases, the radiative heat flux diminishes but $\overline{q}_R$ is mainly a result of fluid to wall and fluid to fluid contributions. In other words, a higher share of heat flux traveling from hot to cold side is absorbed and redistributed within the media. Thus the influence of radiative heat transfer in bulk temperature and temperature profile is increased.

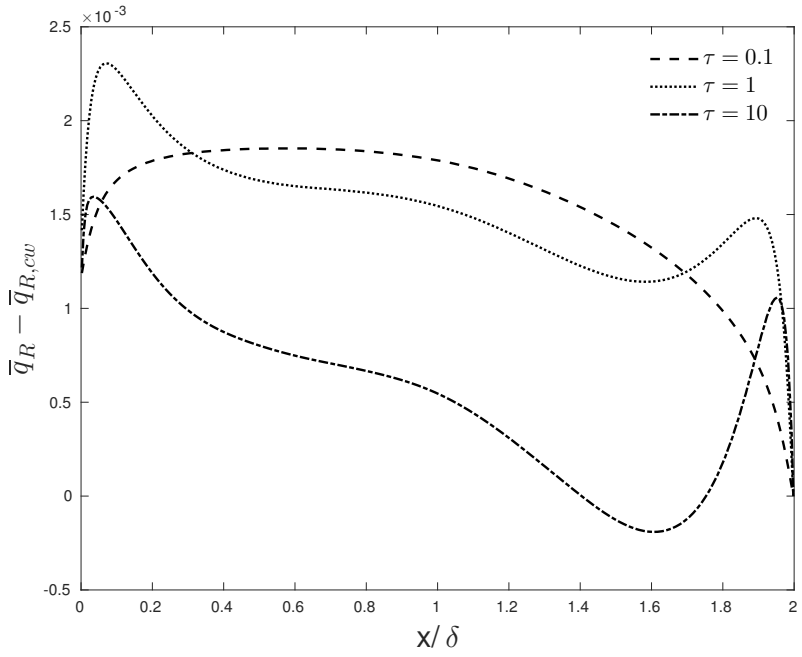

FIGURE 4.3: radiative heat flux $\overline{q}_R$

Figure 4.3 shows plots of the radiative heat flux $\overline{q}_R$ minus the radiative wall flux on the cold side. In a situation in which $T_{w,c} = T_{w,h}$ it would hold that $\overline{q}_{R,hw} - \overline{q}_{R,cw} = 0$ since wall to wall contributions would not participate in radiative heat transfer. The increase of $\overline{q}_R$ near the hot wall is due to the effect of emission augmentation, while moving towards the cold boundary energy is absorbed resulting in a reduction of $\overline{q}_R$. The presence for $\tau = 10$ of a region where $\overline{q}_R < \overline{q}_{R,wc}$ displays the effect of strong fluid to fluid contributions, confirming the absorption of intensity emitted from the hot boundary, and therefore a lack of wall to wall contributions.

Conductive heat flux, shown in figure 4.2(b), is aligned with the temperature gradient,

and thus presents the features explained while analyzing temperature profiles. Therefore the modification of conductive heat flux can be inferred from the analysis of figure 4.1(a).

Figure 4.2(c) presents profiles of turbulent heat flux. If no radiative heat transfer occurs (case Ref) turbulent heat flux is constant in the channel core. Furthermore $\overline{q}_{turb}$ decreases till zero near the walls where conductive heat flux is predominant due to the no slip condition. The symmetry of $\overline{u'\theta'}$ is lost in radiative cases where a peak originates on the cold side. For a low optical thickness ($\tau = 0.1$) turbulent heat flux is suppressed near the hot wall as well as in the rest of the channel due to the decrease in temperature gradient and a lower fluctuating thermal field (see next section). The profile shows a local maximum near the hot side, owing to the intense turbulence levels near the walls. By increasing the optical thickness to $\tau = 1$ (case G1) the peak on the cold side is reduced and shifted towards the outer layer and same occurs on the hot side where the reduction of turbulent heat flux affects a larger area. The local maximum disappears, leaving space to a monotonic transition from the walls to the peak location. In the core of the channel turbulent heat transfer is enhanced by the increase of optical thickness. For a high optical thickness case (G10), turbulent heat flux is strongly intensified on the cold side, where a further shift of the peak towards the center is observed.

4.1.3 Temperature variance and fluctuations of radiative quantities

In this section temperature variance will be examined to understand the modification of temperature fluctuation in presence of a radiating field.

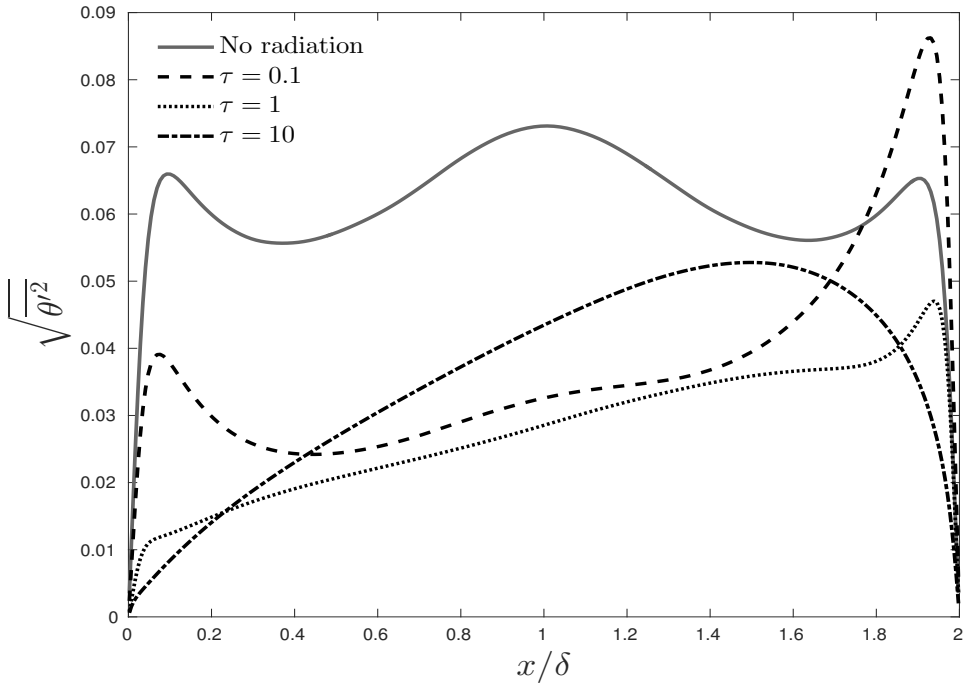

FIGURE 4.4: Turbulent intensity of temperature fluctuation

The temperature variance for the grey gas cases with different optical thicknesses is shown in figure 4.4. For a non radiating case, temperature root mean square profile is symmetric showing local peaks near the walls and a maximum in the center of the channel. In the boundary layer, as already noticed by Kim et Al [27], temperature fluctuations are highly correlated to streamwise velocity fluctuations, exhibiting the same turbulent structures. The local maximum located in the channel core is generated by pockets of cold and hot fluid transported from the boundaries towards the center.

The temperature variance can be analyzed in detail by means of the evolution equation for temperature fluctuations:

$$\frac{\partial \theta'}{\partial t} + \frac{\partial \overline{u_j}\theta'}{\partial x_j} + \frac{\partial u_j' \overline{\theta}}{\partial x_j} + \frac{\partial u_j'\theta'}{\partial x_j} - \frac{\partial \overline{u_j'\theta'}}{\partial x_j} = \frac{1}{RePr}\frac{\partial^2 \theta'}{\partial x_j^2} - \kappa \frac{E_m'}{RePrPl} + \kappa \frac{G'}{RePrPl} \ . \quad (4.6)$$

G' is a source of energy fluctuation, while E_m' acts as a sink. Note that E_m' is always positively correlated to θ', since:

$$E_m' = 4\left(\frac{\theta}{T_0^+} + 1\right)^{4'} , \quad (4.7)$$

As a matter of fact, E'_m stabilizes temperature levels in the channel; as a positive θ fluctuation occurs a positive E_m fluctuation follows, increasing emission and subsequently reducing temperature. Vice versa when a negative θ' is observed less emission is experienced, consequently rising temperature to the previous value. On the other hand G' counteracts the sink effect produced by E'_m and where fluctuations of G are high, the stabilizing effect of emission is weaker, allowing for higher θ' values.

The peak locations are retained for a low optical thickness radiative case (G01, $\tau = 0.1$). The Radiative power fluctuations act as a sink term since they are dominated by the emission fluctuations E'_m, resulting in a mitigation of the fluctuation peak near the hot wall. Indeed G' (figure 4.5) show a negligible contribution to equation 4.6. On the other hand, the high temperature gradient occurring on the cold side increases the thermal turbulence near the cold wall beyond case Ref. This rise in fluctuation levels is not a direct effect of radiation term, rather an effect of the increased production due to higher temperature gradients (see temperature variance budgets section 4.1.4). In the core of the channel the effect of fluctuating energy pockets is reduced, since thermal structures directed towards the core absorb/emit radiation, with a significant aid from fluid to wall heat flux contributions, stabilizing the temperature before the center is reached. In other words, the lower temperature gradient in the core results in a lower fluctuation level.

When the optical thickness increases, fluctuation levels are largely reduced both on the hot and cold side due to the direct action of radiative emission, which provides means of stabilization to temperature fluctuations. Transport of cold and hot pockets of temperature towards the center of the channel is nullified by the strong action of radiative heat transfer that balances temperature levels before the center is reached. A new peak starts to appear close to $x/\delta = 1.5$. This local maximum is not determined by the action of turbulent transport, rather than the action of incident radiation fluctuations that start to balance the sink produced by E'_m (see section 4.1.4). Nonetheless the overall tendency is to further reduce thermal turbulence intensity by redistributing temperature through emission.

Interestingly, increasing the optical thickness to $\tau = 10$ produces a higher level of thermal fluctuations. The peak at $x/\delta \sim 1.5$ already present in case G1 grows for $\tau = 10$ causing temperature fluctuations in the channel core to be larger when compared to cases G1 and G01. Near-wall fluctuations on the hot side are largely reduced, while near the cold wall no peak as the previous cases can be noticed. The modification of thermal turbulent structures is presumably caused by incident radiation fluctuations that reach a magnitude comparable to emission fluctuations. In figure 4.5 it is possible to notice the drastic increase in incident radiation fluctuations upon increasing the optical thickness. This rise is caused by the reduction of radiation length scales discussed in section 2.4;

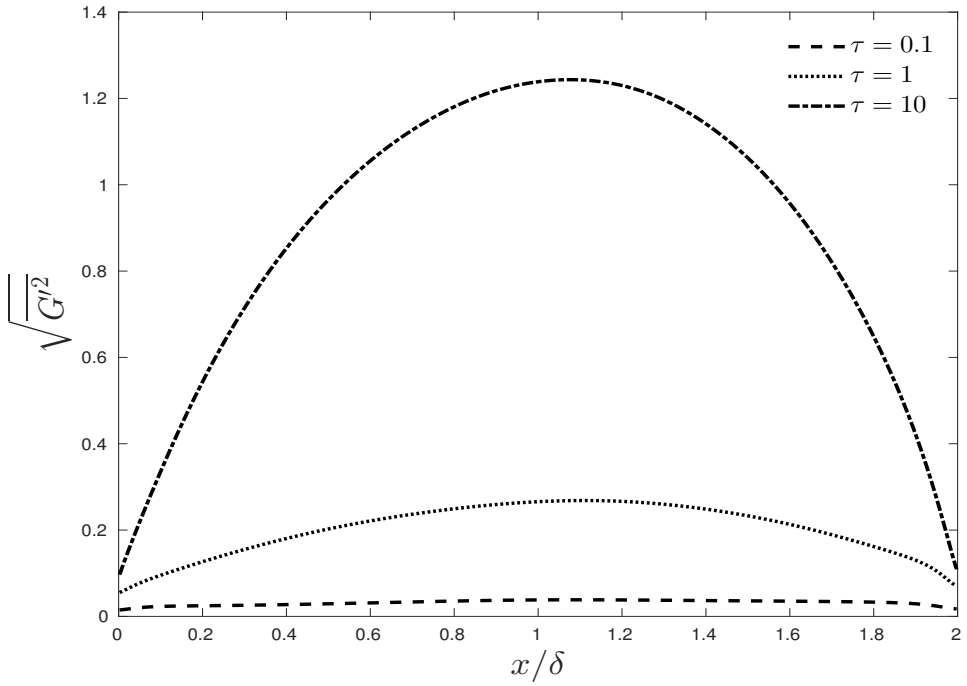

FIGURE 4.5: incident radiation root mean square profiles

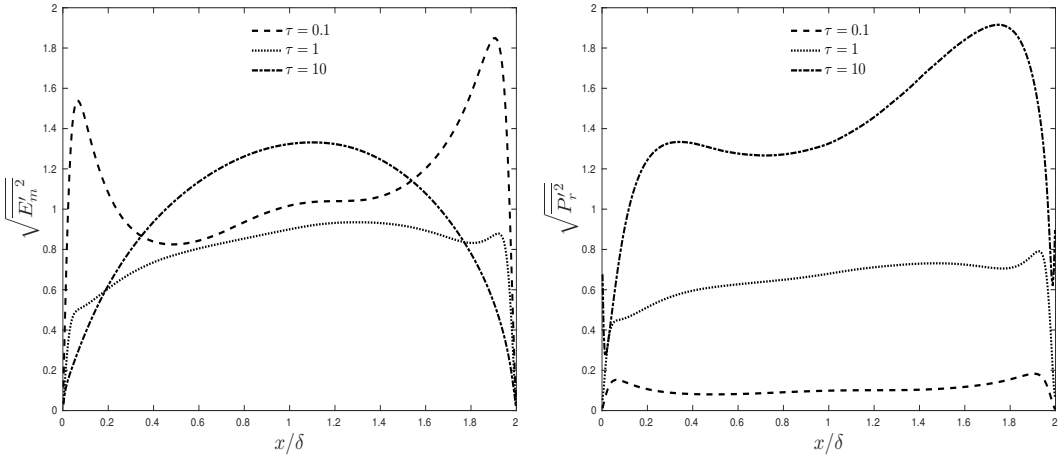

FIGURE 4.6: (a): E_m root mean square profiles; (b): P_r root mean square profiles

incident radiation at a high optical thickness can be regarded mostly as a short range phenomenon, hence being heavily influenced by local temperature fluctuations. Interestingly the peak of incident radiation fluctuations is always located near the center of the channel. Radiation as a matter of fact is not transported by the flow, to which it is indirectly coupled by means of temperature. For this reason incident radiation experiences a heavy reduction in fluctuations near the boundaries where a fixed temperature is provided, while undergoing larger fluctuations in the center where the mitigating effect of the boundaries is not felt. Recalling the theory investigated in section 2.4, incident radiation is mostly influenced by large temperature scales, while small eddies mostly behave as an optically thin media. For this reason G fluctuations are mostly concentrated

near the channel center where temperature fluctuations are usually associated with large scales of motion, while decreasing towards the walls where the presence of vortices characterized by higher frequencies can be observed. Profiles of $\sqrt{\overline{G'^2}}$ will drastically change if iso-flux or adiabatic boundaries would be applied, modifying temperature rms profiles. The peak observed in $\overline{\theta'^2}$ profile for case G10, does not match with the location of $\overline{G'^2}$ maximum, but is shifted towards the cold wall, because of the lower level of Emission fluctuations located on the cold side.

4.1.4 Budgets of temperature variance

The budget equation for the temperature variance is discussed next to highlight the effects of different phenomena on temperature fluctuations. Transport equation for temperature variance, as derived in appendix B for fully developed channel flow, reads:

$$0 = -2\overline{u'\theta'}\frac{\partial\overline{\theta}}{\partial x} + \frac{\partial}{\partial x}\left(\frac{1}{RePr}\frac{\partial\overline{\theta'^2}}{\partial x} - \overline{u'\theta'^2}\right) - \frac{2}{RePr}\overline{\left(\frac{\partial\theta'}{\partial x_j}\right)^2} - \frac{2}{RePrPl}\overline{P_r'\theta'} \ . \tag{4.8}$$

Individual description of the terms is written below:

- Turbulent production $\mathcal{P}_\theta = -2\overline{u'\theta'}\frac{\partial\overline{\theta}}{\partial x}$
- Turbulent transport $\mathcal{T}_\theta = -\frac{\partial\overline{u'\theta'^2}}{\partial x}$
- Molecular diffusion $\phi_m = \frac{1}{RePr}\frac{\partial^2\overline{\theta'^2}}{\partial x^2}$
- Molecular dissipation $\epsilon_m = -\frac{2}{RePr}\overline{\left(\frac{\partial\theta'}{\partial x_j}\right)^2}$
- Radiation term $\mathcal{R} = -\frac{2}{RePrPl}\overline{P_r'\theta'}$

The radiation term $\mathcal{R}$, in analogy with the molecular terms (ϕ_m, ϵ_m), can be decomposed into a diffusion ϕ_r and a dissipation term ϵ_r as follows:

$$\overline{P_r'\theta'} = \overline{\frac{\partial q_j'}{\partial x_j}\theta'} \ , \tag{4.9}$$

where:

$$\overline{\frac{\partial q_j'}{\partial x_j}\theta'} = \frac{\partial\overline{q_x'\theta'}}{\partial x} - \overline{\frac{\partial\theta'}{\partial x_j}q_j'} \ . \tag{4.10}$$

Therefore, the decomposition yields:

$$\mathcal{R} = \phi_r + \epsilon_r \ , \tag{4.11}$$

where:

$$\phi_r = -\frac{2}{RePrPl}\frac{\partial\overline{q_x'\theta'}}{\partial x} \ , \tag{4.12}$$

and

$$\epsilon_r = \frac{2}{RePrPl}\overline{\frac{\partial\theta'}{\partial x_j}q_j'} \ , \tag{4.13}$$

Figure 4.7 reports the budgets of temperature variance for a non radiating turbulent channel flow. The profiles are symmetric due to the symmetry of temperature profile. Adjacent to the walls, due to the non slip condition, molecular effects dominate, with molecular diffusion balancing molecular dissipation. Near the walls turbulent production shows a peak. High temperature gradients in the near wall region ensure a high

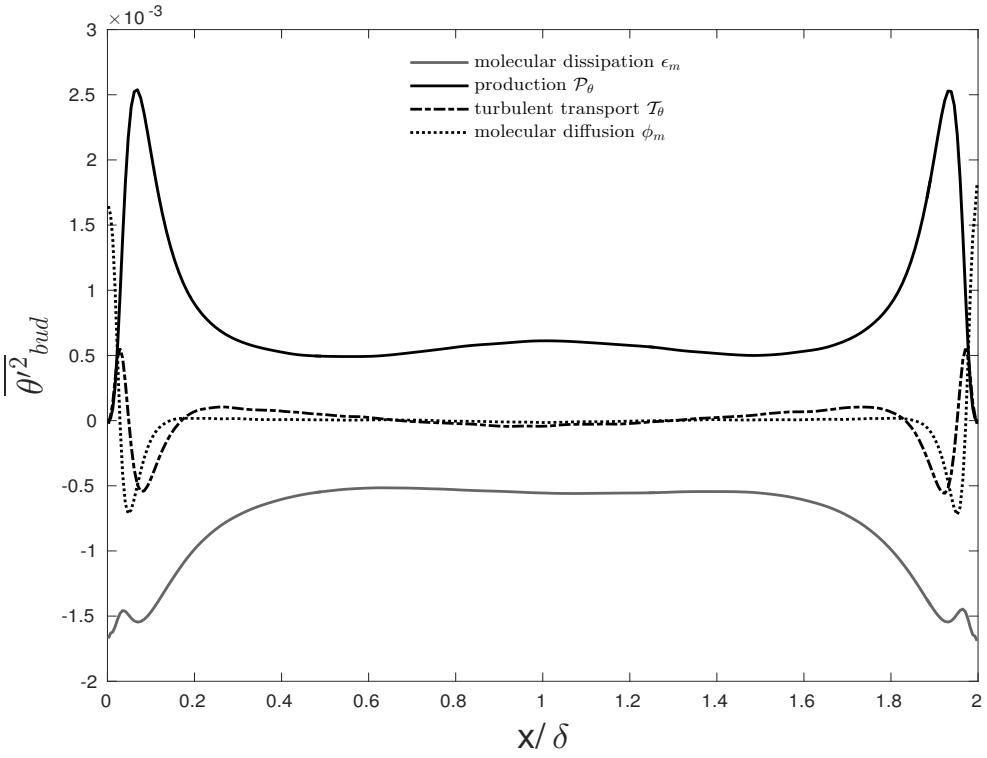

FIGURE 4.7: Budgets of temperature variance for Reference case (Ref)

production rate of temperature variance. The temperature fluctuations are subsequently redistributed towards the wall and towards the center of the channel by the action of turbulent transport ($\mathcal{T}_\theta$). In the center of the channel a direct balance of production and molecular dissipation can be observed.

Figure 4.8 presents the budgets of temperature variance for a low optical thickness radiative channel flow (case G01). Contrary to profiles in figure 4.7, budgets of temperature variance for a radiative flow are non-symmetrical. A noticeable rise in production can be observed on the cold side, due to the increase in temperature gradient. In order to balance the larger production rate, molecular dissipation, molecular diffusion and turbulent transport increase when compared to a non radiating case. The opposite effect is observed on the hot side where an overall reduction in magnitude of budgets is experienced. Radiation terms ($\mathcal{R}$, ϕ_r and ϵ_r) show a negligible contribution near the boundaries. In the core of the channel the production is weakened due to the reduction of the temperature gradient, causing a subsequent shrink in molecular dissipation. A direct effect of radiation can be noticed in the core of the channel where radiative dissipation ϕ_r starts to aid molecular dissipation in balancing production.

In figure 4.9 budgets of temperature variance for an intermediate optical thickness case are shown (case G1). On the hot wall budgets reduce drastically when compared to cases G01 and Ref, due to the reduced production, effect of a limited temperature gradient and a lower wall normal turbulent heat flux (figure 4.2(c)). This reduction causes

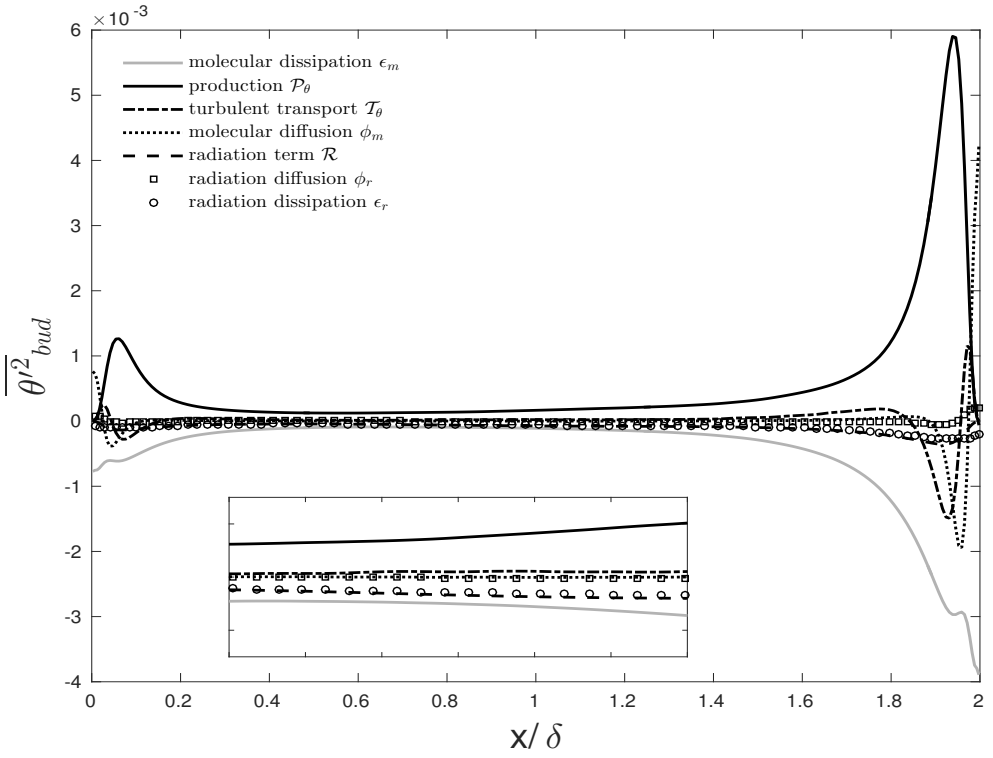

FIGURE 4.8: Budgets of temperature variance for case G01 $\tau = 0.1$, inclusion highlights the core zone ($x/\delta = 0.6 - 1.2$)

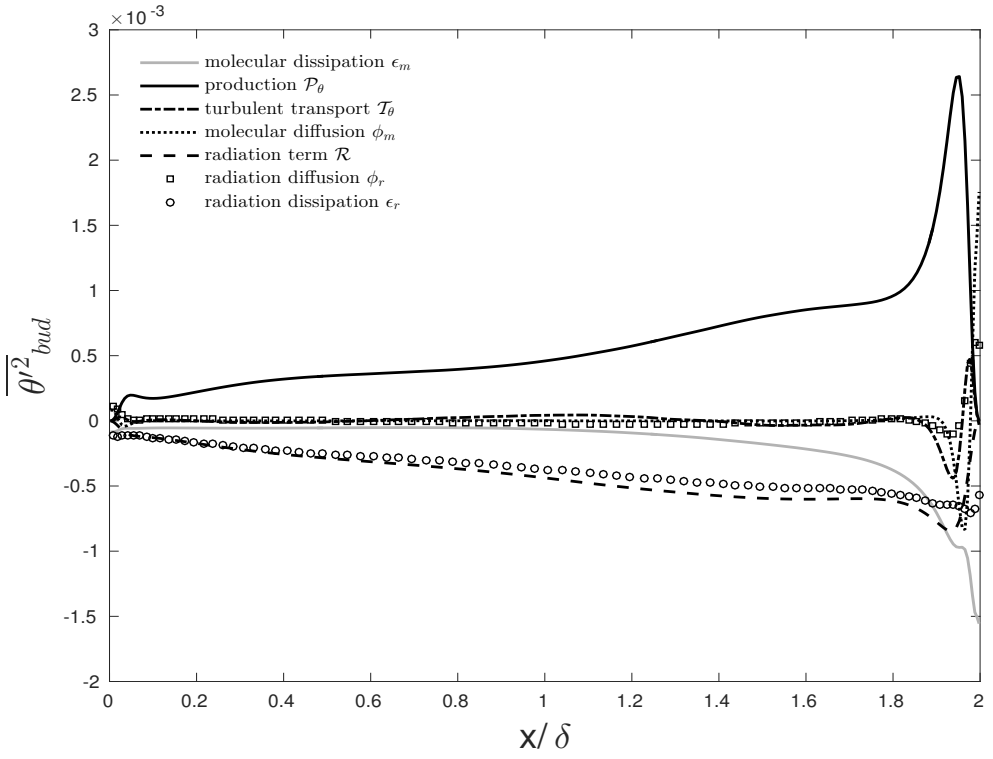

FIGURE 4.9: Budgets of temperature variance for case G1 $\tau = 1$.

all budgets near the hot wall to diminish. On the cold side the same effect is observed when compared to G01, with an overall reduction in budgets of temperature variance. Contrarily in the channel core production rate increases. The increase of production, caused by the rise in temperature gradient, is balanced by the strong growth of radiation dissipation that acts as a counterpart to turbulent production. Molecular diffusion and dissipation experience a further reduction, showing relevance only on the cold side. A small peak in turbulent transport starts to appear in the channel core, followed by a local minimum located around $x/\delta = 1.6$. The budgets analysis suggests a shift of fluctuation levels towards the center of the channel, due to the action of a more fluctuating radiation field. Relevance of molecular terms (ϕ_m and ϵ_m) reduces in favor of the radiative counterparts (ϕ_r and ϵ_r).

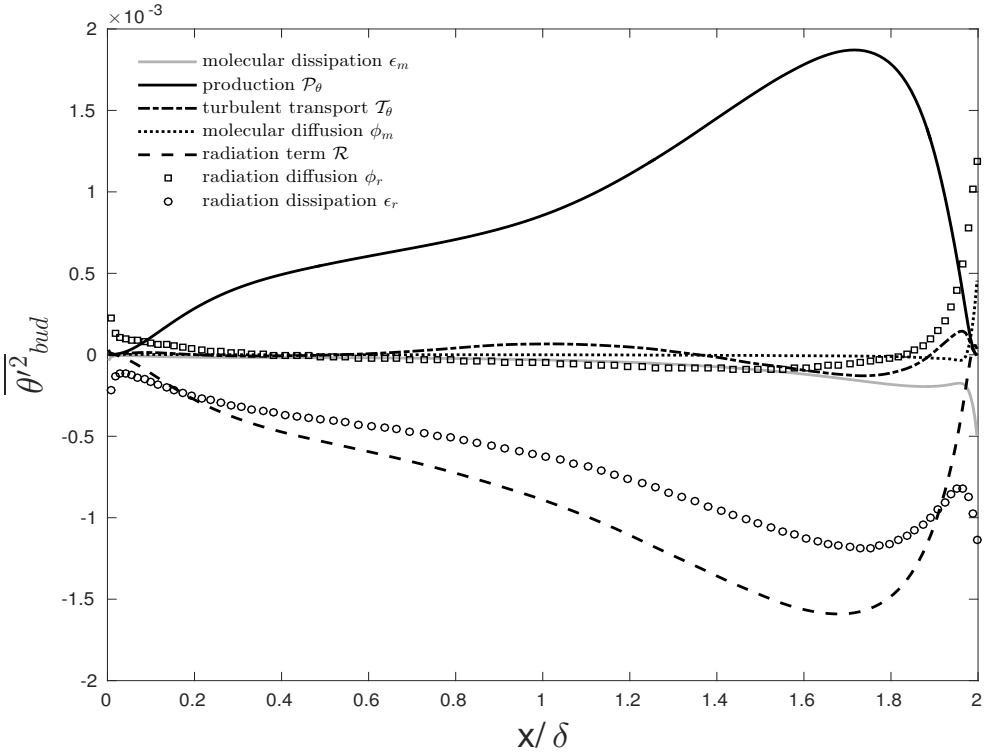

FIGURE 4.10: Budgets of temperature variance for case G10 $\tau = 10$

By further increasing the optical thickness, an enhancement of effects already noticed for case G1 occurs. In the whole core of the channel an overall increase in budget's magnitude is noticed. The molecular terms fall off, confirming the complete dominance of radiative terms, and on the hot side production is minimized due to smoothening of mean temperature gradient. All the budgets near the hot wall reduce significantly, while the radiative terms ϕ_r and ϵ_r increase and balance each other. This is the analogous of the near wall effects in a non radiating case, with radiative terms substituting molecular terms. In other words, temperature fluctuations are transported towards the hot wall by means of radiative diffusion and subsequently dissipated by the action of ϵ_r. Indeed,

by reducing the radiation length scales, radiative terms reduce to local quantities acting akin to molecular terms. The production is located further away from the wall, following the observation made in section 4.1.3. Turbulent transport grows in the core of the channel in order to redistribute fluctuations produced in the new peak location ($x/\delta = 1.7$). The decomposition of radiative term does not seem to work properly for $\tau = 10$ since $\epsilon_r + \phi_r \neq \mathcal{R}$ (figure 4.10). Following the considerations of chapter 2 it is possible to conclude that the low order of the scheme prevents a high accuracy in the intensity solution for a high optical thickness. Budgets obtained with CLAM scheme for $\tau = 10$ are shown in appendix B (figure B.1) and present a much higher accuracy. However the investigation of TRI with a more accurate solver is left for future work due to computational expenses.

The results suggest that with increasing the optical thickness the relevance of molecular terms is reduced in favour of the radiative terms. The radiative dissipation and diffusion take the place of the molecular dissipation and diffusion in redistributing and balancing the fluctuations produced by a mean temperature gradient that is enforced by radiative heat transfer (see figure 4.1). The evidence collected from the analysis of the temperature variance budgets seem to suggest that a further increase in the optical thickness would result in a further alignment of the production with $\overline{G'^2}$ peak (figure 4.5). Furthermore, the temperature fluctuations would recover and the radiative terms (ϕ_r and ϵ_r) would behave qualitatively similar to the molecular terms (ϕ_m and ϵ_m).

To highlight the effect of absorption and emission, the radiative term $\mathcal{R}$ can be decomposed as:

$$\mathcal{R} = \mathcal{R}_e + \mathcal{R}_a \ , \tag{4.14}$$

where

$$\mathcal{R}_e = -\frac{2\kappa}{RePrPl}\overline{E'_m\theta'}, \qquad \mathcal{R}_a = \frac{2\kappa}{RePrPl}\overline{G'\theta'}. \tag{4.15}$$

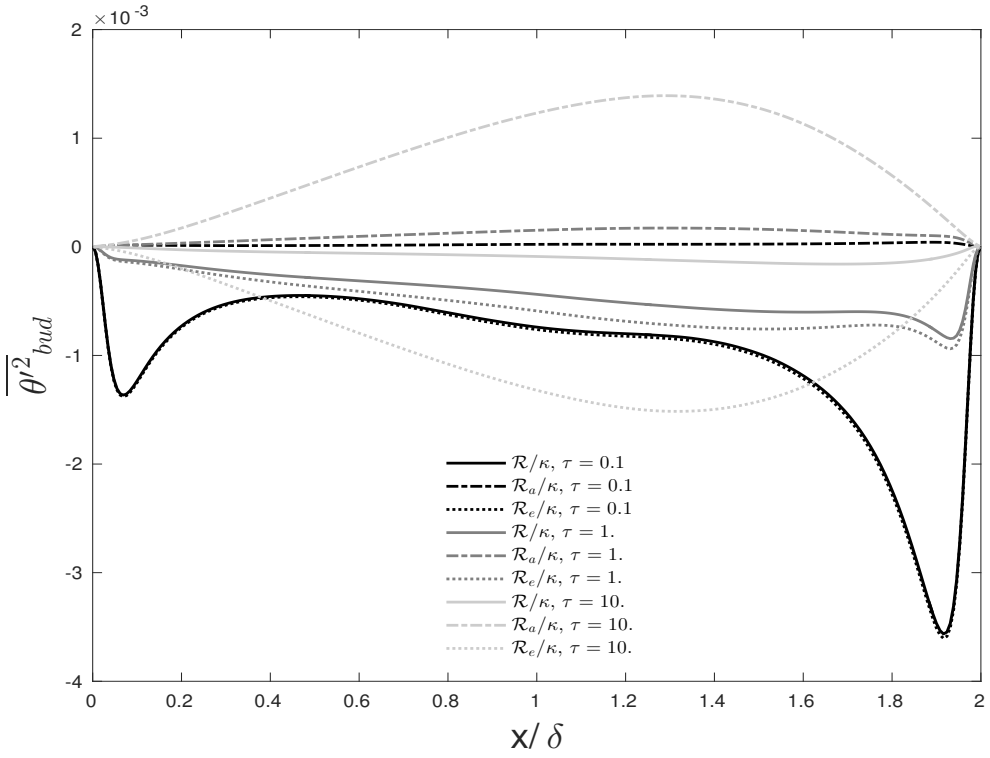

FIGURE 4.11: Radiation term $\mathcal{R}$ decomposed in absorption $\mathcal{R}_a$ and emission term $\mathcal{R}_e$ normalized by absorption coefficient κ for different optical thickness

Figure 4.11 shows the profiles foe $\mathcal{R}$, $\mathcal{R}_e$ and $\mathcal{R}_a$ normalized by the absorption coefficient. $\mathcal{R}_e$ is a sink, while $\mathcal{R}_a$ is a source of temperature fluctuations. As the optical thickness increases the effect of absorption term grows drastically. This confirms the hypothesis postulated in section 4.1.3, which states that G' is the cause of a modification of the thermal turbulence field, while emission fluctuation acts only as a sink for thermal fluctuations. It has to be noticed that the profiles in figure 4.11 are normalized by the absorption coefficient in order to clarify and compare the effects of different optical thicknesses, but $\mathcal{R}$,$\mathcal{R}_a$ and $\mathcal{R}_e$ increase drastically in magnitude upon increasing the optical thickness.

4.1.5 Temperature, velocity and incident radiation correlations

Since thermal turbulence is mostly influenced by velocity and incident radiation fluctuations, a particular attention must be paid to the correlation of these three quantities.

Plots of correlation coefficient for temperature - streamwise velocity (w) and temperature - incident radiation are shown in figures 4.12(a) and 4.12(b), respectively.

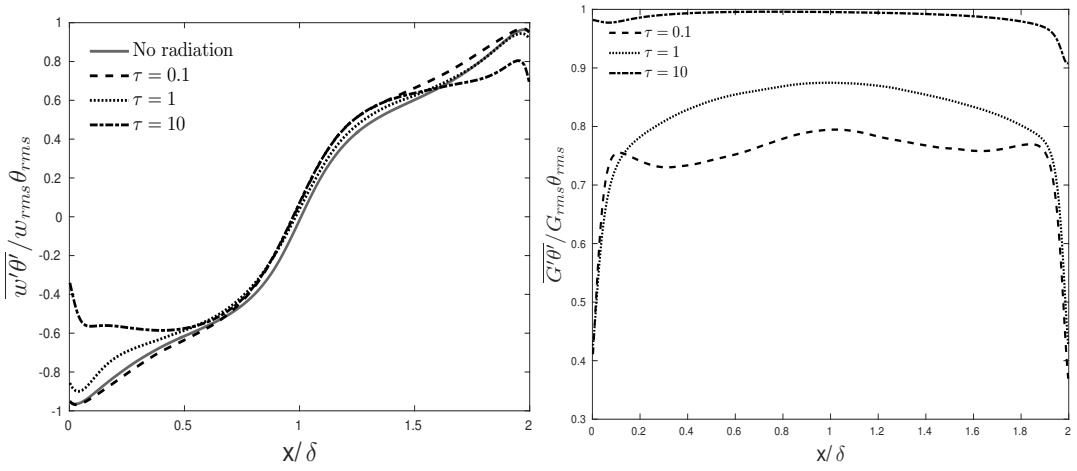

FIGURE 4.12: (a): streamwise velocity - temperature co-variance (streamwise turbulent heat flux); (b): incident radiation - temperature co-variance

The streamwise velocity and temperature fluctuation correlation is high near the walls. In the core of the channel, the correlation with streamwise velocity decreases since temperature fluctuations are mainly an effect of turbulent transport by wall normal velocity fluctuations. The correlation of $\overline{w'\theta'}$ for case G01 is similar to the non radiative case close to the walls. This proves that for a low optical thickness radiative heat transfer does not translate in a modification of thermal structures. As expected, upon increasing the optical thickness (cases G1 and G10), the temperature fluctuations start to decouple from streamwise velocity fluctuations as the correlation coefficient decreases. On the other hand, the correlation coefficient between G' and θ' (figure 4.12(b)) follows an opposite trend; upon increasing the optical thickness correlation coefficient between temperature and incident radiation rises ($\overline{G'\theta'}/G_{rms}\theta_{rms} \approx 1$ for $\tau = 10$). The lower value of $\overline{G'\theta'}/G_{rms}\theta_{rms}$ near the boundaries suggests the presence of fluid to wall contributions and smaller thermal scales (see section 4.1.6). It can be safely deduced that the shortening of the radiation length scale allows increased incident radiation fluctuations, reducing energy sink effects of radiative emissions.

Temperature autocorrelation

In this section temperature 2-point autocorrelation will be investigated. 2-point 1-time covariance for two turbulent quantities f_1 and f_2 is defined as:

$$R_{f_1,f_2}(x,r) = \overline{f_1'(x) f_2'(x+r)} \ , \tag{4.16}$$

For convenience, correlations are computed in Fourier space in the homogeneous directions and then transformed back to physical space using to the relation:

$$R_{f_1,f_2}(x,r) = \frac{1}{2\pi} \int_{-\infty}^{\infty} E_{f_1,f_2}(x,w_r) e^{+iw_r r} dw_r \tag{4.17}$$

where $E_{f_1,f_2} = \overline{\widehat{f_1'} \widehat{f_2'}^*}$ is the energy co-spectrum and w_r is the wavenumber in r direction. $R_{f_1,f_2}(x,r)$ can be longitudinal, where the separation vector r is chosen to be parallel to the direction of the mean velocity ($r = r_z$), or transverse, where separation vector r is chosen to be perpendicular to the direction of mean velocity ($r = r_y$). The correlation is normalized as follows to yield the 2-point cross correlation:

$$\rho_{f_1,f_2}(x,r) = \frac{R_{f_1,f_2}(x,r)}{R_{f_1,f_2}(x,0)} \ . \tag{4.18}$$

Figure 4.13 illustrates longitudinal and transverse temperature 2-point autocorrelations at different channel heights; specifically in the location of velocity fluctuation peaks ($x/\delta = 0.076$ and $x/\delta = 1.93$) and the location of $\overline{\theta'^2}$ maximum for highly radiating case ($x/\delta \sim 1.5$).

By observing $\rho_{\theta,\theta}$ in figure 4.13 it is possible to notice that streamwise structures are not drastically modified by the radiative heat transfer. The same behaviour is recognizable for non radiative as well as radiative cases. A slight growth of the structures in the z direction appears for a large optical thickness case, where temperature autocorrelation highlights longer and more coherent structures. The enlargement of thermal structures suggests the need of using a larger box size in order to completely capture the features of large eddies. The same outcome can be concluded through the investigation of transverse 2-point temperature autocorrelation. In spanwise direction the effect of temperature structure modification is somewhat emphasized since the structures are relatively thin. A clear shift of the minimum in the positive r_y direction can be noticed in figures 4.13(a), 4.13(c) and 4.13(e) for case G10. This shift is a results of the presence of much larger and more coherent structures in the spanwise direction.

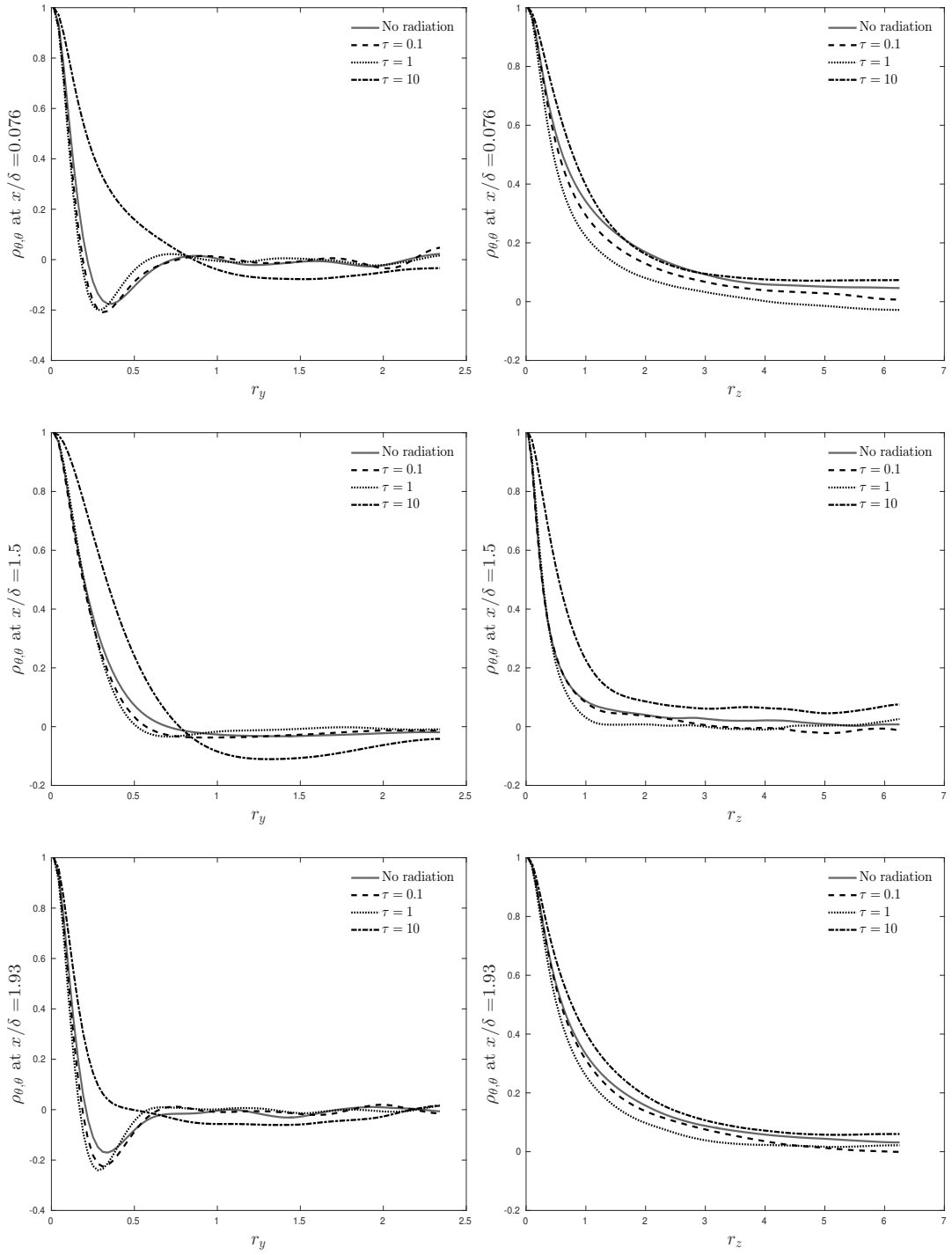

FIGURE 4.13: temperature longitudinal (a,c and e) and transverse (b,d and f) 2-point autocorrelation $\rho_{\theta,\theta}$ for different channel heights

4.1.6 Spectral analysis

Energy spectrum provides information on the energy of fluctuations contained at specific frequencies.
The region of interest is around $x/\delta = 1.5$, where temperature fluctuations peak for the optically thick case, and $x/\delta = 1.93$ where the large temperature gradient increases temperature fluctuations for G01 (see figure 4.4).

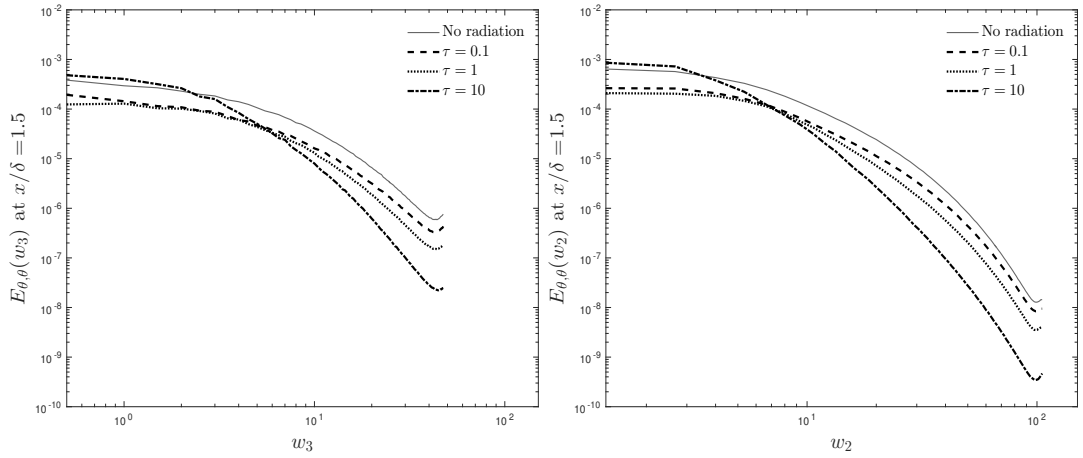

FIGURE 4.14: Temperature energy spectra $E_{\theta,\theta}$ at $x/\delta = 1.5$, (a): longitudinal energy spectra; (b): transverse energy spectra

The longitudinal temperature energy spectra for the location $x/\delta = 1.5$ are shown in figure 4.14(a), while figure 4.14(b) shows transverse temperature energy spectra. When comparing case G01 with the reference case, it is clearly noticeable that radiative effects are dominated by the emission. The Energy is reduced throughout the whole spectrum at a constant rate, proving that emission reduces fluctuations irrespective of the associated frequency. A further decrease in overall fluctuation intensity can be observed for $\tau = 1.$, with a larger energy reduction concentrated at large wavenumbers (i.e. within the small scales). The modification of the thermal energy spectra for $\tau = 1$ proves that the increase of $\overline{G'^2}$ affects mostly the large scales, while at small wavelength the stabilizing action of emission proceeds undisturbed. Upon increasing the optical thickness ($\tau = 10$) the energy contained in the large scales grows beyond the level of a non radiative case. The sink of fluctuation energy due to emission is further increased at high wavenumbers, due to the action of a higher absorption coefficient (see equation (2.45)), confirming the observation of optically thin behaviour of the small scales enounced in section 2.4. Therefore, upon increasing optical thickness the different behaviour observed for small and large eddies is amplified. In equation (2.45) emissive (constant 4) and absorptive ($\Re(\mathbf{w}, \kappa)$) terms scaling are multiplied by the absorption coefficient, which augments the effect of a different behaviour resulting in a completely different scaling of the energy spectrum.

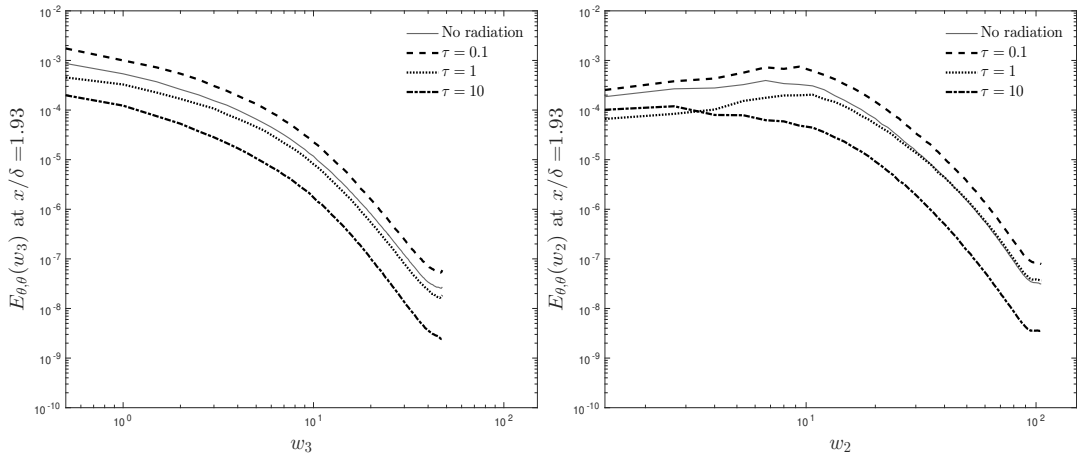

FIGURE 4.15: Temperature energy spectra $E_{\theta,\theta}$ at $x/\delta = 1.93$, (a): longitudinal energy spectra; (b): transverse energy spectra

Figure 4.15 depicts temperature energy spectra for cases Ref, G01, G1 and G10 at $x/\delta = 1.93$. In the streamwise direction (figure 4.15(a)) due to the low level of incident radiation fluctuations a constant energy sink rate throughout the whole spectrum is observed. For the case G01 instead, the higher production (located at intermediate wavelengths), combined with the effect of turbulent transport results in higher energy at all frequencies when compared to the non radiative case.
The same behaviour as for figure 4.15(a) is noticed for the large wavenumber range in the spanwise direction (figure 4.15), while for $\tau = 10$ in the low wavenumber region the phenomena of energy accumulation at large scales occurs.

Figures 4.16 and 4.17 show contours of transverse temperature spectra multiplied with the wavenumber and normalized by the local temperature variance. The y-axis shows the

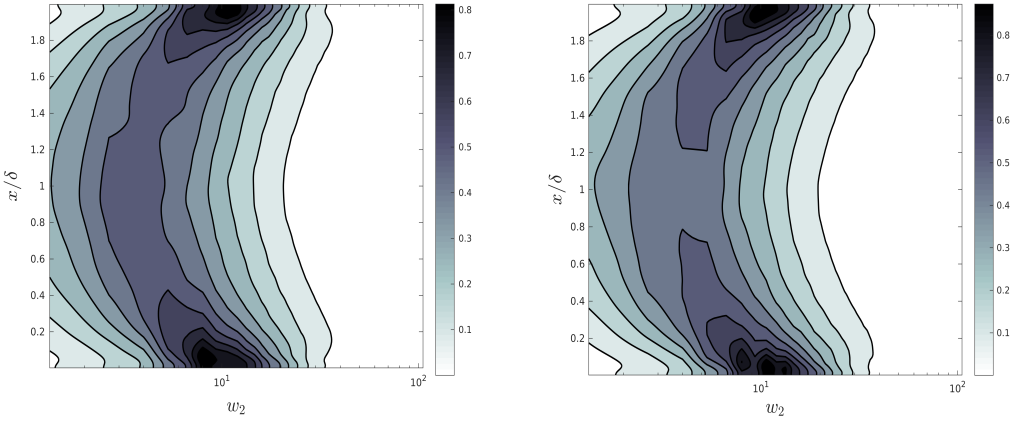

FIGURE 4.16: Pre-multiplied, normalized thermal energy spectra contours $w_2 E_{\theta,\theta}/\overline{\theta'\theta'}$; (a): no radiation case; (b) $\tau = 0.1$

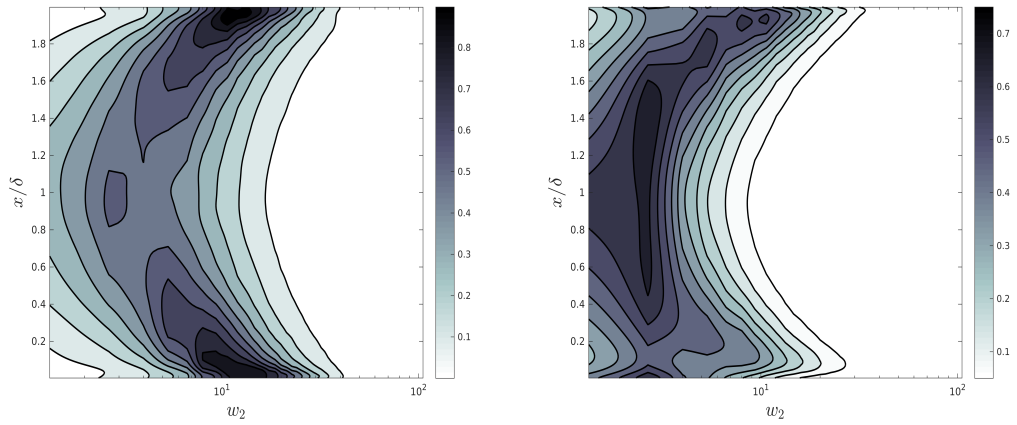

FIGURE 4.17: Pre-multiplied, normalized thermal energy spectra contours $w_2 E_{\theta,\theta}/\overline{\theta'\theta'}$; (a): $\tau = 1$; (b) $\tau = 10$

variation in the wall normal direction (x/δ), while the x-axis represents the wavenumber w_2. For a non radiative case the energy in the core of the channel is concentrated in relatively large eddy fluctuations, while close to the walls fluctuations are characterized by a larger frequency, denoting the presence of smaller thermal structures. The redistribution of energy changes when increasing optical thickness as the higher frequency fluctuations located near the wall transfer their energy to the large scales in the channel core.

The incident radiation spectra are analyzed as for the temperature spectra in order to identify the length scales of interest when dealing with radiative turbulent flows.
Figure 4.18 shows respectively the longitudinal and transverse G' energy spectra at $x/\delta = 1$, where $\overline{G'^2}$ shows a peak (see figure 4.5). Spectra are normalized by the optical thickness in order to improve the visibility and highlight the resulting slope.
A first observation can show that incident radiation fluctuations grow significantly over the whole spectra by increasing the optical thickness, confirming the validity of the conclusions drawn in section 2.4. Indeed the slope of $E_{G,G}$ steepens with an increase in τ, highlighting the preferential effect of incident radiation over the large scales when a high optical thickness is considered.

On the other hand, figure 4.19 shows $E_{G,G}$ normalized by the optical thickness close to the cold wall ($x/\delta = 1.93$). The slope increase observed in figure 4.18 is hardly noticeable, and only visible for the highest simulated optical thickness ($\tau = 10$). The energy increase throughout the spectra is also relatively low when compared to the growth observed at $x/\delta = 1$. Indeed the combination of these observations suggest that the influence of a thermal field fluctuating at higher frequencies, as for the near wall region, delays the recovery of temperature fluctuations due to the inhibition of $\overline{G'^2}$ growth (i.e. a lower rate increase of $E_{G,G}$ with τ).

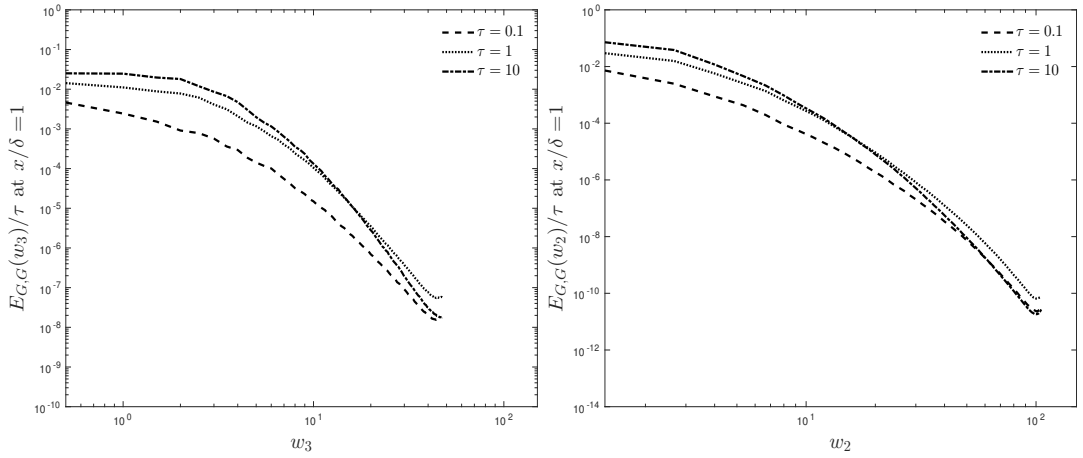

FIGURE 4.18: Incident radiation energy spectra $E_{G,G}$ normalized by optical thickness τ at $x/\delta = 1.$, (a): longitudinal energy spectra; (b): transverse energy spectra

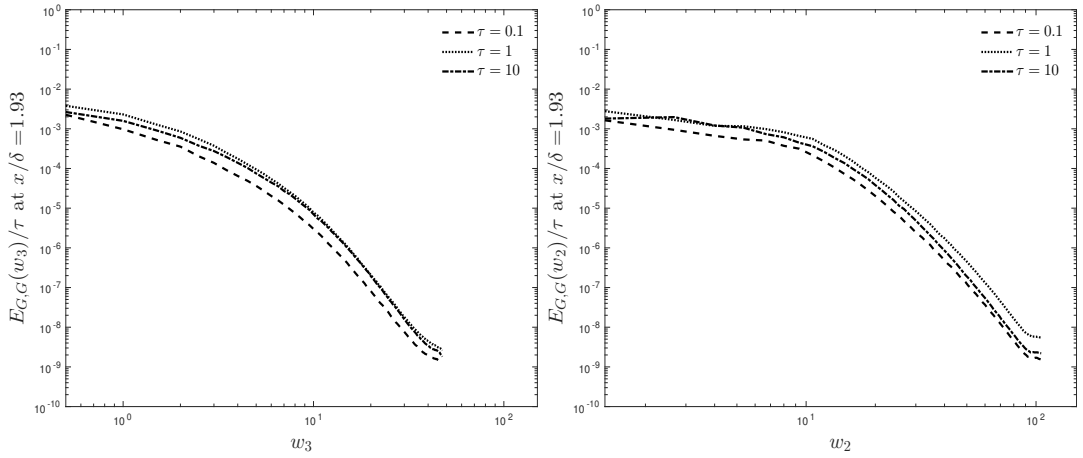

FIGURE 4.19: Incident radiation energy spectra $E_{G,G}$ normalized by optical thickness τ at $x/\delta = 1.93$, (a): longitudinal energy spectra; (b): transverse energy spectra

In order to verify the conclusions drawn in section 4.1.4, a comparison between the influence of molecular and radiative terms over the scales can be performed. The molecular dissipation in homogeneous isotropic turbulence scales with w^2, having a larger effect on smaller scales. The radiative influence over the scales can be analyzed by inspecting the term $N(w) = E_{P_r,\theta}/E_{\theta,\theta} \cdot 2/Pl$ defined as in Schertzer and Simonin [10]. The characteristic time scale of molecular dissipation can be defined as $t_m = (E_\epsilon/E_{\theta,\theta})^{-1}$, where E_ϵ is the molecular dissipation spectra, commonly referred in literature as $D_\theta(k)$. In analogy with t_m, the characteristic radiative time scale is represented by $t_R = N^{-1}(w)$. Note that radiation time scale contains information of radiation diffusion, while t_m concerns only molecular dissipation since molecular diffusion is absent in the core of the channel. Figure 4.20 shows plots of the aforementioned terms calculated in the transverse and longitudinal direction, respectively.

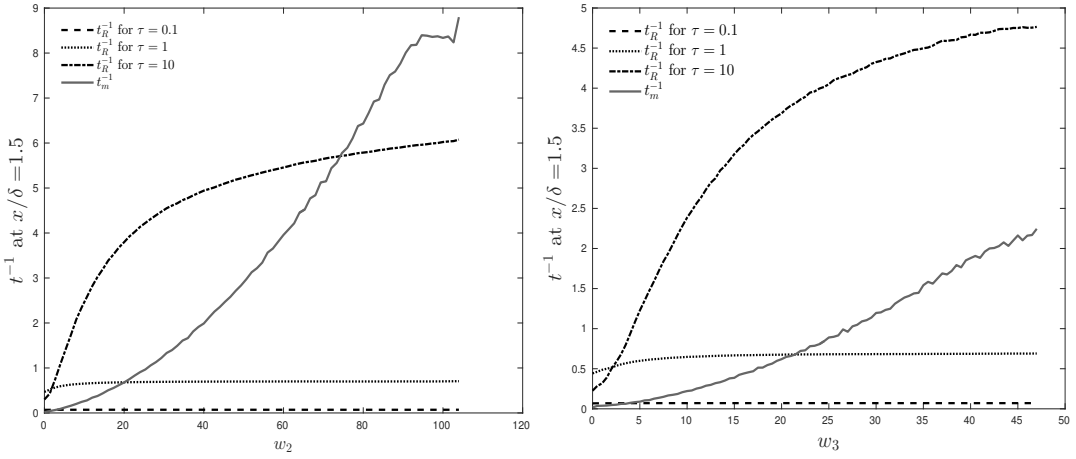

FIGURE 4.20: inverse of characteristic time scales for molecular dissipation and radiative terms at $x/\delta = 1.5$, (a): using transverse spectral information; (b): using longitudinal spectral information

Indeed radiation acts similarly at all scales for $\tau = 0.1$ since t_R is almost constant. The molecular dissipation dominates over radiation terms in the whole frequency range. While increasing the optical thickness, radiative terms grow in relevance causing the appearance of a radiative range where the effects of radiative dissipation and diffusion are larger than the molecular counterparts. For $\tau = 10$ relevance of radiative terms is overshadowing molecular terms in most of the spectra since the characteristic radiative time scale is lower than the molecular time scale. It is interesting to notice that, as expected, the radiative time scale is significantly different in the whole frequency range, reflecting the different behaviour of temperature scales.

From the spectral analysis three main conclusions can be assessed:

- The behaviour of thermal and radiative field interactions, investigated with analytical derivation in homogeneous isotropic turbulence in section 2.4 is noticed to occur in radiative turbulent channel flows. For a low optical thickness the TRI effect mainly translates in a dissipation of thermal turbulence. For a higher optical thickness, energy is withdrawn from the small scales by the action of emission and deposited in the large scales through absorption. A steepening of the thermal energy spectra thus occurs as a consequence of the accumulation of energy in the low frequency range.

- The presence of inhomogenous turbulence delays the above mentioned transition of TRI since energy near the boundaries is stored at higher frequencies of temperature fluctuations. The accumulation of energy in large thermal eddies is therefore noticed particularly in the core of the channel, while in the near wall region a localized energy sink is observed also for high optical thicknesses.

- The development and growth of a "radiative range" in the thermal energy spectrum, where radiation dominates over molecular dissipation and diffusion, can be noticed for intermediate (G1) and large (G10) optical thickness.

Temperature fluctuation contours

A clear visualization of the features described above is obtained with fluid flow snapshot contours. Figure 4.21 shows contours of temperature fluctuation at $x/\delta = 1.5$. The energy reduction due to radiative emission is noticeable in figures 4.21(b) and 4.21(c), while already for $\tau = 1$ an enlargement of the scales can be observed. Figure 4.21(d) shows the characteristic large structures appearing for high optical thickness as described in the section above. On the other hand, figure 4.22 shows snapshots of temperature fluctuations in $x/\delta = 1.93$. The predicted increase in fluctuation levels for $\tau = 0.1$ is displayed, while a clear visualization of temperature variance reduction is observed in figures 4.22(c) and 4.22(d). As stated in section 2.4 small eddies retain relatively optically thin behaviour when the optical thickness increases, this explains why the recovery of fluctuation intensity affects large thermal eddies, while small eddies are further dissipated.

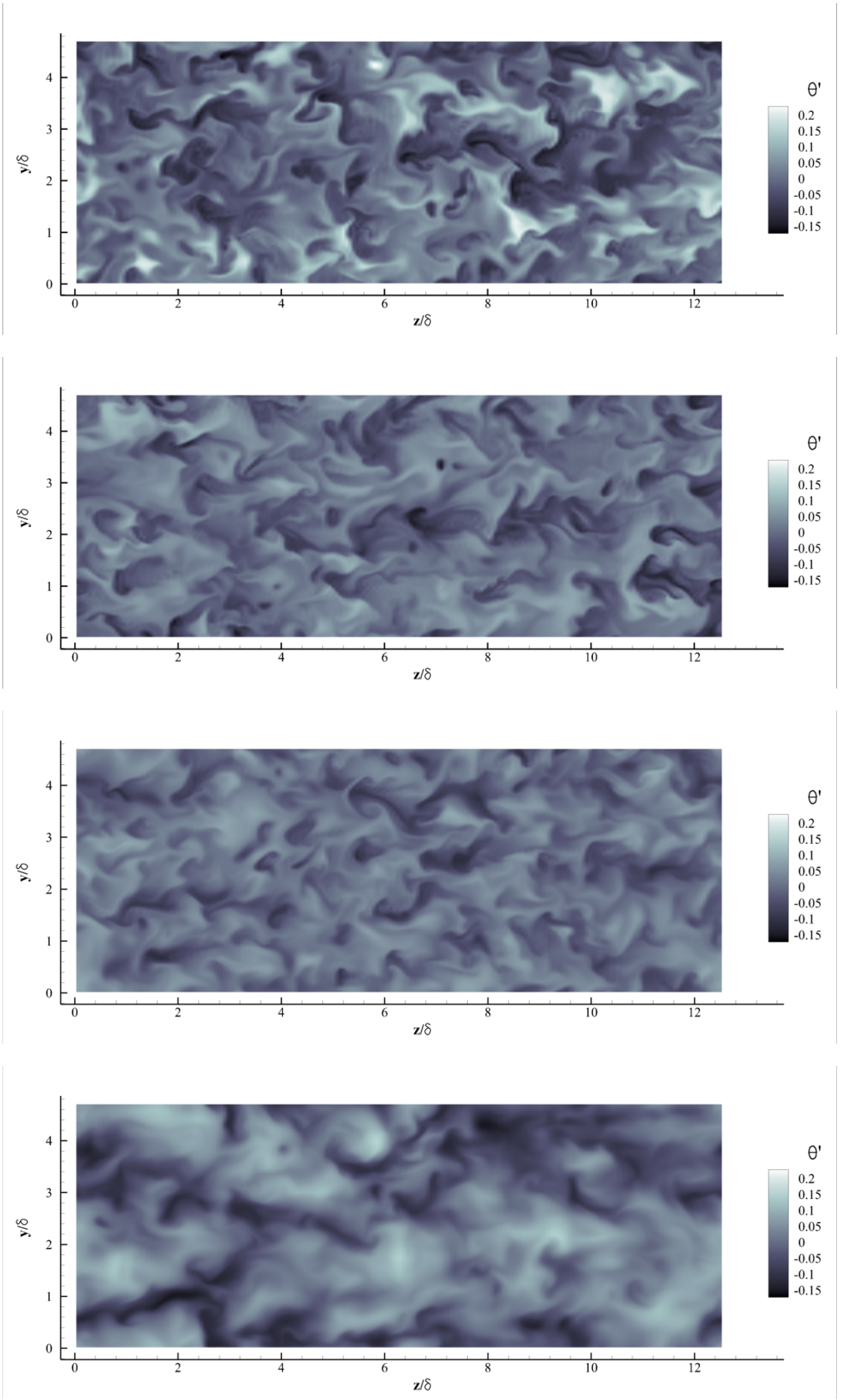

FIGURE 4.21: Snapshots of θ' at $x/\delta = 1.5$; (a): No radiation; (b): $\tau = 0.1$; (c): $\tau = 1.$; (d): $\tau = 10$.

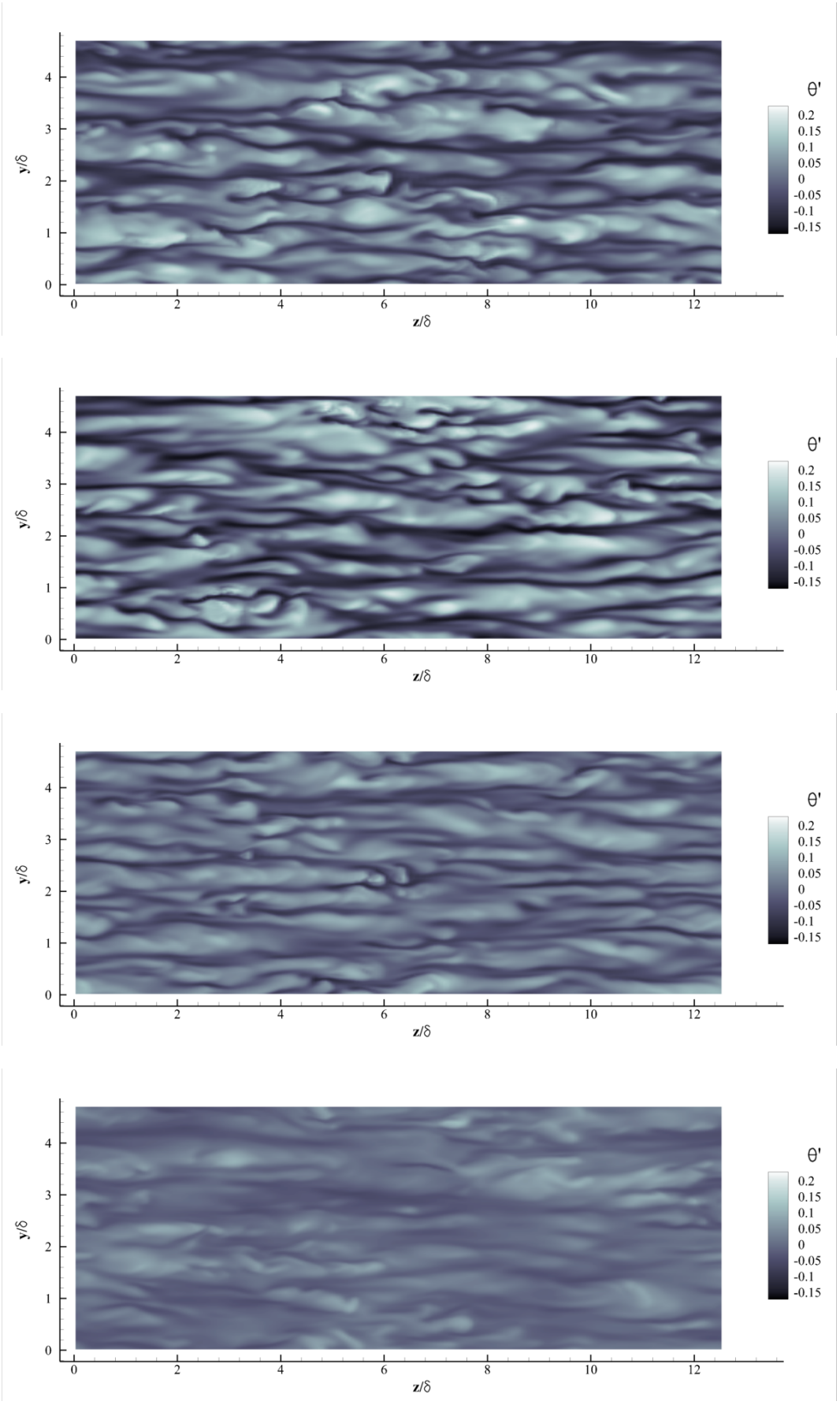

FIGURE 4.22: Snapshots of θ' at $x/\delta = 1.93$; (a): No radiation; (b): $\tau = 0.1$; (c): $\tau = 1.$; (d): $\tau = 10$.

4.2 Variable absorption coefficient

In this section results for $\kappa = f(T)$ simulations will be presented and discussed. The differences between a non-grey and a grey participating media will be highlighted. Analyzed cases are referred as H01,H1 and H10 (see table 3.1).

4.2.1 Mean flow properties

In this section mean quantities are briefly discussed to explain the main differences between cases H and cases G. Contrary to cases G, the absorption coefficient for cases H, defined as in equation (3.9), is characterized by a mean and a fluctuating value.

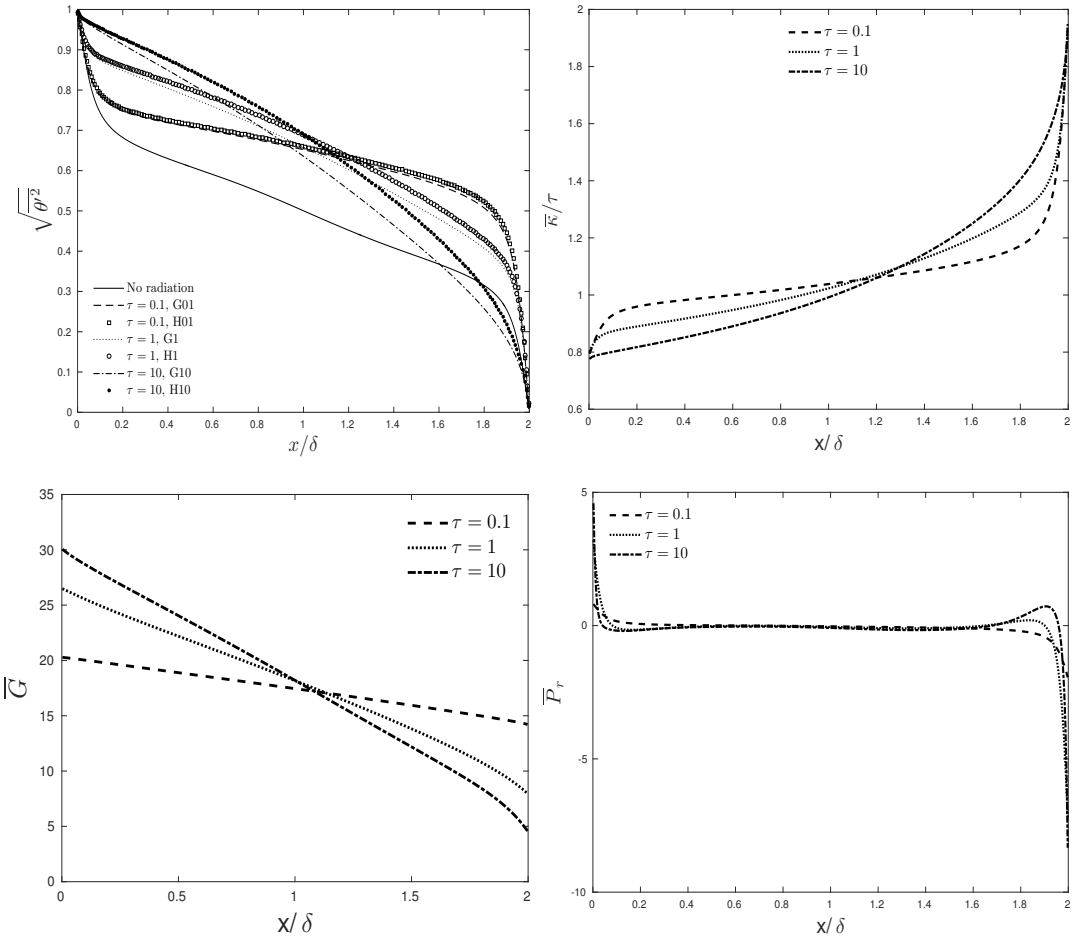

FIGURE 4.23: Averaged profiles. (a): mean temperature; (b): mean absorption coefficient; (c): mean incident radiation; (d): mean radiative heat source

By comparing profiles in figure 4.23(a), it is possible to notice that $\overline{\theta}$ for case H01 is relatively similar to case G01. Although the absorption coefficient varies between 0.08 and 0.2, the medium can still be considered as optically thin, therefore the heat source

remains relatively homogeneous.

A large discrepancy of $\overline{\theta}$ profiles can be observed in the optically thick case (case H10). The absorption coefficient varies roughly between 8 and 20, therefore the flow adjacent to the hot wall experiences a more homogeneous heat source than the fluid on cold side, where the radiative heat flux is more stratified due to the enhanced absorption. The resulting temperature profile has a lower gradient on the hot side when compared to case G10, while a higher gradient occurs on the cold side. The overall temperature is higher for cases H01,H1 and H10 when compared to G01, G1 and G10. The lower absorption coefficient on the hot side enables more intensity to travel towards the core of the channel, while a higher $\overline{\kappa}$ on the cold side prevents loss of energy due to absorption from the wall by confining the fluid-wall contributions to a closer to the wall.

4.2.2 Temperature variance analysis

Figure 4.24 shows a comparison between profiles of $\sqrt{\overline{\theta'^2}}$ for grey and varying κ cases.

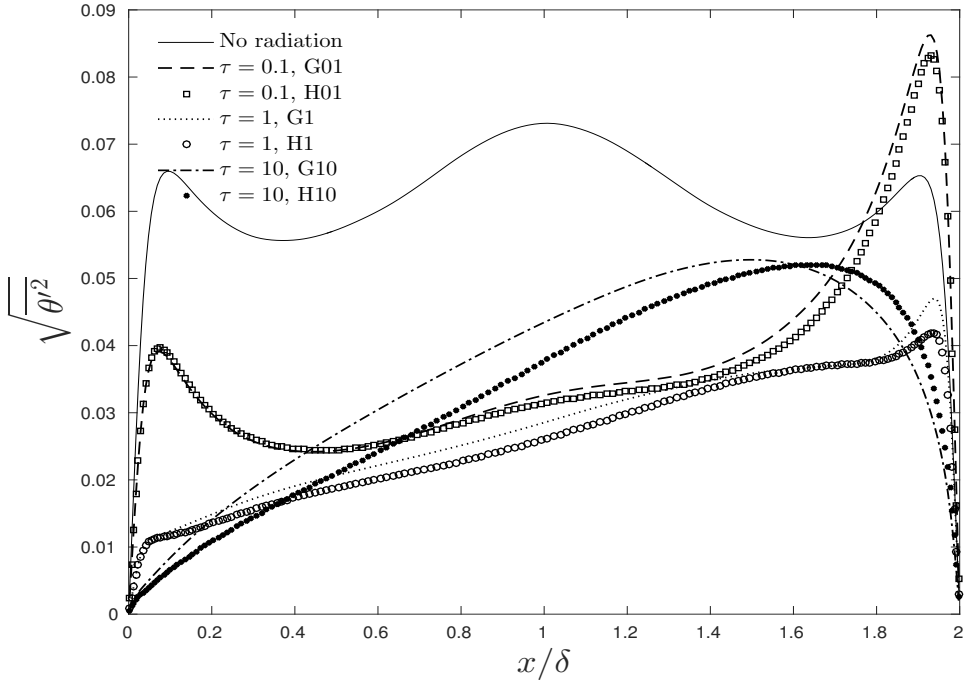

FIGURE 4.24: Temperature root mean square profiles; markers denote varying κ cases, while lines denote grey gas cases

A first noticeable effect of a variable absorption coefficient is a slight reduction of fluctuation levels on the cold side for the low optical thickness case when compared to case G01.

A further reduction in temperature variance can be observed for $\tau = 1$, while in the rising peak zone ($x/\delta \sim 1.6$) fluctuation levels are unaffected by variations in absorption coefficient.

While increasing the optical thickness the tendency inverts and a higher fluctuation intensity is observed on the cold side. On the other hand, on the hot side a reduction in $\overline{\theta'^2}$ occurs. The analysis of the modification of temperature variance must be performed by including κ fluctuations in absorption - temperature and emission - temperature correlations. For cases H01,H1 and H10 useful quantities to investigate, in analogy with E_m and G for grey gas, are $P_e = \kappa E_m$ and $P_a = \kappa G$.

Profiles of emission term $\overline{P'_e\theta'}$ normalized by the optical thickness, compared with $\overline{E'_m\theta'}$ for grey cases are shown in figure 4.25.

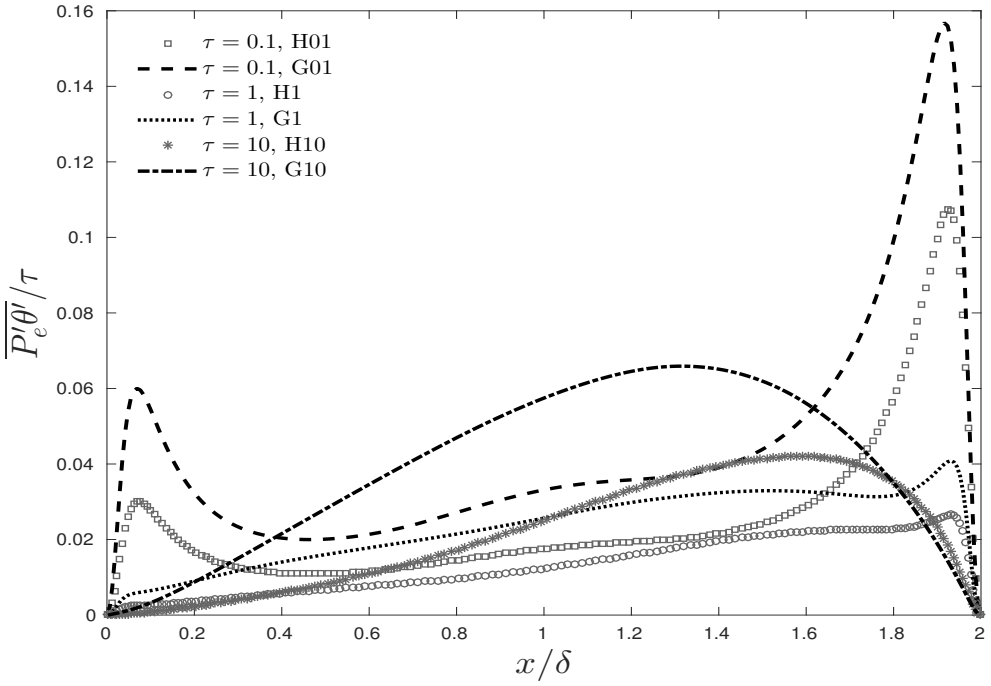

FIGURE 4.25: Emission term normalized by the optical thickness, for variable κ (markers) and grey cases (lines)

Emission term for fluctuating absorption coefficient can be decomposed in:

$$\overline{P'_e\theta'} = \overline{\kappa'\theta'} \cdot \overline{E}_m + \overline{E'_m\theta'} \cdot \overline{\kappa} + \overline{E'_m\theta'\kappa'} \ . \tag{4.19}$$

The magnitude of the last term on the RHS of equation (4.19) is much lower when compared to the other terms and thus can be neglected. While the second term on the RHS is always positive (i.e. positive temperature fluctuations always lead to positive E_m fluctuations), the first term on the RHS is always negative, acting as a reduction in emission dissipation (see figure 4.27(b)). In other words, a positive θ' causes a negative κ' to occur, subsequently reducing the emissive power. The result is a lower emission energy sink for cases H01 and H1 when compared to G01 and G1. For a higher optical thickness ($\tau = 10$) the larger local $\overline{\kappa}$ near the cold wall results in an increase of second term on the RHS of equation (4.19) and causes a localized growth of $\overline{P'_e\theta'}$ beyond the

level for G10.

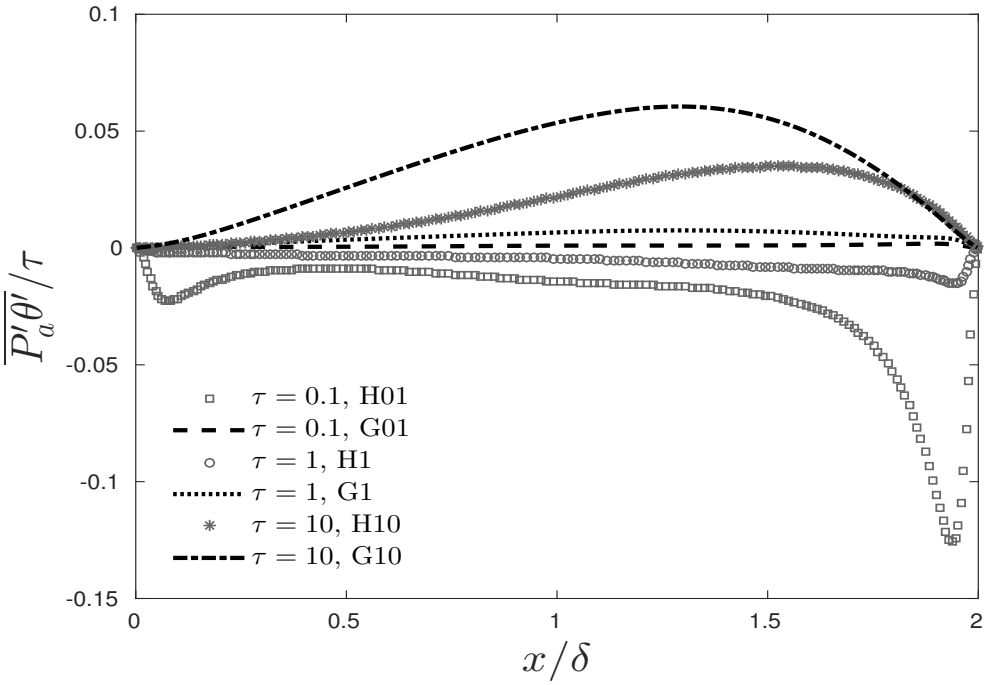

FIGURE 4.26: Absorption term normalized by optical thickness

Figure 4.26 presents plots of the absorption term ($\overline{P'_a\theta'}$) normalized by the optical thickness compared with $\overline{G'\theta'}$ for grey cases. Interestingly, in opposition to G01 and G1, $\overline{P'_a\theta'}$ is negative for cases H01 and H1. Therefore the absorption term acts as a sink of temperature fluctuations, aiding emission in stabilizing temperature profile.

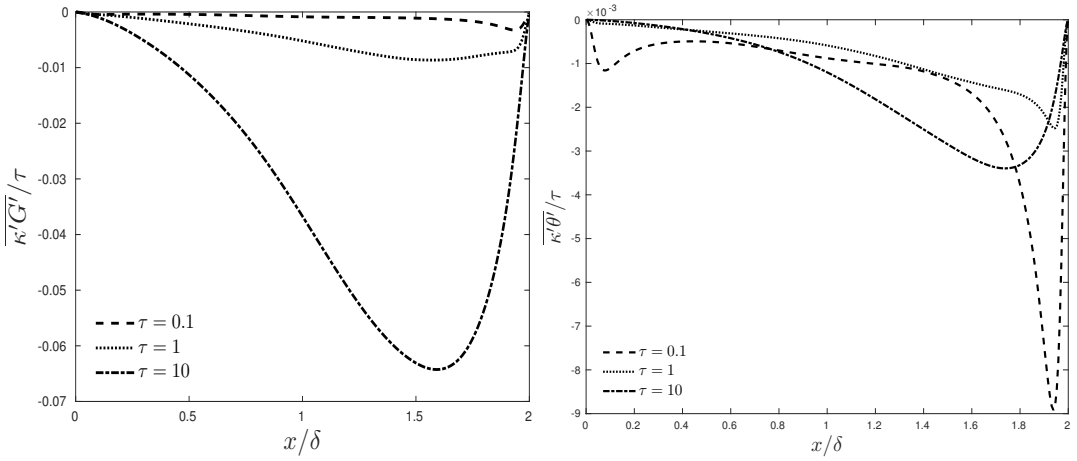

FIGURE 4.27: Absorption coefficient correlations, (a) absorption coefficient - incident radiation correlation normalized on optical thickness; (b): absorption coefficient - temperature correlation normalized on optical thickness

$\overline{P'_a\theta'}$ can be decomposed as:

$$\overline{P'_a\theta'} = \overline{\kappa'\theta'} \cdot \overline{G} + \overline{G'\theta'} \cdot \overline{\kappa} + \overline{\kappa' G'\theta'} \ . \tag{4.20}$$

The last term on the RHS of equation (4.20) is neglected because much smaller than the other two terms. As confirmed by figure 4.27(b), the first term on the RHS (term 1) is always negative since $\kappa \sim 1/\theta$ (i.e. a positive θ fluctuation produces a negative κ fluctuation and vice versa a negative θ' cause a positive κ'). Figure 4.27(a) shows that the second term (term 2) on the RHS of equation (4.20) is always positive since $\overline{\kappa' G'} < 0$ (i.e. a local temperature increases causes a rise in locally available energy for absorption producing a positive absorption fluctuation; vice versa for a local temperature decrease). Therefore, the two terms on the RHS of equation 4.20 counteract each other. At a low and intermediate optical thicknesses (cases H01 and H1) term 1 is dominating over term 2 and $\overline{P'_a\theta'}$ acts as a sink of temperature variance, aiding emission in reducing fluctuations. This causes lower temperature variance for cases H01 and H1 when compared to cases G01 and G1. In other words, a positive temperature fluctuation would result in a lower absorption coefficient and thus a smaller energy absorbed, subsequently reducing the temperature fluctuation itself. At $x/\delta \sim 1.6$ incident radiation fluctuations are high enough to contrast the damping effect of $\overline{\kappa'\theta'}$. Therefore, $\overline{\theta'^2}$ increase to a level comparable to G1. When the absorption coefficient is high enough, term 2 regains strength due to larger G' and dominates over term 1. For case H10 then $\overline{P'_a\theta'}$ reacquires its source role, contrasting emission in reducing thermal fluctuations. The modification of $\overline{\theta'^2}$ on the cold side for case H10 is caused by the higher mean absorption coefficient when compared to case G10 that results in higher $\overline{G'^2}$). On the other hand, a lower $\overline{\kappa}$ on the hot side causes lower $\overline{G'^2}$ ad thus a larger sink of fluctuations due to emission (it is recalled that an increase in $\overline{G'^2}$ directly translates in an increase of $\overline{\theta'^2}$).

It can be inferred from the above figures that in the low to intermediate absorption coefficient range, the effect of a fluctuating κ influences temperature variance more than the effect of a variation of $\overline{\kappa}$ over the channel. On the other hand, for a high optical thickness $\overline{\theta'^2}$ mainly varies due to the variations of $\overline{\kappa}$ from hot to cold side. A summary of κ' and $\overline{\kappa}$ effects on $\overline{\theta'^2}$ is displayed below:

- κ fluctuations for a low and intermediate optical thickness reduce $\overline{P'_e\theta'}$ decreasing the strength of emissive dissipation, but the overall $\overline{P'_r\theta'}$ term is balanced by the effect of absorption that, for variable absorption coefficient, acts as a sink of thermal fluctuations. The combined effect therefore result in a slight decrease of $\overline{\theta'^2}$

- For a high optical thickness ($\tau = 10$), absorption term regains the role of temperature variance source. Due to the higher mean absorption coefficient ($\overline{\kappa} > 10$) on the cold side, the effects described for grey gas are amplified and higher temperature fluctuations can be observed. The opposite occurs on the hot side where an

overall lower absorption coefficient ($\overline{\kappa} < 10$), combined to the effect of κ', results in lower thermal fluctuations. A shift of thermal fluctuation peak towards region of higher absorption coefficient $x/\delta \sim 1.6$ is caused by the amplification of $E_m - G$ caused by $\overline{\kappa}$ (see equation (2.45)).

4.3 Effect of Planck number

In this section results from cases L01, L1 and L10, characterized by a higher Planck number and thus a lower radiative heat transfer relevance, are presented and compared with cases H01, H1 and H10.

4.3.1 Mean flow properties

As for cases H01, H1 and H10 a brief discussion on the average temperature and mean radiative quantities is performed to provide a first insight of the differences among the cases.

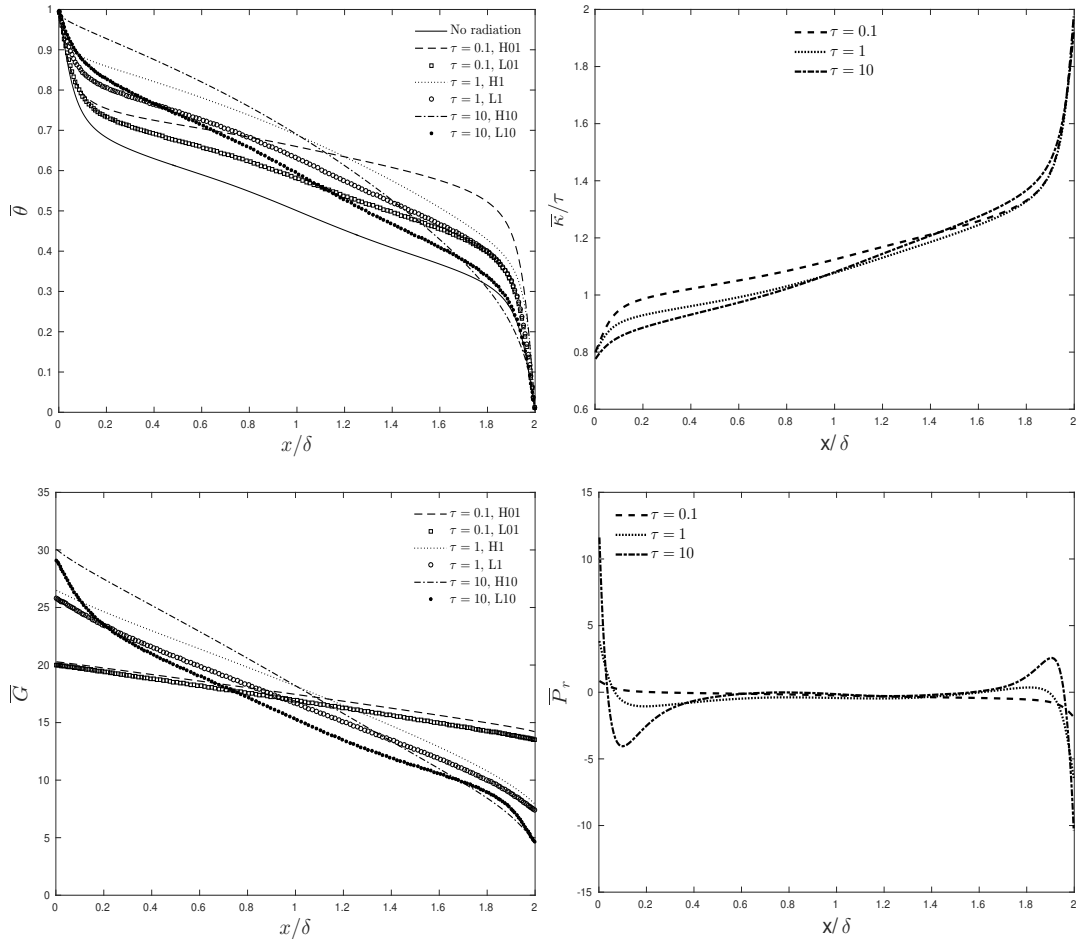

FIGURE 4.28: Averaged profiles. (a): mean temperature; (b): mean absorption coefficient; (c): mean incident radiation; (d): mean radiative heat source

Mean temperature profiles for $Pl = 0.3$ agree with the results by Gupta et al [4] obtained with coupled LES and P_1 of turbulent channel flow. The mean temperature for radiative cases L show a limited deviation from the non radiative case when compared to cases H,

however a substantial increase in bulk temperature can still be observed. Nonetheless, the same features described for figures 4.1(a) and 4.23(a) apply for figure 4.28(a). The temperature gradient near the cold wall is increased for case L01, while further decreasing for L1 and L10. Although the temperature gradient close the cold wall decreases for L10 when compared to L01, contrarily to case G10, a steeper slope of temperature profile when compared to the reference case is retained. In the core of the channel the temperature gradient decreases for case L01 due to the fairly homogeneous distribution of $\overline{G}$, while increasing when the optical thickness is increased due to the more stratified heat source.

4.3.2 Thermal turbulence, temperature variance budgets and spectral analysis

Profiles of $\sqrt{\overline{\theta'^2}}$ for high Planck number cases are shown in figure 4.29.

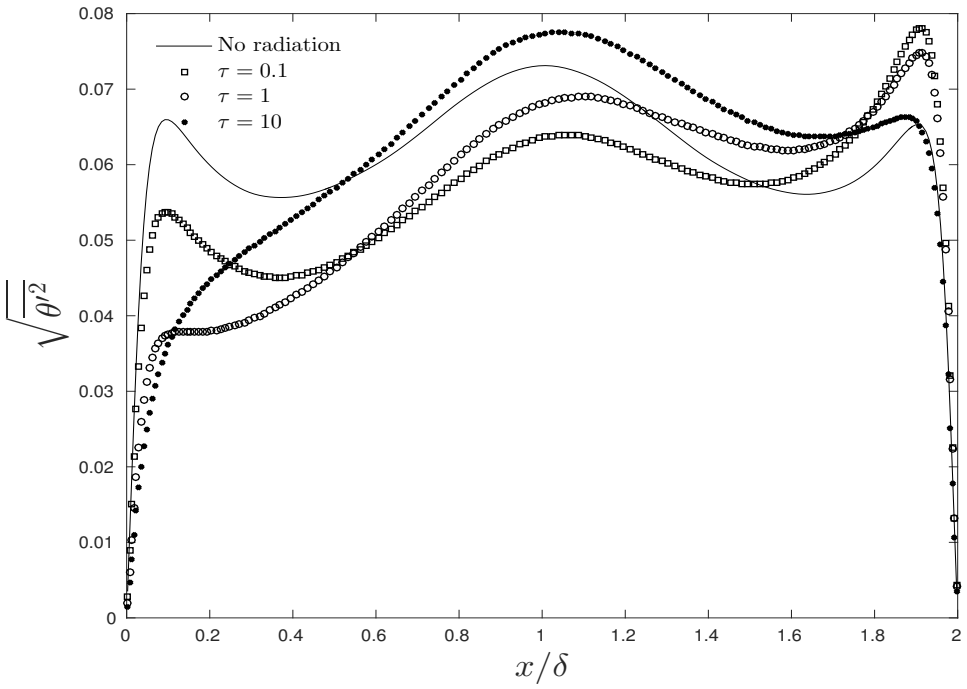

FIGURE 4.29: $\sqrt{\overline{\theta'^2}}$ profiles for $Pl = 0.3$ and various optical thickness.

The temperature variance for a higher Planck number is significantly different with respect to the previous examined cases. Higher temperature gradients on the cold side of the channel produce higher fluctuation levels, while on the hot side a reduction of the temperature variance is noticed. An analysis of figure 4.29 suggests that the differences of $\overline{\theta'^2}$ between a non radiative and a radiative case is mainly due to the effect of $\overline{P}_r$ that reshapes temperature profiles causing a modification in temperature gradient. Therefore, a direct influence of the radiative term is not expected. Due to this reason, for large Planck numbers the radiation budgets of temperature variance are expected

to be relatively small when compared to their molecular counterparts and the spectral modification of thermal structures as discussed for grey gas is not foreseen to occur.

Temperature variance budgets are presented in figure 4.30 for cases L01, L1 and L10. Temperature variance budgets for non radiative channel flow are shown again for comparison.

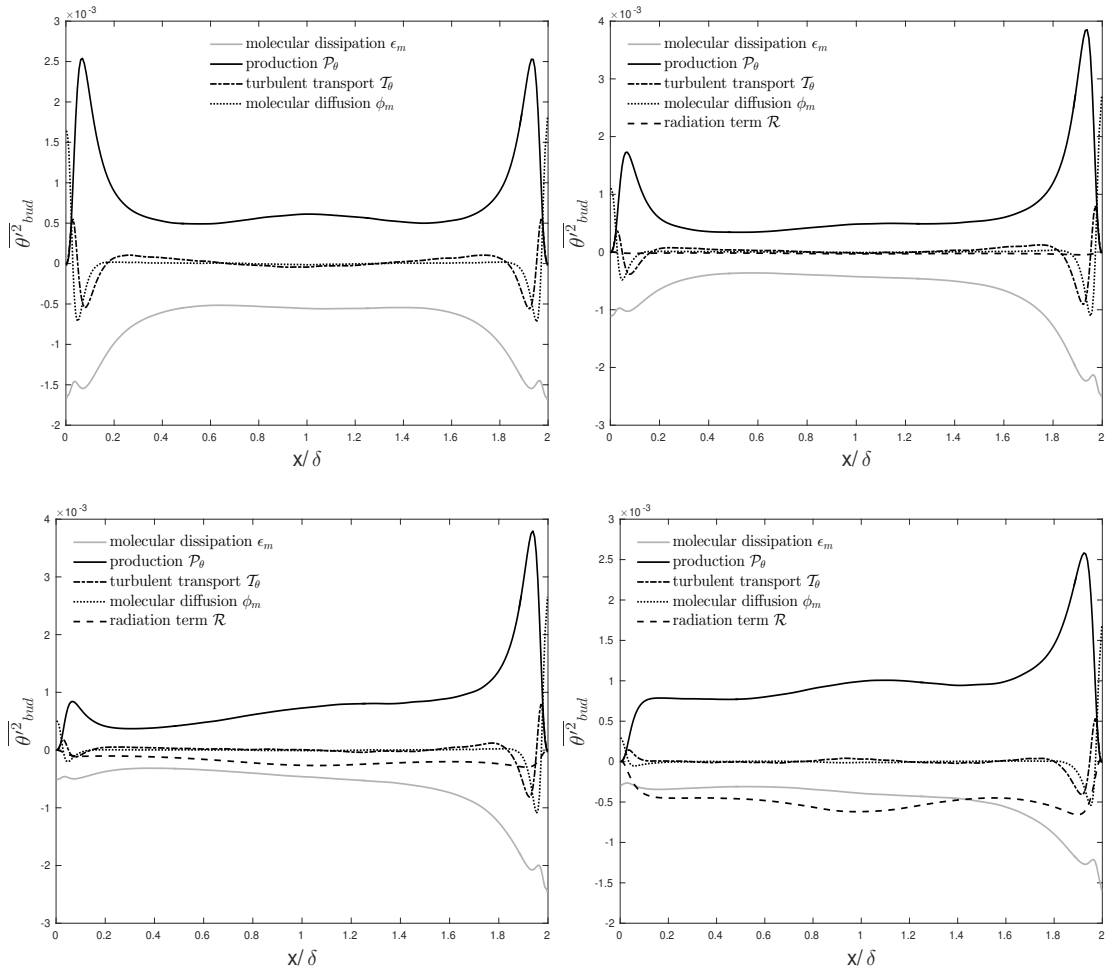

FIGURE 4.30: Temperature variance budgets, (a): non radiative case; (b): case L01, $\tau = 0.1$; (c): case L1, $\tau = 1$; (d): case L10, $\tau = 10$

Indeed, the dependency of the molecular, the production and the radiative terms on the optical thickness shows that the direct influence of radiative field fluctuations is minor when compared to the effect of the mean radiative field. The increased production caused by the modification of the mean temperature profiles is balanced mostly by molecular dissipation. For $\tau = 0.1$ $\mathcal{R}$ is negligible, confirming the results obtained by Sakurai et al [1] for an optically thin channel flow. It is possible to conclude that, while increasing the Planck number, the strength of radiative terms is greatly reduced and as a consequence molecular terms are much larger when compared to the previously examined cases. Despite the reduction in the radiation relevance for cases L, the patterns

explained in section 4.1.4 are still noticeable (i.e. radiation causes the loss of symmetry between hot and cold side and affects mostly the center of the channel, where a production increase is noticed. The radiation term increases in relevance upon increasing the optical thickness, while molecular terms reduces).

Figure 4.31 shows respectively longitudinal and transverse thermal energy spectra at $x/\delta \sim 1.07$.

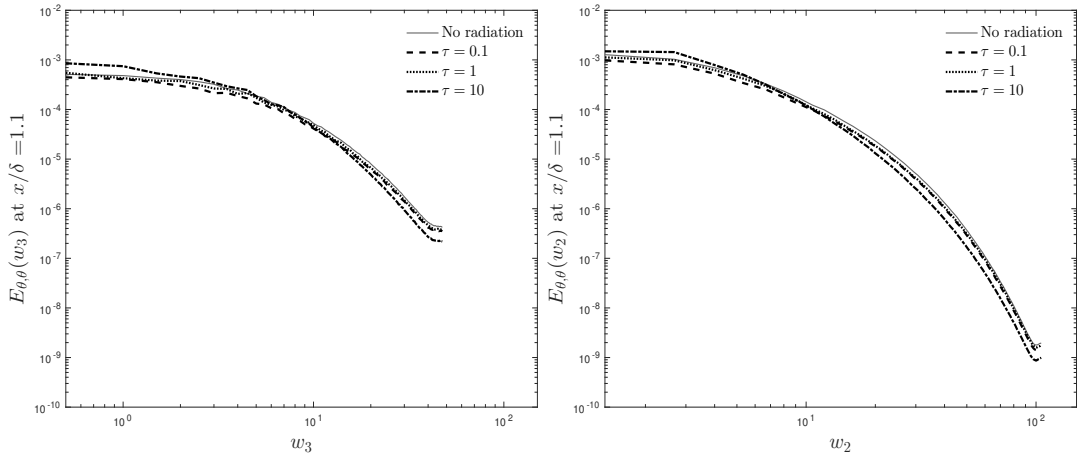

FIGURE 4.31: Temperature energy spectra $E_{\theta,\theta}$ at $x/\delta = 1.1$, (a): longitudinal energy spectra; (b): transverse energy spectra

The accumulation of energy at larger scales when dealing with a large optical thickness is still visible but has a much lower effect on the temperature spectra when compared to figures shown in section 4.1.6. Similarly occurs with the energy sink throughout the spectra, which is greatly reduced when compared to cases H. An improved visualization can be obtained by plotting contours of pre-multiplied energy spectra normalized by local temperature variance ($w_2 E_{\theta,\theta}/\overline{\theta'\theta'}$) to investigate the redistribution of energy over the scales within the channel.

Figures 4.32 and 4.33 show contours of pre-multiplied normalized transverse temperature energy spectra for cases Ref and L01 and for cases L1 and L10, respectively. The modifications of thermal structures is not clearly visible comparing non radiative case with L01 and L1. The slight appearance of energy redistribution in the center of the channel is noticeable for $\tau = 10$. From the analysis of the above figures it is possible to conclude that a lower Planck number acts as intensification of the optical thickness and radiative effects described in section 4.1. Therefore, all the characteristics of turbulence radiation interactions described in section 4.1 remain valid and are further amplified or reduced by a respectively low and high Planck number.

4.4 Turbulent heat flux modeling in radiative flows

Reynolds average energy equation for turbulent channel flow, in presence of radiation, reads:

$$\frac{\partial \overline{\theta}}{\partial t} = \frac{1}{RePr}\frac{\partial^2 \overline{\theta}}{\partial x^2} - \frac{1}{RePrPl}\overline{P_r} - \frac{\partial \overline{u'\theta'}}{\partial x} \ . \tag{4.21}$$

The last term on the RHS, representing the turbulent mixing due to turbulent heat flux, is an unclosed term and requires a closure. Several closures have been developed for non radiative situations, the easiest and most popular is the "gradient diffusion approximation". This approach aligns turbulent heat flux to mean temperature gradient ($\overline{u'\theta'} \sim \partial\overline{\theta}/\partial x$) scaling it, in analogy with the eddy viscosity approximation, with the definition of an eddy diffusivity α_t. Turbulent diffusivity is then related to the eddy

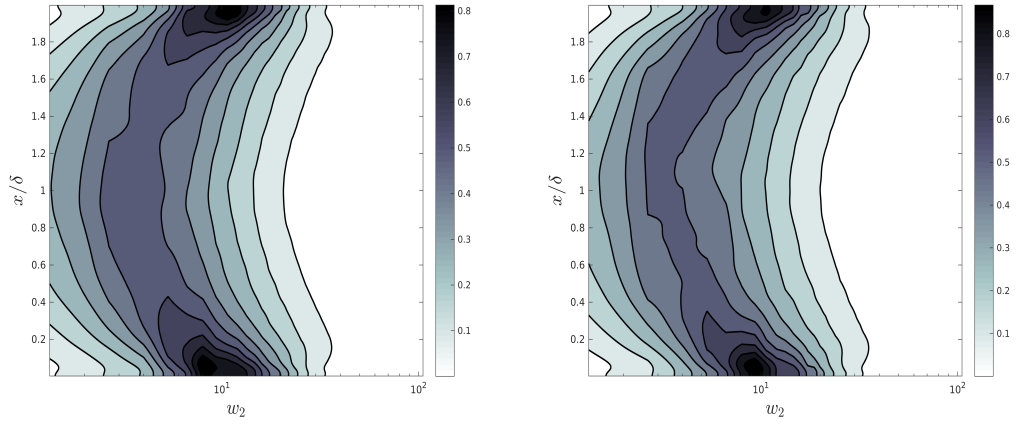

FIGURE 4.32: Pre-multiplied, normalized thermal energy spectra contours $w_2 E_{\theta,\theta}/\overline{\theta'\theta'}$; (a): no radiation case; (b) $\tau = 0.1$

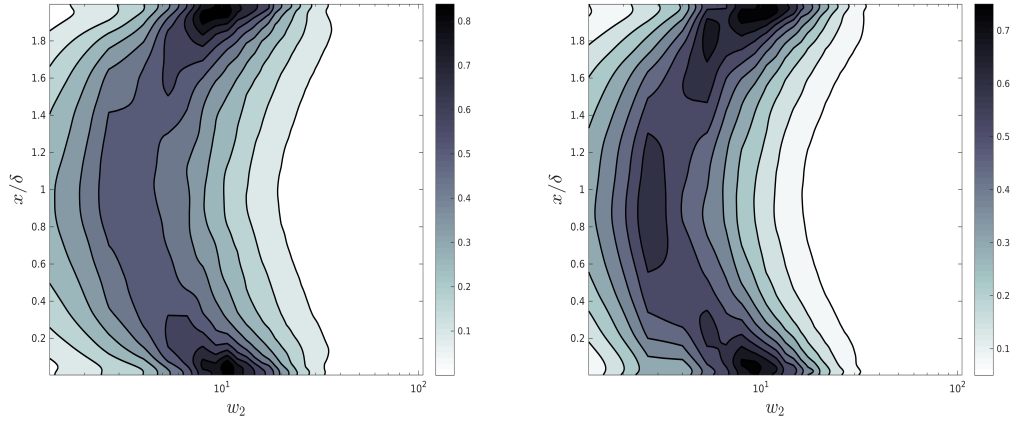

FIGURE 4.33: Pre-multiplied, normalized thermal energy spectra contours $w_2 E_{\theta,\theta}/\overline{\theta'\theta'}$; (a): $\tau = 1$; (b) $\tau = 10$

viscosity (ν_t) by the definition of a turbulent Prandtl number:

$$Pr_t = \frac{\nu_t}{\alpha_t} = \frac{\overline{u'w'}}{\overline{u'\theta'}} \frac{\partial\overline{\theta}/\partial x}{\partial\overline{w}/\partial x} \ . \tag{4.22}$$

In this section the only developed model for turbulent Prandtl number in radiative turbulent flows existent in literature, proposed by Zhang [3], is explained and validated in this work for low to high optical thicknesses for grey gas.
The starting point of the model developed by Zhang is the normalizaton of turbulent heat flux with a radiative-based scaling factor (γ) that ensures (assumption 1):

$$\frac{\overline{u'\theta'}_R}{\gamma_R} \approx \frac{\overline{u'\theta'}_0}{\gamma_0} \ , \tag{4.23}$$

where the subscripts R and 0 denote quantities for radiative and non radiative cases, respectively. If property above holds, it is possible to obtain a relation between eddy diffusivity and turbulent heat flux for a non radiative case as:

$$\alpha_t = \frac{1}{\rho c_p} \frac{\overline{u'\theta'}_R}{(\partial\overline{\theta}/\partial x)_R} = \frac{1}{\rho c_p} \frac{\gamma_R}{(\partial\overline{\theta}/\partial x)_R} \frac{\overline{u'\theta'}_0}{\gamma_0} \ . \tag{4.24}$$

The normalization factor γ is calculated as:

$$\gamma(x) = \overline{q}_w - \overline{q}_R(x) \ , \tag{4.25}$$

where $\overline{q}_w$ is the wall heat flux while $\overline{q}_R(x)$ is the radiative heat flux within the channel. When no radiative heat transfer is involved, the normalization factor reduces to $\gamma_0 = \overline{q}_{w,cd}$.
Assuming that $\alpha_R \approx \alpha_0$ (assumption 2) and that radiation has no influence on the velocity field $\nu_{tR} \approx \nu_{t0}$ (assumption 3), and rearranging equation (4.25) gives the relation for turbulent Prandtl number in a constant property radiative turbulent flow (see Zhang et al [3] for details):

$$Pr_{tR} = \frac{1}{RePr} \frac{(\partial\overline{\theta}/\partial x)_R}{\gamma_R} (Pr_{t0} + \nu_{t0} Re) \ . \tag{4.26}$$

Assumption 2 is always satisfied in the present work due to the constant property assumption, while assumption 3 is always satisfied due to the assumption of passive temperature (no back coupling of energy equation in momentum equation). The resulting profiles of modeled and calculated turbulent Prandtl number are shown in figure 4.34. To highlight the effects of radiation in modeling turbulent Prandtl number and avoid errors derived by modeling of Pr_{t0} the correct value of non radiative turbulent Prandtl number, calculated from DNS, is used to model Pr_{tR}.

The high gradient and weird behaviour of Pr_t in the center of the channel is due to $\overline{u'w'}$ reaching zero not in the exact location of $\partial\overline{w}/\partial x$, resulting in a singular point for ν_t.

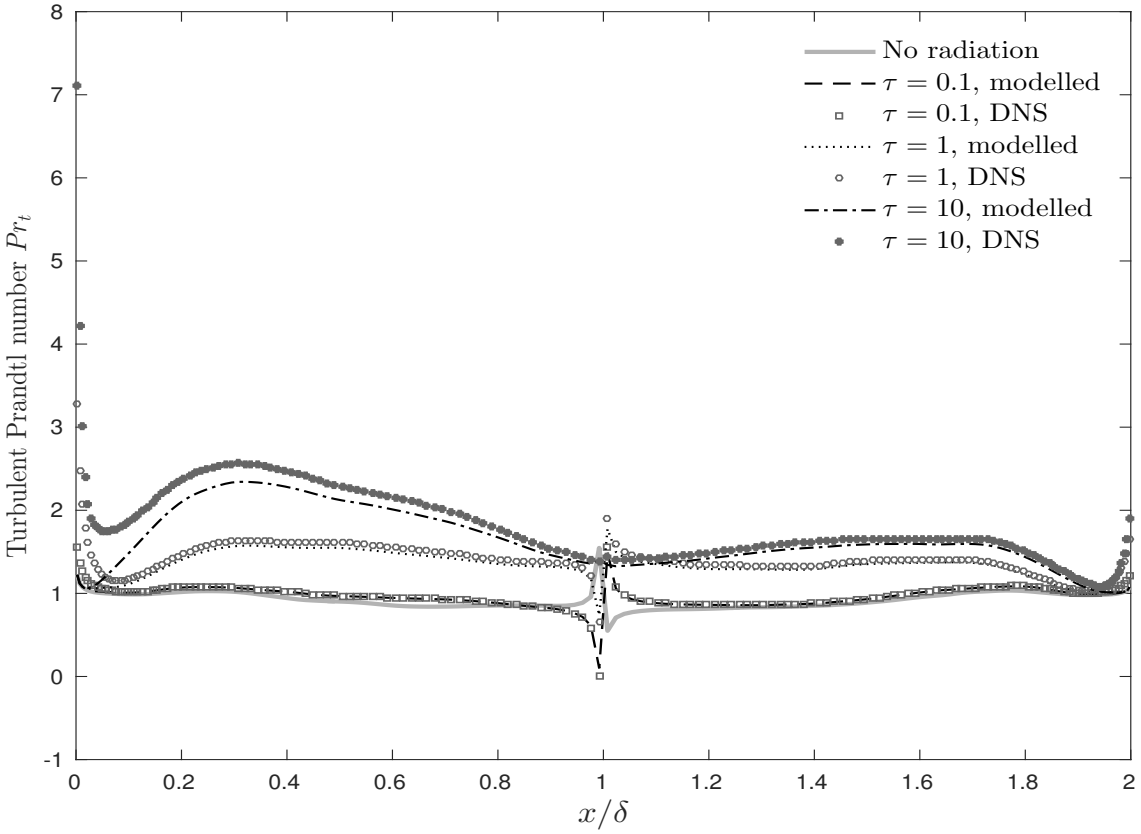

FIGURE 4.34: turbulent Prandtl number calculated for case Ref, and comparison between calculated and modeled Pr_{tR} for cases G01,G1 and G10

The turbulent Prandtl number increases significantly when increasing the optical thickness, depicting the decrease in convective effects on mean temperature with increasing τ (as already explained in section 4.1.2). The model developed by Zhang performs exceptionally well with low optical thickness (case G01), being able to exactly reproduce Pr_{tR}. For intermediate values of optical thickness the model seems to deviate even so slightly from the calculated values, while showing a relevant deviation for higher values of optical thickness ($\tau = 10$).

The reason of this deviation can be found in the definition of assumption 1. For clarity let us define:

$$\mathcal{U} \equiv \overline{u'\theta'} \ , \quad \mathcal{D} \equiv -\frac{1}{RePr}\frac{\partial \overline{\theta}}{\partial x} \ . \tag{4.27}$$

Since equation (4.2) holds, it is true that:

$$\mathcal{U} + \mathcal{D} = \overline{q}_w - \overline{q}_R = \gamma \ . \tag{4.28}$$

Assumption 1 (4.23) can be rewritten as follows:

$$\frac{\mathcal{U}_R}{\mathcal{U}_R + \mathcal{D}_R} \approx \frac{\mathcal{U}_0}{\mathcal{U}_0 + \mathcal{D}_0} \ . \tag{4.29}$$

Stating that relation (4.29) subsists is equivalent to saying:

$$\frac{\mathcal{D}_R}{\mathcal{U}_R} \approx \frac{\mathcal{D}_0}{\mathcal{U}_0} \ , \tag{4.30}$$

i.e. the relative importance of conduction over turbulent heat transfer remains constant as radiation is introduced and optical thickness is increased. Condition (4.30) can be met identically only if Pr_t is constant since turbulent Prandtl number is defined as:

$$Pr_t = -\frac{\mathcal{D}}{\mathcal{U}} \cdot \nu_t RePr \ , \tag{4.31}$$

and in developing the model ν_t has been assumed constant throughout the cases (assumption 3).

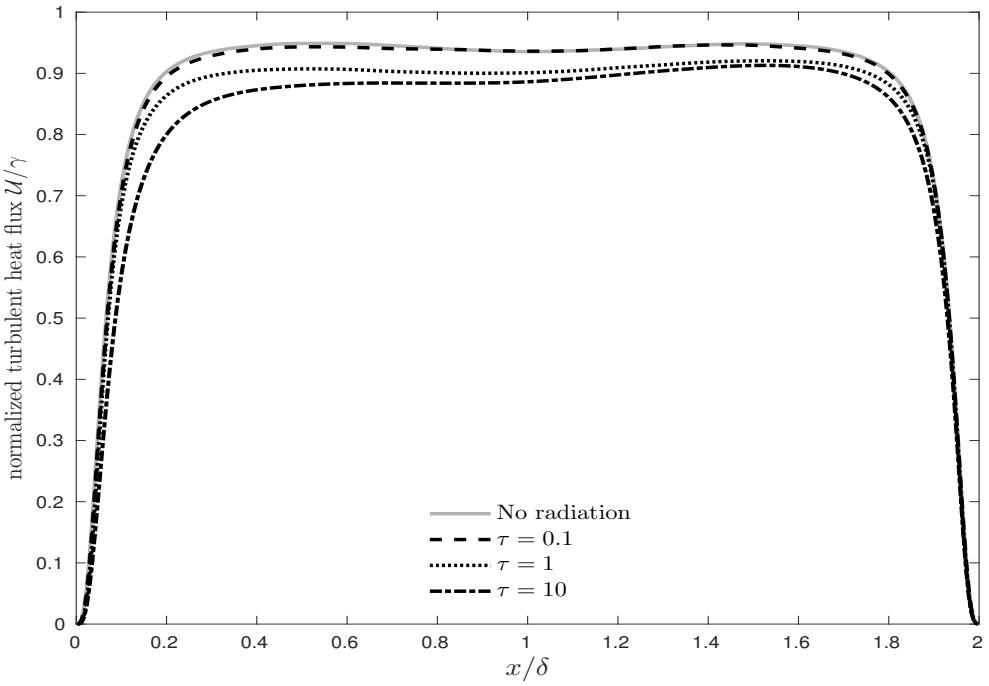

FIGURE 4.35: $\mathcal{U}$ normalized with radiation-based scaling as proposed by Zhang et al [3] for cases Ref, G01, G1 and G10

Figure 4.35 shows profiles of $\mathcal{U}/\gamma$ for all the different cases. Condition (4.29) can be met when $\frac{\mathcal{D}_R}{\mathcal{U}_R} \ll 1$ as it occurs in the core for a non radiative turbulent channel flow. As it appears, for a low optical thickness the decrease of $\mathcal{U}$ is balanced by the decrease in temperature gradient, resulting in the validity of assumption 1. Therefore, the modeled turbulent Prandtl number for a low optical thickness agrees with the value calculated from DNS. However, condition (4.29) is never met when increasing the optical thickness since mean temperature profiles are significantly altered, with a relevant gradient increase in the core of the channel (see figure 4.1(a)). This increase causes $\mathcal{U}_R/\gamma_R < \mathcal{U}_0/\gamma_0$ resulting in negative deviation of the modeled turbulent Prandtl number when compared to the calculated one, mostly on the hot side where $\mathcal{D}$ increases and $\mathcal{U}$ drops.

Indeed a correction on $\mathcal{D}_R$ in order to balance condition (4.29) would result in a better agreement between modeled and calculated Pr_t. Unfortunately, an empirical correction is no use in a modeling perspective, due to the specificity of the present case, but still confirms the cause of deviation at high optical thickness and provides a theoretical base in order to improve the already existing model. It has to be highlighted that no direct action on $\mathcal{D}$ in γ can be performed, since γ in a RANS framework is calculated as $\overline{q}_w - \overline{q}_R$. Due to lack of time turbulent Prandtl modeling was not further investigated, and the discovery of an enhanced normalization that could represent a broader optical thickness and Planck number range and therefore upgrade the existing model is left for further developments.

Chapter 5

Conclusions and Recommendations

5.1 Conclusions

In the present work, a comprehensive study of turbulence radiation interactions in non reactive turbulent channel flow has been performed. The modification of the temperature field upon varying the optical thickness in a grey radiative turbulent channel flow has been extensively investigated with the aid of temperature variance budgets, turbulent energy spectra and temperature 2-point autocorrelations. The results show a different qualitative behaviour of turbulence radiation interactions (TRI) when different optical depths are considered, and highlight particularly the contrasting effects of radiative absorption and emission in TRI.

For a low optical thickness ($\tau = 0.1$) the role of absorption is limited to the modification of mean profiles since incident radiation (G) is not influenced by thermal fluctuations. On the other hand, emission affects the whole temperature spectra, stabilizing temperature and reducing thermal fluctuations mainly in the channel core. For an intermediate case ($\tau = 1.$) the effects are amplified and a strong depletion of the thermal fluctuation field is noticed because of emission. When increasing the optical depth to moderately optically thick levels ($\tau = 10$), thermal fluctuations show a large influence on absorption, experiencing a stronger coupling between incident radiation (G) and temperature variance. The effect of a larger absorption fluctuation field is translated in a transition of TRI: for a high optical thickness, energy is withdrawn from the whole spectrum irrespective of frequency levels due to a tight coupling of emission and temperature fluctuations, and it is accumulated on the large scales that are more sensitive to absorption. The effects described in section 2.4 by analytical derivation describe thus correctly the

transition of TRI between optically thin and thick media, shifting from a purely dissipative effect to a preferential redistribution of energy over frequencies. The effect of inhomogeneuos turbulence (i.e. the presence of boundaries) results in a enhancement of the aforementioned TRI transition towards the center of the channel, where larger structures can absorb and contain the redistributed energy.

Furthermore, a study of the budgets of temperature variance show that with an increase of optical thickness the direct effect of radiation on thermal turbulence increases drastically, replacing the role of molecular terms in dissipating and redistributing temperature variance. The radiative term ($\mathcal{R}$) has been investigated by decomposition in two quantities, namely radiative diffusion ϕ_r and radiative dissipation ϵ_r, in analogy with molecular terms, and as the optical thickness is increased a similarity between the behaviour of radiative and molecular terms can be observed.

Moreover a radiative turbulent channel flow characterized by a variable absorption coefficient has been investigated in order to quantify the effect of a variable κ on turbulence radiation interaction. The findings suggest that the dissipative effect of TRI on thermal fluctuations is increased with the introduction of κ fluctuations, thus slightly reducing temperature variance. The transition of TRI from optically thin to optically thick media is noticed to occur within the channel due to the effect of a strongly varying $\overline{\kappa}$.
Finally the effect of the Planck number is investigated. The temperature variance profiles appear to be largely different for a higher Planck number. A thorough investigation revealed that the different thermal fluctuation levels are due to the larger relevance of molecular terms and turbulent transport. However, despite being weakened, the behaviour of radiative terms, and the above mentioned TRI transition is retained for higher Planck number values. It can be concluded that Planck number acts only as an amplification or damping factor, highlighting or smoothing the TRI effects on thermal turbulence, without changing the underlying physics of TRI.

5.2 Recommendations

The results obtained provide a general and comprehensive study on the effect of TRI for various optical depths. If a more accurate characterization of higher order statistics is required, it is recommended to use of a more accurate radiation solver, especially for higher values of τ. This can be achieved by either improving the current spatial discretization scheme, or by implementing a Monte Carlo radiation solver. Furthermore, the non-grey effects can be better understood by employing an improved radiation spectral modeling that can handle spectral intensity and absorption coefficient. Finally, the investigation of even larger optical depths is recommended in order to investigate strong

TRI as depicted by figures 2.12 and 2.13 in section 2.4, which show the tight coupling of incident radiation over all the scales for a large enough κ.

Appendix A

Reynolds Averaged Navier Stokes Equations

Reynolds averaging procedure enables the simplification of the full Navier-Stokes equations, by dealing only with mean quantities.
Reynolds decomposition refers to the separation of a turbulent variable f into a mean part, denoted by a bar, and a fluctating part, denoted by a prime: $f = \overline{f} + f'$.
Reynolds averaging operator should sadisfy the following conditions:

(1) $\overline{f+g} = \overline{f} + \overline{g}$

(2) $\overline{cf} = c \cdot \overline{f}$ with c a constant

(3) $\overline{\frac{\partial f}{\partial s}} = \frac{\partial \overline{f}}{\partial s}$ with s a spatial or temporal coordinate

(4) $\overline{\overline{f}g} = \overline{f}\overline{g}$

Condition (4) with $g = 1$, combined with condition (2) yields the final two conditions:

(5) $\overline{\overline{f}} = \overline{f}$

(6) $\overline{f'} = 0$

The continuity equation, the instantaneous Navier-Stokes equations and the energy equation for an incompressible non radiative fluid read:

$$\frac{\partial u_i}{\partial x_i} = 0 \ , \tag{A.1}$$

$$\frac{\partial u_i}{\partial t} + \frac{\partial u_j u_i}{\partial x_j} = -\frac{\partial p}{\partial x_j} + \nu \frac{\partial^2 u_i}{\partial x_j^2} \ , \tag{A.2}$$

$$\frac{\partial T}{\partial t} + u_j \frac{\partial T}{\partial x_j} = \frac{k}{\rho c_p} \frac{\partial^2 T}{\partial x_j^2} \ . \tag{A.3}$$

Reynolds averagind applied to equation (A.1) yields (with the use of condition (3)):

$$\frac{\partial \overline{u_i}}{\partial x_i} = 0 \ , \tag{A.4}$$

and therefore:

$$\frac{\partial u_i'}{\partial x_i} = 0 \ , \tag{A.5}$$

hence continuity for an incompressible fluid is valid both for the mean and the fluctuating velocity. Averaging equation (A.2) and applying conditions (1),(2) and (3), yields:

$$\frac{\partial \overline{u_i}}{\partial t} + \frac{\partial \overline{u_j u_i}}{\partial x_j} = -\frac{\partial \overline{p}}{\partial x_j} + \nu \frac{\partial^2 \overline{u_i}}{\partial x_j^2} \ . \tag{A.6}$$

The advective term can then be decomposed with Reynold decomposition as:

$$\overline{u_j u_i} = \overline{(\overline{u_j} + u_j')(\overline{u_i} + u_i')} = \overline{\overline{u_j u_i} + u_j' u_i' + \overline{u_j} u_i' + u_j' \overline{u_i}} \ , \tag{A.7}$$

therefore applying condition (1) and (4)

$$\overline{u_j u_i} = \overline{u_j u_i} + \overline{u_j' u_i'} + \overline{u_j} \overline{u_i'} + \overline{u_j'} \overline{u_i} \ , \tag{A.8}$$

Since condition (6) applies, the end form of Reynolds Averaged Navier Stokes equations (RANS) yields:

$$\frac{\partial \overline{u_i}}{\partial t} + \frac{\partial \overline{u_j u_i}}{\partial x_j} = -\frac{\partial \overline{p}}{\partial x_j} + \nu \frac{\partial^2 \overline{u_i}}{\partial x_j^2} - \frac{\partial \overline{u_j' u_i'}}{\partial x_j} \ . \tag{A.9}$$

By applying Reynolds averaging to equation (A.3) and considering conditions (1), (2), and (3):

$$\frac{\partial \overline{T}}{\partial t} + \frac{\partial \overline{u_j T}}{\partial x_j} = \frac{k}{\rho c_p} \frac{\partial^2 \overline{T}}{\partial x_j^2} \ . \tag{A.10}$$

Same decomposition as in equation (A.8) can be performed for term $\overline{u_j T}$ yielding:

$$\frac{\partial \overline{T}}{\partial t} + \frac{\partial \overline{u_j} \overline{T}}{\partial x_j} = \frac{k}{\rho c_p} \frac{\partial^2 \overline{T}}{\partial x_j^2} - \frac{\partial \overline{u_j' T'}}{\partial x_j} \ . \tag{A.11}$$

Terms $\overline{u_j' u_i'}$ and $\overline{u_j' T'}$ are respectivly defined as Reynolds shear stress and Turbulent heat flux. They are both unclosed terms, meaning that solving the above sets of equations do not provide the values of $\overline{u_j' u_i'}$ and $\overline{u_j' T'}$. Due to this reason numerical solution of RANS equations relies on the correct modelling of the above mentioned Reynolds terms. Reynolds averaging will be applied furter for the derivation of the temperature variance budget equation.

Appendix B

Derivation of temperature variance transport equation

The transport equation for temperature variance is derived from the energy equation and helps to analyse and understand the level of thermal turbulence in the flow. Let us consider the energy equation (see chapter 3), to which the Reynolds averaged energy equation (see appendix A) is subtracted, yielding:

$$\frac{\partial \theta'}{\partial t} + \frac{\partial \overline{u_j}\theta'}{\partial x_j} + \frac{\partial u_j'\overline{\theta}}{\partial x_j} + \frac{\partial u_j'\theta'}{\partial x_j} - \frac{\partial \overline{u_j'\theta'}}{\partial x_j} = \frac{1}{RePr}\frac{\partial^2 \theta'}{\partial x_j^2} - \frac{P_r'}{RePrPl} \ , \tag{B.1}$$

where P_r' can be decomposed in its emitting and absorbing contributions (as done in chapter 4):

$$P_r' = \kappa E_m' - \kappa G' \ . \tag{B.2}$$

The continuity equation of incompressible flows states (see Appendix A:

$$\frac{\partial u_j}{\partial x_j} = \frac{\partial \overline{u_j}}{\partial x_j} = \frac{\partial u_j'}{\partial x_j} = 0 \tag{B.3}$$

Therefore the LHS of equation B.1 can be simplified making use of the continuity equation as:

$$\frac{\partial \theta'}{\partial t} + \overline{u_j}\frac{\partial \theta'}{\partial x_j} + u_j'\frac{\partial \overline{\theta}}{\partial x_j} + \frac{\partial u_j'\theta'}{\partial x_j} - \frac{\partial \overline{u_j'\theta'}}{\partial x_j} \tag{B.4}$$

Equation B.1 is then multiplied by θ' and averaged by means of Reynolds averaging. Making use of derivation properties, and taking in account the principles of Reynolds averaging:

$$\frac{1}{2}\frac{\partial \overline{\theta'^2}}{\partial t} + \frac{\overline{u_j}}{2}\frac{\partial \overline{\theta'^2}}{\partial x_j} + \overline{u_j'\theta'}\frac{\partial \overline{\theta}}{\partial x_j} + \frac{1}{2}\frac{\partial \overline{u_j'\theta'^2}}{\partial x_j} = \frac{1}{2RePr}\frac{\partial^2 \overline{\theta'^2}}{\partial x_j^2} - \frac{1}{RePr}\overline{\left(\frac{\partial \theta'}{\partial x_j}\right)^2} - \frac{\overline{P_r'\theta'}}{RePrPl} \tag{B.5}$$

Since the flow is statistically steady, homogeneous in the streamwise and spanwise directions (y and z) and $\overline{u} = \overline{v} = 0$, the above equation can be simplified as:

$$0 = -2\overline{u'\theta'}\frac{\partial\overline{\theta}}{\partial x} + \frac{\partial}{\partial x}\left(\frac{1}{RePr}\frac{\partial\overline{\theta'^2}}{\partial x} - \overline{u'\theta'^2}\right) - \frac{2}{RePr}\overline{\left(\frac{\partial\theta'}{\partial x_j}\right)^2} - \frac{2}{RePrPl}\overline{P'_r\theta'} \qquad \text{(B.6)}$$

Budgets of equation (B.6) are singularly explained in chapter 4.

The plot of temperature variance radiative budgets for case G10 (see section 4.1.4) calculated using CLAM scheme is shown in figure B.1

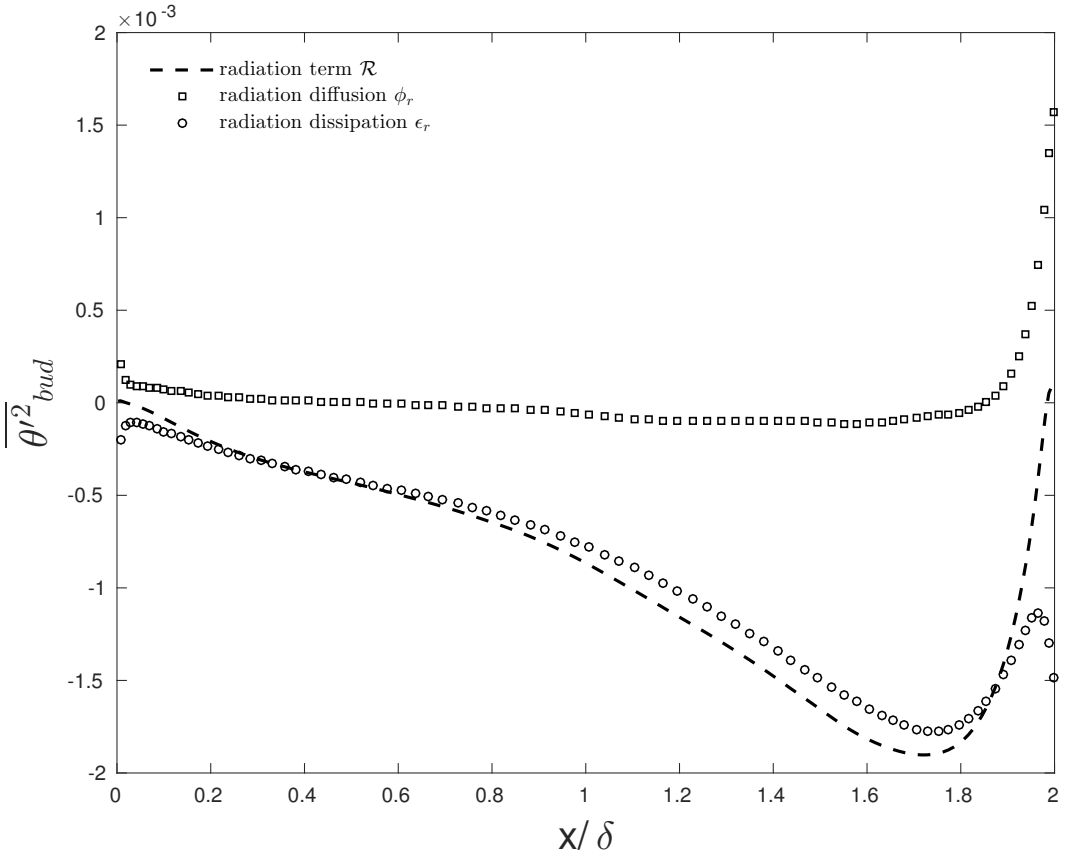

FIGURE B.1: Radiative budgets for temperature variance equation, $\tau = 10$, CLAM scheme

Appendix C

Properties of Fourier transform

Properties of Fourier transform operator will be summariezed below in order to aid the derivation performed in section 2.4.
Definition of Fourier transform of a function $f(x)$ is recalled here:

$$\widehat{f}(w) = \int_{-\infty}^{\infty} f(x) e^{-iwx} dx \tag{C.1}$$

where w is the wavenumber and x the position. Interesting theorems for the derivations performed in the present work are:

- Convolution theorem
- Derivation theorem

Convolution theorem states that:

$$\widehat{f(x)g(x)} = \widehat{f}(w) * \widehat{g}(w) \tag{C.2}$$

Derivation theorem states that:

$$\widehat{\frac{\partial f(x)}{\partial x}} = -iw\widehat{f}(w) \tag{C.3}$$

Bibliography

[1] A. Sakurai, K. Matsubara, K. Takakuwa, and R. Kanbayashi. Radiation effects on mixed turbulent natural and forced convection in a horizontal channel using direct numerical simulation. *Journal of Fluid Mechanics*, 55(1):2539–2548, 2012.

[2] S.P. Burns and M.A. Christon. Spatial Domain based Parallelism in Large-Scale, Participating Media Radiative Transport Applications. *Numerical heat transfer, Part B*, 31(1):401–421, 1997.

[3] Yufang Zhang. *Coupled convective heat transfer and radiative energy transfer in turbulent boundary layers*. PhD thesis, Laboratoire d'Energetique Moleculaire et Macroscopique, Combustion, CNRS et Ecole Central Paris, 2013.

[4] A. Gupta, M.F. Modest, and D.C. Haworth. Large-eddy simulation of turbulence-radiation interactions in a turbulent planar channel flow. *Journal of Heat Transfer*, 131(6), 2009.

[5] Y. Wu, M.F. Modest, and D.C. Haworth. A high-order Monte Carlo method for radiative transfer in direct numerical simulation. *Journal of Computational Physics*, 223(1):898–922, 2007.

[6] K.V. Deshmukh, M.F. Modest, and D.C. Haworth. Direct numerical simulation of turbulence-radiation interaction in a statistically one-dimensional nonpremixed system. *Journal of Quantitative spectroscopy and Radiative transfer*, 109(1):2391–2400, 2008.

[7] L. Tesse, F Dupoirieux, and J. Taine. Monte carlo modeling of radiative transfer in turbulent sooty flame. *Journal of Heat and Mass Transfer*, 47(1):555–572, 2004.

[8] M. Roger, P.J. Coelho, and C.B. da Silva. Relevance of subgrid-scales for large eddy simulations of turbulence-radiation interactions in a turbulent plane jet. *Journal of Quantitative Spectroscopy and Radiative Transfer*, 112(1), 2011.

[9] A. Gupta, M.F. Modest, and D.C. Haworth. Turbulence-radiation interactions in large-eddy simulations of luminous and nonluminous nonpremixed flames. *Proc. Combust. Inst.*, 2012.

[10] D. Schertzer and O. Simonin. A theoretical study of radiative cooling in homogeneous and isotropic turbulence. In L. J. S. Bradbury, F. Durst, B. E. Launder, F. W. Schmidt, and J. H. Whitelaw, editors, *Turbulent Shear Flows 3*, pages 262–274, 1982.

[11] A. Soufiani. Temperature turbulence spectrum for high-temperature radiating gases. *Journal of Thermophysics*, 5(4):489–494, 1991.

[12] M. Coantic and O. Simonin. Radiative effects on turbulent temperature spectra and budgets in the planetary boundary layer. *Journal of Atmospheric Science*, 41 (1):2629–2651, 1984.

[13] R. Viskanta and M.P. Menguc. Radiation heat transfer in combustion systems. *Energy Combustion Scence*, 13(1):97–160, 1987.

[14] K.V. Deshmukh, M.F. Modest, and D.C. Haworth. Higher-order spherical harmonics to model radiation in direct numerical simulation of turbulent reactive flows. *Journal of Computational Thermal Sciences*, 1(1), 2009.

[15] Michael F Modest. *Radiative Heat Transfer*. Academic Press, 2013.

[16] L.L. Briggs, W.F. Miller Jr., and E.E. Lewis. Ray-effect mitigation in discrete ordinate-like angular finite element approximations in neutron transport. *Nuclear Science and Engineering*, 57(1):205–217, 1975.

[17] G.D. Raithby and E.H. Chui. A finite-volume method for predicting a radiant heat transfer enclosures with participating media. *Journal of Computational Physics*, 112(2):415–423, 1990.

[18] A. Sakurai, T. Song, S. Maruyama, and H.K Kim. Comparison of radiation element method and discrete ordinates interpolation method applied to three-dimensional radiative heat transfer. *Numerical Heat Transfer*, 48(2):259–264, 2005.

[19] S. Maruyama, A. Sakurai, and A. Komiya. Discrete ordinates radiation element method for radiative heat transfer in three-dimensional. *Numerical Heat Transfer*, 51(2):121–140, 2007.

[20] A.D. Kim and M. Moscoso. Radiative transfer computations for optical beams. *Journal of Computational Physics*, 185(1):50–60, 2003.

[21] Moser, Kim, and Mansour. DNS of turbulent channel flow up to $Re_\tau = 590$. *Physics of Fluids*, 11:943–945, 2007.

[22] S.B Pope. *Turbulent Flows*. Cambrige University Press.

[23] G.K. Batchelor. Small-scale variation of convected quatities like temperature in turbulent fluid. general discussion and the case of small conductivity. *Journal of Fluid Mechanics*, 5(1):113–133, 1959.

[24] I.A. Bolotnov, R.T. Lahey Jr, D.A. Drew, K.E. Jansen, and A.A. Oberai. Spectral analysis of turbulence based on the dns of a channel flow. *Computers and Fluids*, 39(1):640–655, 2010.

[25] A. Patel, J.W.R Peeters, B.J. Boersma, and R. Pecnik. Semi-local scaling and turbulence modulation in variable property turbulent channel flows. volume 27, page 095101, 2015.

[26] Sandia National Laboratories Combustion Research Facility. International workshop on measurement and computation of turbulent nonpremixed flames. Available at http://www.sandia.gov/TNF/radiation.html.

[27] J. Kim and P. Moin. Transport of Passive Scalars in Turbulent Channel Flow. *NASA Ames Research Center, Presented at the Sixth Symposium on Turbulent Sheet Flows*, 1987.